**Democratic and Popular Republic of Algeria**
**Ministry of High Education and Scientific Research**

**National Polytechnic School**
Department of Mechanical Engineering
Laboratory of Mechanical Engineering
and Development

**Royal Military Academy of Brussels**

## Doctorat thesis
## in Mechanical Engineering

# Effect of geometrical features on the noise of propellers through time-domain and frequency-domain broadband noise predictions

Mrs. HALIMI Akila

Supervised by: Pr. LARBI Salah (ENP) and MCA. MARINUS G. Benoît (RMA)

Thesis defended on March 17, 2020.

**The jury is composed of:**

| | | | |
|---|---|---|---|
| **President :** | SMAILI Arezki | Professor | E.N.P. Algiers |
| **Examiners :** | IMINE Bachir | Professor | U.S.T.Oran |
| | OUALI Hamid | Professor | E.M.P. Algiers |
| | KHELLADI Sofiane | Professor | E.N.S.A.M. Paris |
| | HAMRI Okba | MCA | E.N.P. Algiers |

**ENP 2020**

**Democratic and Popular Republic of Algeria**
**Ministry of High Education and Scientific Research**

**National Polytechnic School**
Department of Mechanical Engineering
Laboratory of Mechanical Engineering
and Development

**Royal Military Academy of Brussels**

## Doctorat thesis
## in Mechanical Engineering

# Effect of geometrical features on the noise of propellers through time-domain and frequency-domain broadband noise predictions

Mrs. HALIMI Akila

Supervised by: Pr. LARBI Salah (ENP) and MCA. MARINUS G. Benoît (RMA)

Thesis defended on March 17, 2020.

**The jury is composed of:**

| | | | |
|---|---|---|---|
| **President :** | SMAILI Arezki | Professor | E.N.P. Algiers |
| **Examiners :** | IMINE Bachir | Professor | U.S.T.Oran |
| | OUALI Hamid | Professor | E.M.P. Algiers |
| | KHELLADI Sofiane | Professor | E.N.S.A.M. Paris |
| | HAMRI Okba | MCA | E.N.P. Algiers |

**ENP 2020**

**ملخص:**

الهدف من هذه الدراسة هو التحقيق في قدرة الحد من صوت النطاق العريض لمروحة، عن طريق وضع مسننات على الحافة الأمامية و الخلفية. يتم تطبيق نماذج تحليلية جديدة للتنبؤ بالصوت الناتج عن مقطع عرضي لجناح ذو حواف مسننة وتطبيقها على المراوح باستخدام تقسيم الشفرة. يتم تقييم هذه النماذج من خلال المقارنة مع الأطياف التي تم الحصول عليها من محاكاة رقمية تستعمل طريقة Lattice Boltzmann.

أظهرت النتائج التي تم الحصول عليها أن النماذج التحليلية قادرة على التنبؤ بالصوت الناتج عن المراوح المستقيمة أو المسننة بدقة جيدة. تم إجراء دراسة حدية للتنبؤ بالصوت المنبعث من المراوح التي تتميز بحافة أمامية أو خلفية مسننة باعدادات مختلفة. تظهر نتائج الحافة الخلفية المسننة أن استخدام التسننات يقلل من الصوت المنبعث من المراوح بترددات منخفضة إلى متوسطة ولكنه يسبب زيادة في الصوت عند الترددات العالية. تم العثور على أن المسننات الحادة تؤدي لتحقيق أفضل أداء من حيث الحد من الصوت بالنسبة إلى الحافة الأمامية المسننة، توضح النتائج أن التسنينات فعالة في تقليل الصوت الصادر عن المراوح عند الترددات العالية. يزداد تقليل الصوت مع زيادة سعة التسنن ، بينما لا يظهر اختلاف طول الموجة المسننة أي تأثير على تقليل الصوت.

**الكلمات المفتاحية:** الصوت الناتج عن ديناميكية الهواء، صوت النطاق العريض، مروحة، تسنين، نموذج التحليلي، طريقة Lattice Boltzmann.

---

**Résumé:**

Cette étude a pour objectif d'examiner la capacité de réduction du bruit large bande émis par une hélice en appliquant des dents de scie sur son bord d'attaque et/ou son bord de fuite. De nouveaux modèles analytiques pour la prédiction du bruit de profils d'aile avec dents sont implémentés et appliqués aux hélices en utilisant la segmentation de la pale. Ces modèles sont validés par comparaison avec les spectres obtenus par des simulations utilisant la méthode de Lattice Boltzmann.

Les résultats obtenus montrent que les modèles analytiques sont capables de prédire le bruit émis par des hélices sans et avec dents avec une bonne précision. Une étude paramétrique a été conduite pour prédire le bruit émis par des hélices ayant des dents de scie au bord d'attaque et au bord de fuite avec différents paramètres. Les résultats montrent que l'utilisation des dents de scie réduit le bruit de bord de fuite à basses fréquences mais induit un accroissement de bruit à hautes fréquences. Les dents pointues assurent la meilleure performance en terme de réduction de bruit. Pour le bord d'attaque, les résultats montrent que les dents sont efficaces à réduire le bruit de bord d'attaque émis par les hélices à hautes fréquences. La réduction de bruit augmente avec l'augmentation de l'amplitude de la dent, tandis que la variation de sa longueur d'onde ne montre aucun effet sur la réduction de bruit.

**Mots clés**: Aéroacoustique, bruit large bande, hélice, dents de scie, modèle analytique, méthode de Lattice Boltzmann.

---

**Abstract:**

This study aims at investigating into the capability of reducing the broadband noise of a propeller, by means of sawtooth trailing edge and leading edge serrations. New analytical models for predicting noise from airfoils with serrated edges are implemented and applied to propellers using a blade strip approach. These models are assessed by comparison with spectra obtained from time-domain Lattice Boltzmann Method simulations.

Obtained results showed that the analytical models are able to predict the noise from either straight or serrated propellers with a good accuracy. A parametric study was conducted to predict the noise emitted by propellers featuring sawtooth trailing edge or leading edge serrations with different parameters. The results of the serrated trailing edge show that the use of serrations reduces the noise emitted by the propellers at low to mid frequencies but induces a noise increase at high frequencies. The sharpest serrations were found to achieve the better performance in terms of reducing noise. For the serrated leading edge, the results show that the serrations are effective in reducing the noise emitted by the propellers at high frequencies. The noise reduction increases with the increased serration amplitude, while the variation of serration wavelength shows no significant effect on the noise reduction.

**Keywords:** Aeroacoustics, Broadband noise, Propeller, Serrations, Analytical model, Lattice Bolzmann method.

# Acknowledgements

I would like to thank my supervisors Pr. Salah LARBI and Dr. Ir Benoit. G MARINUS for their support and for giving me the opportunity to work with them. Benoit, I am very grateful for all the insightful suggestions, discussions, advice, guidance and most of all for your constant availability throughout my PhD. You gave me the taste for learning.

I want to express my deep gratitude to my colleagues at the High School of Aeronautical Techniques/Dar EL Beidha and all my friends, who supported me and gave me positive energy to carry on this work.

I would like to thank all the staff of the department of mechanical engineering of the National Polytechnic School for making me feel as I was one of them.

I spent six nice months in the department of mechanics of the Royal Military Academy of Brussels, and met many people who were so kind to me. I warmly thank all of them.

I would like to thank my family and especially my parents who carved deeply into my soul the living truth that dialogue is paramount; whether it is about the practical things of life or over the fundamental differences that strengthen us.

# Contents

# List of Tables

# List of Figures

# Nomenclature

| | | |
|---|---|---|
| $B$ | Blade count | |
| $c$ | Blade/Airfoil chord | $[m]$ |
| $c_0$ | Speed of sound | $[m.s^{-1}]$ |
| $C_f$ | Skin friction coefficient | |
| $C_p$ | Pressure coefficient | |
| $D$ | Blade diameter | $[m]$ |
| $f$ | Frequency | $[Hz]$ |
| $h$ | Half root-to-tip length of the serration | $[m]$ |
| $J$ | Advance ratio | |
| $K_1, K_2$ | Streamwise and spanwise aerodynamic wavenumbers | $[m^{-1}]$ |
| $k$ | Acoustic wavenumber | $[m^{-1}]$ |
| $L$ | Airfoil span | $[m]$ |
| $L_t$ | Turbulence length scale | $[m]$ |
| $l_y$ | Spanwise correlation length | $[m]$ |
| $M$ | Mach number of uniform flow | |
| $M_t$ | Mach number of the source relative to the observer | |
| $M_z$ | Axial Mach number | |
| $N$ | Rotational velocity | $[rpm]$ |
| $p_f$ | Far field sound pressure | $[Pa]$ |
| $P_{ia}$ | Magnitude of incident wall pressure gust | $[Pa]$ |
| $R$ | Blade radius position | $[m]$ |
| $R_T$ | Ratio of the outer to inner boundary layer time scale | |
| $S_0$ | Correction distance for convection effects | |
| $S_{pp}$ | Far field pressure PSD | $[dB.Hz^{-1}]$ |
| $t$ | Blade/Airfoil thickness | $[m]$ |
| $T_u$ | Turbulence intensity | $[\%]$ |
| $U$ | Flow velocity | $[m.s^{-1}]$ |
| $U_c$ | Convection velocity | $[m.s^{-1}]$ |
| $U_e$ | External velocity | $[m.s^{-1}]$ |
| $\vec{x} = (x_1, x_2, x_3)$ | Airfoil model frame of reference | |
| $\vec{X} = (x_1, x_2, x_3)$ | Observer position in the fixed reference frame | |
| $(R_0, \Theta, \Psi)$ | Observer position in the fixed reference frame | |
| $\vec{y} = (y_1, y_2, y_3)$ | Observer position in the blade reference frame | |

# Greek letters

| | | |
|---|---|---|
| $\alpha$ | Free stream to convection speed ratio | |
| $\beta$ | Compressibility parameter | |
| $\beta_c$ | Clauser's parameter | |
| $\delta$ | Boundary layer thickness | $[m]$ |
| $\delta^*$ | Boundary layer displacement thickness | $[m]$ |
| $\theta$ | Boundary layer momentum thickness | $[m]$ |
| $\Theta$ | Angle of observer from upstream rotor axis | $[^o]$ |
| $\lambda$ | Wavelength of the serration | $[m]$ |
| $\Pi$ | Parameter of the wake's law | |
| $\rho_0$ | Air specific mass | $[kg.m^{-3}]$ |
| $\tau$ | Wall shear stress | $[Pa]$ |
| $\Psi$ | Angle of flow in rotor plane | $[^o]$ |
| $\Phi_{pp}$ | Wall pressure PSD | $[dB.Hz^{-1}]$ |
| $\Phi_{ww}$ | Impinging upward velocity | $[dB.Hz^{-1}]$ |
| $\phi_{ww}$ | Velocity PSD | |
| $\omega$ | Angular frequency | $[s^{-1}]$ |
| $\omega_e$ | Emitted angular frequency | $[s^{-1}]$ |
| $\Omega$ | Rotational velocity | $[rad.s^{-1}]$ |

# Abreviations

| | | |
|---|---|---|
| $BPF$ | Blade Passage Frequency | |
| $CFD$ | Computational Fluid Dybamics | |
| $DNS$ | Direct Numerical Simulation | |
| $LBM$ | Lattice-Boltzmann Method | |
| $PSD$ | Power Spectral Density | $[dB.Hz^{-1}]$ |
| $RANS$ | Reynolds Averaged Navier-Stokes | |
| $SPL$ | Sound Pressure Level, $p_{ref} = 2.10^{-5}$Pa | $[Hz]$ |
| $SLE$ | Serrated Leading Edge | |
| $STE$ | Serrated Trailing Edge | |
| $UDF$ | User Defined Function | |

# *Chapter I*
# *Introduction*

# Chapter 1
# Introduction

## 1.1 Aim and context

Since the first flight of the Wright brothers on December the $17^{th}1903$, propellers were the only propulsion system for aircraft but became merely an alternative when the turbojet and later the turbofan appeared. It is only in the late $1970s$, under the pressure of high fuel prices, that new concepts such as the single- or counter-rotation propfan were developed. These concepts promised interesting efficiencies though they required additional development to keep vibration and noise levels within reasonable limits [1].

The use of advanced propellers is quite frequent these days, especially to propel Unmanned Aerial Vehicles (UAVs). Due to their unique properties, UAVs are used in tactical surveillance missions or for reconnaissance purposes. In order to gain information about the scouting area without being easily identified, achieving an acoustically stealth-mode is an essential feature of mission success. Despite the different aims, the noise footprint of these vehicles is extremely important even when employed in civilian roles, due to their flight proximity to populated urban areas. This fact makes drone noise a challenging issue for scientific community at both industrial and academic level. In a recent document [2], the European Aviation Safety Agency (EASA) specified the noise level requirement for drones at a fixed value of $60dB(A)$, measured at a distance of $3m$ from the source. Generally, the strategic objectives for drone market growth are greater endurance and acoustic impact reduction. These two aspects are also key issues to improve the safety of this technology in the future. Drone noise pollution is also a problem from the point of view of public acceptance of the widespread deployment of flying drones in urban areas.

For propeller-driven aircraft, the main noise sources are the engine and the propeller itself. Therefore, to reduce drone noise signature, the only way to proceed is to optimize both components at the same time. For this reason, in recent years, there has been renewed interest in the propellers. Rotor noise is becoming a very central issue because

of the several fields of drones applications. The aerodynamic noise of conventional propellers can be split into two main components in the Fourier domain: tonal and broadband contributions [1, 3]. Tonal components are directly related to the periodic motion of the blade in the surrounding fluid. Therefore, the frequency and magnitude of the radiated noise is related to rotational velocity. The physical mechanism associated with the production of the tonal contributions is related to blade thickness and to aerodynamic loading. On the other hand, broadband noise is radiated by the interaction of turbulent flow structures with the blade edges. Therefore, it is either generated at the blade leading/trailing edge or at the blade tip.

Propeller noise is a central and complicated issue that has to be taken into account in system design. There are two basic strategies to control the noise generated: active and passive [4]. Active flow control methods include active modifications of airfoil geometry or flow conditions, which is achieved by either modifying airfoil geometry and surface through actuators, or by acting on the local boundary layer through blowing and suction jets. On the other hand, passive flow control techniques enable the boundary layer to be manipulated without further consumption of additional energy, and it can be employed to reduce noise generation. The first strategy is to employ an optimized geometry by taking into account acoustic constraints in the multi-disciplinary optimization process [5]. This solution ensures that aerodynamic, structural and acoustic problems are addressed simultaneously but leads to blade geometry that reduces noise for a specific operating configuration, so it is not sure that in other configurations the behaviour would be exactly the same, both in terms of thrust and noise generation. The boundary layer tripping is also used by adding a strip of an adhesive tape near the leading edge on the suction surface of a propeller blade [6]. Another strategy to reduce noise is the use of porous materials [7]. The effect of porosity on rotor noise has been studied principally for wind turbines but it seems very interesting also for UAV rotors. Recent observations and studies on owls [8] found that they can fly quietly close to their prey, and have the well-known ability of silent flight, which may be an excellent biological clue for finding solutions for quieter aircraft and other aerodynamic structures. This led to innovative aerodynamic geometries, the most effective being the

application of serrations.

In this study the focus is on this control method. The use of serrations is of particular interest in this work due to its potential noise reduction efficiency.

## 1.2 Thesis objective

Serrations have been extensively studied and proved their effectiveness in reducing self noise and turbulence interaction noise of airfoils, wind turbines and axial fans, however studies on their use for propellers are scarce. Furthermore, no comprehensive study was conducted to model analytically propeller blades with serrated edges and there are even less validation cases where analytical results are compared to experimental or numerical ones. Such analytical models are particularly useful in the design stages of propellers or complete aircraft because they are relatively computationally cheap. Consequently, this study presents an investigation into the capability of reducing broadband noise of an innovative propeller geometry operating at Mach 0.2, by means of sawtooth serrations. The serrations are not inserted onto a classical rounded edge but are obtained by variation of the spanwise distribution of chord and thickness which results in the existence of streamwise streaks into both sides of the blade. The noise spectrum is predicted using a new analytical model for predicting noise from serrated airfoils extended to rotating blades by the use of the strip approach. The analytical results are compared with time-domain LBM simulations performed for the same geometries. The sensitivity of noise reduction to the geometry is calculated through variations in amplitude $2h$ and wavelength $\lambda$ reported to the boundary layer thickness $\delta$ for the serrated trailing edge and to the turbulence length scale $L_t$ for the serrated leading edge. The objective is to assess:

– The serrations parameters that yield maximum noise reduction;
– The effect of flow conditions on the noise reduction;
– The effect of serrations on the local flow features around the blades.

The main original contributions of this study are:

– Complete calculation of the broadband noise spectrum for a low speed propeller blade ($M = 0.2$) with straight or serrated trailing edge/leading edge;

– Implementation of a recent analytical formulation for predicting trailing edge/leading edge noise from airfoils which has been extended to rotating blades to assess the potential of noise reduction when applying sawtooth serrations on the trailing edge/leading edge of a propeller blade;
– A parametric study of the effect of the main geometric parameters onto the reduction up to high frequencies ($11kHz$);
– High-fidelity modelling of the noise radiated by either the baseline and the serrated blades using a time-domain Lattice-Boltzmann method software.

## 1.3 Thesis structure

This thesis describes the results of analytical and numerical study aimed at investigating the potential of self noise and turbulence interaction noise reduction of a propeller blade using sawtooth serrations.
Chapter 2 gives an overview of the broadband noise reduction using serrations either for airfoils and rotating blades. Chapter 3 related to the analytical prediction of broadband noise, presents an outline about the noise footprint signature of airfoils and propellers and the analytical approaches used to predict the broadband noise. The derivation of Amiet's model for predicting trailing edge noise from airfoils is detailed along with the formulae derived by Roger and Moreau for trailing edge and leading edge noise. The models implemented for airfoils are then extended to rotating blades by the use of the strip approach and by taking into account the Doppler effect. The models are validated by comparison to experimental data available in the literature. Chapter 4 details the theory behind the Lattice-Boltzmann time-domain high-fidelity method used to model the noise emitted by the blades. The geometries of the baseline and the serrated blades are then described in addition to the operating conditions. The numerical set up and the influence of the numerical parameters on the noise prediction performance are also discussed. Chapters 5 and 6 present the serrated propellers broadband noise predictions using the analytical and the numerical models described in the two previous chapters. First, the analytical models are assessed by comparison to the LBM results. The influence of the serration parameters on the noise reduction is studied along with

the influence of the operating conditions. The directivity patterns are also drawn in order to depict the response of the serrated blades over different observer positions. The effect of the introduction of serration on the aerodynamic flow field around the blades is also studied. Finally, general conclusions are drawn together with possible points for improvement.

# *Chapter 2*
# *State of the art*

# Chapter 2
# State of the art

This chapter contains a review of the broadband noise reduction using serrations either for airfoils and rotating blades. First, a brief history of the research conducted on airfoil broadband noise reduction by the use of serrations is presented. Then, a survey of the use of serrations on the trailing edge/leading edge of airfoils and rotating blades is detailed.

## 2.1 Airfoil broadbnd noise reduction using serrations

The silent flight of the owl was investigated in the early 1970$s$ as part of a program researching novel designs for quieter aircraft. Recently, an in-depth study of the structure of the wing conducted by Bachmann et al. [8] showed that, through millions of years of evolution, the owl has developed wavy comb-type leading edges (or serrations) and fringe type trailing edges that generate noise under $2kHz$, while their preys acute hearing system is typically within the range $2 - 20kHz$. The study provided detailed pictures of the wing structure shown in figure 2.1 where the leading edge and trailing edge features are highlighted.

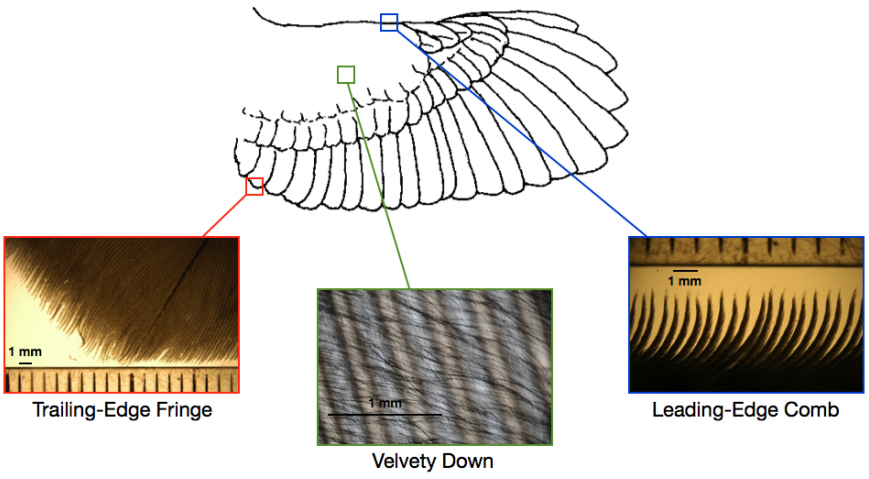


Figure 2.1: Structure of the Owl's wing [8].

Kroeger et al. [9] and Lilley et al. [10] showed that the leading edge serrations on the owl wing completely suppressed the separation of the flow that would normally occur along a steep downwards flight path of $24^o$ at the low Reynolds number of about $1.5e5$. Instead, vortices are shed from each serration and the boundary layer remains attached, even when the wing dynamics approach stall, therefore providing noise reductions of up to about $20dB$. When the leading edge comb structure was removed, the flight of the owl became unstable and as noisy as any other bird. In addition, the fringes at the wing trailing edge provide a smooth mixing of the upper and lower boundary layer and reduce the scattering by the edge discontinuity. Lilley associated a reduction of about $6-7dB$ due to the trailing edge fringes only, by comparison with noise measurements performed on a bird of similar size and mass. Lilley also attributed the very low noise emission at frequencies above $2kHz$ to an absorption of the boundary layer energy by the compliant surface covering the upper wing and the paws of the owl, due to a fluffy fibrous material whose fibres are only slightly larger than the Kolmogorov length scales.

Recently, Johari et al. [11] studied the effect of leading edge protuberances inspired from humpback whales flippers (figure 2.2) on the performance of an airfoil. The outcomes revealed that the protuberance amplitude had a distinct effect on the performance of the airfoil, whereas the wavelength had little.

## 2.2 Trailing edge noise

The theoretical problem of the acoustic scattering of the boundary layer vortices past a trailing edge has received much attention starting from the $1970s$. Different approaches, reviewed by Howe [12], were considered, depending on the way the noise generation and propagation are handled. Amiet [13] and Howe [14,15] proposed an analytical radiation model for the interaction of a turbulent boundary layer convected past a semi-infinite rigid flat plate at $0^o$ incidence in a subsonic flow. These two models mainly differ in the way the aerodynamic near field is related to the acoustic radiation. Both lead to the conclusion that the sound radiated in the far field follows a velocity power law of $U^5$ for the pressure density spectrum. Both models are valid for acoustic wavelength

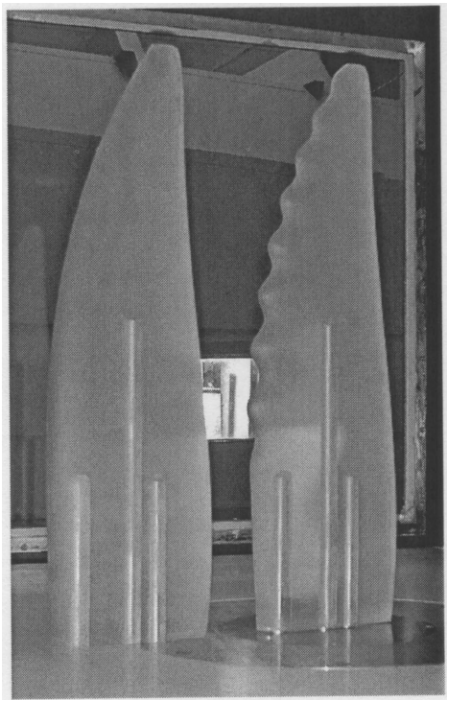

Figure 2.2: $3D$ scale model of a humpback whale flipper with and without sinusoidal leading edges [11].

smaller than the airfoil chord (due to the semi-infinite flat plate assumption). Amiet's model is valid for all subsonic flows while Howe's model is valid for very low Mach numbers only.

To take into account the effect of rotation on trailing edge noise modelling, Amiet [16] proposed a simplified alternative approach, which has been widely used since. This approach consists of approximating the noise from an airfoil in rotating motion by the average over the angular position of the noise from a translating airfoil. In other words, the circular motion is approximated by a series of translations over an infinitesimal distance. Amiet stated that this approach is valid at high frequencies and low rotor speed, where the effects of rotation on the noise are weak. This method has been first applied to the leading edge rotor noise by Paterson and Amiet [17] and to trailing edge rotor noise by Schlinker and Amiet [18]. This formulation has been used extensively in many applications: helicopter rotors [16], wind turbines [19] and propellers [20, 21]. Later, Amiet's analytical model has been extended by Roger and Moreau [22, 23] to include a leading edge back-scattering correction, which takes into account the effect

of the finite chord. When the turbulent structures are scattered at the trailing edge, acoustic waves propagate upstream of the flow. Back-scattered waves from the trailing edge are then scattered again at the leading edge of the airfoil. The extended model have been validated by Rozenberg et al. [24, 25] for a low speed axial fan and Pagano et al. [26] for a propeller blade in a pusher configuration.

The main input data for the trailing edge noise models are the wall pressure statistics near the trailing edge. They can be obtained by experiments [27] or deduced from detailed numerical simulations [28]. However, these latter are still too computationally expensive to model the acoustic sources accurately. Consequently, different empirical spectral models have been proposed to evaluate the wall pressure spectrum, providing the inner or outer variables of the turbulent boundary layer [18, 29, 30].

## 2.3 Trailing edge serrations

Inspired from the owl feathers, serrations were applied to airfoils in order to investigate their efficiency in reducing trailing edge noise. Howe [31] developed an analytical model to investigate the noise produced by low Mach number turbulent flow over a flat plate with a serrated trailing edge of sinusoidal [32] and sawtooth [31] profiles (figure 2.3) at zero angle of attack.

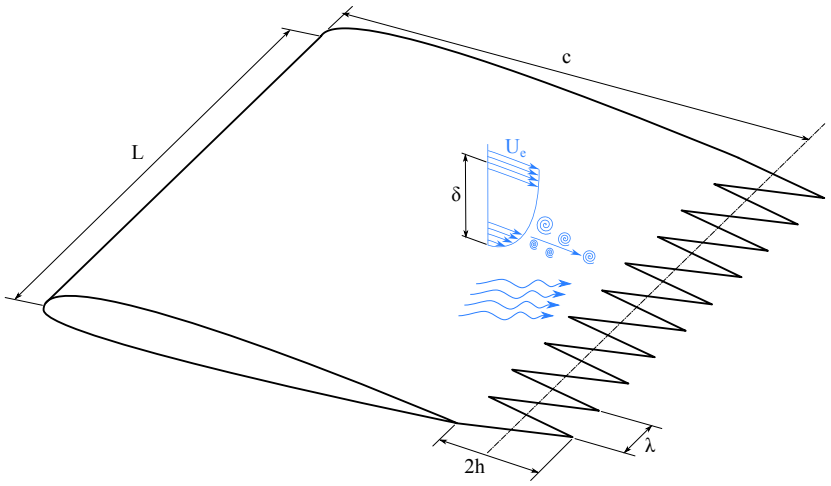


Figure 2.3: Airfoil with trailing edge serrations.

The results indicated that sawtooth serrations achieved better noise reduction over

sinusoidal ones. Moreover, the use of sharp sawtooth with $h/\lambda > 4$, where $h$ and $\lambda$ are the half root-to-tip length and the wavelength of the serration respectively, can lead to substantial reductions in radiated trailing edge sound levels. Howe's model overestimates the noise reduction compared to experimental data, but it provides useful insight into the mechanisms of noise reduction obtained when using trailing edge serrations. Later, Azarpeyvand et al. [33] extended Howe's mathematical model to study novel trailing edge serrations profiles. The results showed that the noise reduction is dependant of the serration geometry and that the noise efficiency can be significantly reduced by applying complex periodic serrations to the trailing edge. Meanwhile, Jones et al. [34] performed Direct Numerical Simulations of the flow around a NACA0012 airfoil fitted in turn with a straight edge, a short serration of amplitude similar to the boundary layer thickness $\delta$, and a long serration of amplitude about $2\delta$, at Reynolds number $Re_c = 50000$ and $M = 0.4$. Broadband noise reductions of between $6 - 10dB$ were obtained, and it was found that the noise reduction was greater for the long serrations and spread over a larger frequency bandwidth. For the shorter serration only, an increase of the noise was observed at high frequencies. The trailing edge noise directivity was not affected by the presence of the serrated trailing edge. The boundary layer properties were found to be little affected by the presence of the serrations and the formation of horse-shoe vortices was reported to occur behind the serrations, promoting a faster mixing of the turbulence in the airfoil wake. An experimental investigation on the acoustic performance of a serrated trailing edge airfoil with different sawtooth geometries was then conducted by Gruber [35]. It was reported that a noise reduction of $7dB$ over a wide frequency range was achieved while a noise increase of about $3dB$ is measured at higher frequencies. The main results showed that the frequency at which noise is increased is $f\delta/U \approx 1$, where $\delta$ is the boundary layer thickness and $U$ is the flow velocity. The following conditions need to be fulfilled to reduce the noise: $h/\delta > 0.5$ and $\lambda$ to be small. Moreau et al. [36] investigated the sawtooth trailing edge noise of a flat plate at low-to-moderate Reynolds numbers. Serrations were found to achieve noise attenuation over a wide range of frequencies, depending on Strouhal number and serration wavelength, without modifying the directivity of the radiated noise. Recently,

Lyu et al. [37] developed a new mathematical model to predict the sound radiated from an airfoil with serrated trailing edge. According to this model, the sound reduction achieved by a trailing edge with a sharp sawtooth serration is around $5 - 10dB$ for a wide bandwidth. Fisher at al. [38] combined the model of Lyu with CFD-RANS results to predict the far field sound pressure emitted from an airfoil with a sawtooth serrated trailing edge. It was found that the first order solution underestimates the measured sound spectrum by about $3dB$ but the tendency between the serration geometries is predicted correctly, which lead to the fact that this model can be used to optimise serrated geometries.

The noise reduction potential of rotating blades with serrated trailing edge is experimentally well documented. The work of Dassen et al. [39] and Oerlemans et al. [40] demonstrated that serrations reduce the trailing edge noise for wind turbines despite a noise increase at high frequencies. In [39] serrations were applied to the wind turbine blade trailing edge in order to determine the effect of length, position and orientation of the teeth on the noise reductions. This study included small scale experiments in which it was found that serrations gave an overall reduction of $2dB$ at low frequencies while increasing the noise at high frequencies and at high incidence angles of attack. Oerlemans [40] investigated the use of serrations and airfoil shape optimization to reduce trailing edge noise. Experiments were conducted on a $94m$ diameter, three bladed wind turbine in an open-jet wind tunnel. A NACA64418 airfoil model was selected as the reference blade because of its common use in modern wind turbines. One blade was optimized for aerodynamics, one blade for trailing edge noise reduction with serrations along the span, and one blade remained untreated and was used as the reference blade. Serrations showed reductions of about $2 - 3dB$, however a significant noise increase was reported at high frequency attributed to a misalignment of the serrations with the flow.

Although the use of serrations on rotating blades has proved its efficiency to reduce the trailing edge noise experimentally, there have been few attempts at modelling serrated rotating blades analytically. Sinayoko et al. [41] tackled the effect of rotation on the efficiency of serrations, for a wind turbine blade element. Their model combined Howe's

low Mach number isolated airfoil theory with Amiet's [16] rotating airfoil technique. They reported that obtained results for stationary blades can be applied to a rotating blade and that rotation has little impact on the noise reduction produced by the serrations. The results, obtained with the zero-order approximation of the analytical model, showed that the most effective serrations are deep and narrow relative to the boundary layer thickness satisfying the conditions: $\lambda \leq \delta$ and $h \geq \lambda$, and reduce noise at high enough frequencies.

Trailing edge serrations have proven to be valid solutions of trailing edge noise reduction, however its underlying noise reduction mechanism is still not fully understood. Several aerodynamic mechanisms are candidates to explain the noise reduction in the low to mid frequency range and the noise increase at higher frequencies:

– The mean pressure difference between the suction and pressure sides at the trailing edge drives the wake to start mixing together at the roots of the serrations and finally creates cross flow [42]. The cross-flow increases the distance between the model surface and the suction side boundary layer [43], and thus leads to a less efficient scattering source;
– Flow visualization showed that stronger turbulence exists on the predominantly sawtooth's oblique side edges and peaks. Vathylakis and Chong [44,45] conjectured that there were convective pressure-driven spanwise vortical structures near the sawtooth side edges and amalgamation of the vortical structures on both sides near the sawtooth peaks. The interaction between these vortical structures and the local turbulent boundary layer could be an effective mechanism to redistribute the momentum transfer, turbulent shear stress, and energy spectrum, resulting in reduced convection velocity of the turbulent eddies and weakened scattering of the turbulence interaction noise;
– The particular sawtooth geometry reduces the spanwise coherence (related to the spanwise correlation length), which further reduces the noise generation efficiency. In the streamwise direction, the turbulent eddies propagates at a similar speed for both the baseline and serrated trailing edges. In the spanwise direction, on the other hand, no convection velocity or any discernible difference in phase spectra exists

for the baseline trailing edge, but noticeably different spanwise coherence and phase spectra functions are present for the serrated trailing edges [44–46];

– The cross flow through the roots between adjacent teeth increases turbulence activity and produces small jets, which are believed to be the reason for high-frequency noise increase [42].

## 2.4 Turbulence interaction noise

First studies on the turbulence interaction noise of airfoils were initiated by Sears [47], Graham [48] and Amiet [49]. Sears originally considered the interaction of an unsteady sinusoidal gust with a flat plate and developed a model for the prediction of the plate aerodynamic response under such unsteady loading. Sears' model was later developed and extended to compressible flows by Graham [48] and Amiet [49]. In Amiet's model, the blade response function to an incoming gust is first obtained using the Schwarzschild technique and the far field sound is then formulated based on the theories of Kirchoff and Curle using the radiation integral. Amiet's model relates the far-field sound power spectral density (PSD) to the energy spectrum of the velocity fluctuations of the incoming gust. It has been widely shown that Amiet's model can provide fairly good comparisons with experimental observations when the turbulence statistical quantities are known. Later, the theoretical power spectral density presented in the midspan plane by Amiet [49] has been extended by Roger and Moreau [22, 23] to three-dimensional gusts for application to arbitrary observer location and semi-empirical corrections have been proposed by Moreau et al. [50] to account for the effect of camber and thickness of a slightly cambered thick airfoil.

## 2.5 Leading edge serrations

The geometrical modification of the airfoil leading edge to reduce the turbulence interaction noise has been the subject of several studies [51–53] performed in the 70s. These latter showed that the leading edge serrations were effective in reducing turbulence interaction noise for airfoils and rotating blades with specific configurations and operating conditions. Since then, various investigations were performed to tackle

the effect of leading edge serrations on reducing noise and the mechanisms behind this reduction. Roger et al. [7] conducted a series of experiments on a NACA0012 airfoil to assess possible means to reduce its emission of turbulence interaction noise. Two techniques were investigated: the design of leading edge serrations (figure 2.4) and the use of porous materials. Both methods were found to reduce noise.

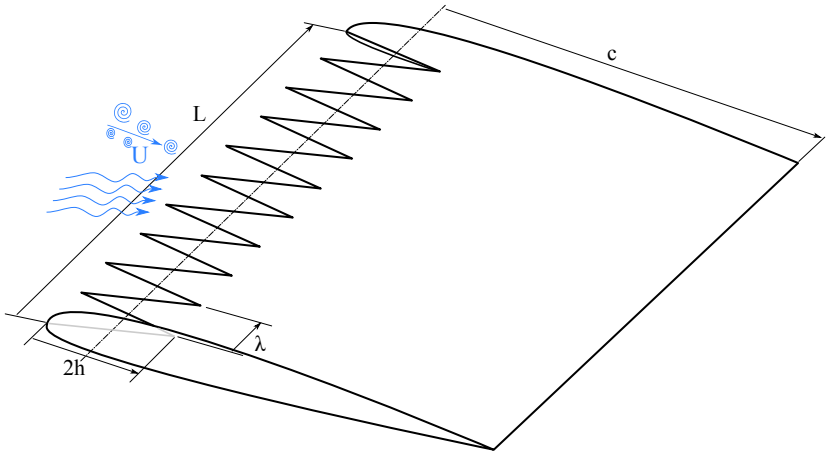


Figure 2.4: Airfoil with leading edge serrations.

Moreover, the airfoil with leading edge serrations accomplished a reduction of $10dB$. Later, Narayanan et al. [54] studied in detail the influence of the wavelength $\lambda$ and the amplitude $2h$ characteristics of sinusoidal serrations applied on a flat plate. It was found that a significant noise reduction was achieved in the mid frequency range. The flat plate results were compared to the performance of a NACA65 airfoil with the same serrations profile. The obtained results depicted a better noise reduction attained by the flat plate compared to the airfoil. The results of the parametric study showed that the serration amplitude is the factor determining noise control performance, overall noise reduction level was found to vary logarithmically with the serration amplitude but was weakly dependant on the serration wavelength. Chaitania et al. [55] carried out this study by using complex serrations geometries formed by a superposition of two serration profiles of different frequency, amplitude and phase. These serrations were found to provide greater noise reduction than single wavelength serrations.

In parallel, many numerical and analytical studies were conducted to evaluate the noise reduction capability of using leading edge serrations on airfoils. The computational re-

sults of Lau et al. [56] revealed that the hydrodynamic quantity $k_1 h$ is a key factor in determining the serration effectiveness, where $k_1$ is the hydrodynamic wavenumber of the disturbance in the streamwise direction. The serration wavelength $\lambda$ was found to be less important. It was observed that the ratio $2h/\lambda_g$ is an important factor that characterises the acoustic performance of wavy leading edge, where $\lambda_g$ is the wavelength of the incident gust. The reduction of noise was found to increase with $2h/\lambda_g$ and is significant for $2h/\lambda_g \geq 0.3$. Later, Turner et al. [57] used a dual-frequency wavy serration profile and found that the noise reduction increases with more complex serration geometries. In more recent work, Lyu et al. [58, 59] derived a generalised Amiet model to predict the turbulence interaction noise from a flat plate with sawtooth leading edge serrations. The noise spectra predicted by this model were in good agreement with experimental data which suggested that the model can capture the essential physics of the noise generation and reduction mechanisms and can provide an accurate prediction of the noise from serrated leading edges. A parametric study was conducted to assess the effect of serration geometry on the emitted noise. It was found that in order to reduce turbulence interaction noise the serration wavelength has to be sufficiently small and the amplitude has to be large. Moreover, the effect of flow convective effects was studied. The outcomes revealed that serrations geometry does not affect the trends of the predicted spectra when increasing the mean flow velocity. Shallow serrations (large $\lambda$ and small $h$) increase significantly noise with Mach number.

Currently, the focus is on understanding mechanisms by which leading edge serrations are able to reduce the noise produced through the interaction with turbulent flow. Most of the studies are numerical or analytical due to the fact that obtaining near field quantities near the leading edge is hard experimentally. In this context, Kim et al. [60] performed numerical simulations on a flat-plate airfoil with straight and wavy leading edges. The results show that two main mechanisms are responsible for the noise reduction: a source cut-off and a phase interference effects existing in the surface pressure fluctuations along the leading edge. The analytical results of Lyu et al. [58] suggested that the destructive interference of the scattered pressure induced by the leading edge serrations is responsible for the noise reduction, especially in the

mid to high frequency regime where the leading edge noise is most effectively reduced using serrations. Later, Ayton et al. [61] presented an analytical solution for the sound generated by an unsteady gust interacting with a semi-infinite flat plate with a serrated leading edge. The solution predicted a logarithmic dependence between the serration amplitude and the decrease of far field noise. The mechanisms behind the noise reduction were proposed to be an increased destructive interference in the far field, and a redistribution of acoustic energy from low cut-on modes to higher cut-off modes as the serration amplitude is increased. Recently, Wang et al. [62] carried out a numerical investigation of an airfoil inspired by the owl wing and another one with a wavy leading edge and a serrated trailing edge. The results of the flow field around the airfoil with serrations indicated that the range and size of separation vortices were reduced compared to the straight edge airfoil and that the tube shaped vortices in the wake were restrained and split into small scale vortices which cause less aerodynamic noise.

In summary, the use of serrations on airfoils, wind turbines and axial fans has interested many researchers whose studies proved that this passive control strategy is effective in reducing either trailing edge or leading edge noise. However, studies on the use of serrations for propellers are scarce. Furthermore, there are few attempts to model analytically propellers blades with serrated edges. The objective of this study fits into this context, aiming at modelling the broadband noise spectrum of serrated propeller blades using a frequency-domain analytical formulation developed for airfoils with serrated edges [37, 58]. Alternatively, a numerical approach using the time-domain LBM method is set up to predict numerically the spectra emitted by the serrated blades and inspect the flow field around the blades.

# *Chapter 3*
# *Analytical prediction of broadband noise*

# Chapter 3
# Analytical prediction of broadband noise

Aeroacoustics is concerned with sound generated by aerodynamic forces or motions originating in a flow rather than by the externally applied forces or motions of classical acoustics. Thus, the sounds generated by vibrating violin strings and loudspeakers fall into the category of classical acoustics, whereas sounds generated by the unsteady aerodynamic forces on propellers or by turbulent flows fall into the domain of aeroacoustics [63].

Aerodynamic noise radiation from an unsteady flow is a dissipation mechanism by which a tiny part of the mechanical energy of the flow is converted into sound [64]. The particularity of this acoustic dissipation is that it propagates at large distances and contaminates the environment. The acoustic dissipation of aerodynamic noise is an increasing function of the flow speed. Yet it is a much lower order of magnitude than other forms of dissipation such as viscous losses. The description of the acoustic field requires a higher level of accuracy such as in unsteady flows encountered in aeronautics. Unsteady flows, both periodic and turbulent, will appear as the source of what is called the aerodynamically generated noise. The theory of sound generated aerodynamically, as a branch of acoustics, is new since it was established in the sixties in connection with the noise from aircraft.

This chapter will give an overview of the mechanisms by which aerodynamic noise is generated around airfoils and propellers blades. The prediction methods for propeller broadband noise are described and the detailed development of Amiet's formulation is given along with the trailing edge noise and the turbulence interaction noise models expressions. The models implementation is validated against available airfoils data found in the literature. Finally, the strip approach used to extend Amiet's model for airfoils to rotating blades is explained with its validation with a fan test case.

## 3.1 Airfoil broadband noise mechanisms

The first fundamental principle to be retained from everyday life experience is that vortex dynamics makes sound. This implies two major mechanisms. First, sound is generated as free vortices interact mutually; this occurs in any turbulent mixing region such as free jet or a turbulent boundary layer over a smooth boundary. Secondly, sound is generated as vortices interact directly with a geometrical singularity of a solid surface such as a sharp edge, a corner, an excrescence or any accident. The second mechanism is much more efficient [63]. Moreover, the faster the inertia variation in a vortical flow is, the more efficient is the acoustic dissipation. This makes sound production much stronger in the vicinity of singular points on a solid surface, such as leading or trailing edges of airfoils, blades,...

As mentioned by Brooks et al. [65] the noise radiated by an airfoil can be tonal due to instabilities developing in a laminar boundary layer and to vortex shedding, or broadband. The broadband noise is mainly due to two mechanisms, namely interaction with the upstream turbulence and boundary layer turbulence scattering at the trailing edge (figure 3.1). Both of them involve the same basic process: sound is generated as the inertia of vortical flow is modified by its interaction with a singularity on a solid surface.

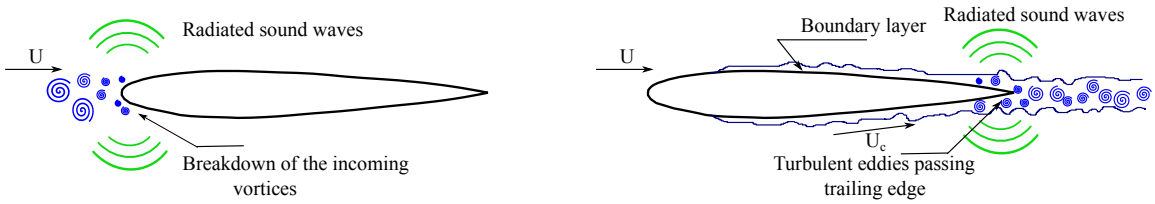


(a) Turbulence interaction noise. (b) Trailing edge noise.

Figure 3.1: Broadband noise mechanisms for airfoils.

The first mechanism, referred to as turbulence interaction noise, involves the breakdown of oncoming vortices on the airfoil and corresponds to equivalent acoustic sources centred at the leading edge. The second mechanism, referred to as trailing edge noise or self noise, is due to the scattering of the airfoil boundary layer vortical structures into acoustic waves at the trailing edge.

Brooks classified self noise mechanisms into five categories:

– Turbulent boundary layer- trailing edge noise;

– Separation stall noise;

– Laminar boundary layer- vortex shedding noise;

– Tip vortex noise;

– Trailing edge bluntness- vortex shedding noise.

## 3.2 Propeller's noise signature

Rotating blades emit two distinctly different types of acoustic signature. The first is referred to as tonal or harmonic noise, and is caused by sources that repeat themselves exactly during each rotation of the propeller. The second is broadband noise which is a random, non-periodic, signal caused by turbulent flow over the blades [1].

Tonal noise is the periodic component, that is, its time signature can be represented by a pulse which repeats at a constant rate. If an ideal propeller with B blades is operating at constant rotational speed N, then the resulting noise appears as a signal with fundamental frequency BN. The blade-passage period is $1/BN$. Typically the generated pulse is not a pure sinusoid, so that many harmonics exist. These occur at integer multiples of the fundamental frequency. The first harmonic is the fundamental, the second harmonic occurs at twice the fundamental frequency, and so on. Broadband noise is random in nature and contains components at all frequencies. The frequency spectrum is continuous, although there may be a shape to it because not all frequencies have the same amplitude. Noise spectrum for propellers is typically represented graphically in the frequency domain for a given microphone or pressure transducer, as shown in figure 3.2.

### 3.2.1 Tonal noise

Periodic noise is generated by steady sources which are those which would appear constant in time to an observer on the propeller moving with it. These latter produce periodic noise because of their rotation. Noise sources are divided into three categories: thickness, loading and quadrupole [1].

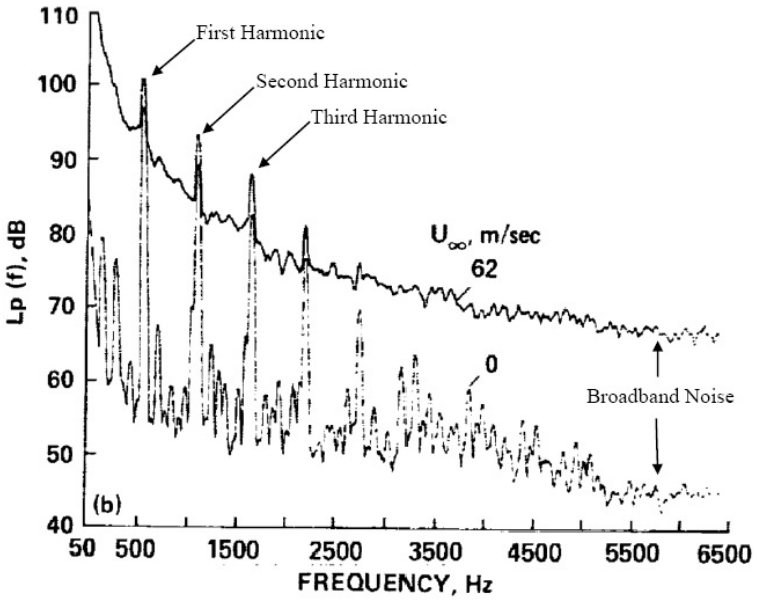


Figure 3.2: Propeller's noise spectrum captured at a pressure transducer for two different free stream velocities [66].

- Thickness noise is generated by the transverse periodic displacement of the air by the volume of a passing blade element. The amplitude of this noise component is proportional to the blade volume, with frequency characteristics dependent on the shape of the blade cross section (airfoil shape) and rotational speed. Thickness noise can be represented by a rotating monopole source distribution and becomes important at high speeds. Thin blade sections and planform sweep are used to control this noise;
- Loading noise is a combination of thrust and torque (or lift and drag) components which result from the pressure field that surrounds each blade as a consequence of its motion. This pressure disturbance moving in the medium propagates as noise. Loading noise is an important mechanism at low to moderate speeds;
- For moderate blade section speed, the thickness and loading sources are linear and act on the blade surfaces. When flow over the blade sections is transonic, nonlinear effects can become significant. In aeroacoustic theory these can be modelled with quadrupole sources distributed in the volume surrounding the blades. The quadrupole could be used to account for all the viscous and propagation effects not covered by the thickness and loading sources.

### 3.2.2 Broadband noise

The broadband noise of a rotor is due to random aerodynamic interactions with turbulence either produced by the interaction of the atmospheric or inflow turbulence with the rotor, or produced by the rotor itself (boundary layers, wakes and tip vortices) (figure 3.3).

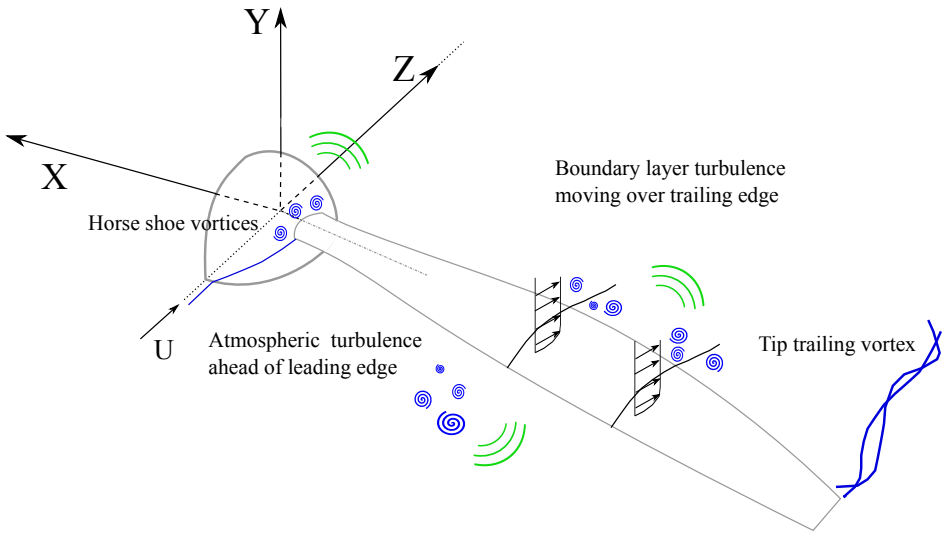


Figure 3.3: Main flow features around propeller blade.

Depending on the propeller design and operating conditions, three mechanisms appear [1]:

– The unsteady aerodynamics of the rotor blade when its leading edge interacts with the inflow turbulence, referred to as turbulence interaction noise. Because the inflow is turbulent, the resulting noise is random. The importance of this noise source depends on the magnitude of the inflow turbulence, it can be significant under conditions of high turbulence and low speeds;

– The acoustic radiation by the trailing edge of a blade when swept by boundary layer disturbances. A typical propeller develops a turbulent boundary layer over the blade surfaces, which can result in fluctuating blade loading at the trailing edge. The noise is characterised by the boundary layer properties. This mechanism is often important in clean incident flows, for which the turbulence interaction noise does not occur;

– Blade tip vortices and leakage flows also induce random fluctuations on propeller

blades, responsible for additional noise sources.

## 3.3 Prediction methods for propeller broadband noise

The noise from rotating blades has been for years predicted by the acoustic analogy, using more or less accurate flow predictions as input data. Modern methods can be developed following two strategies: solving the full fluid dynamics equations by extending Computational Aero-Acoustics (CAA) methods, or developing hybrid methods coupling CFD tools with acoustical post-processing methods based on the acoustic analogy [64]. However, even though these methods are powerful, they do not provide a simple and reliable tool that could be used in an industrial design cycle [67].
Analytical approaches remain attractive when dealing with rotating blades noise studies for two reasons. First, the present state of numerical approaches hardly accommodates for the full 3D configurations encountered in practice, in terms of computational time. Then the analytical methods run faster and can be used at the pre-design stage. But the main point is that the analytical solutions help to define the amount of accuracy needed in the flow data to get good acoustic results. This information is useful also to define the criteria of a numerical approach [64]. Analytical approaches relate the noise power spectral density in the far field at a given observer position and for a given frequency to some statistics in the flow. More precisely, turbulence interaction noise is deduced from a statistical description of the incident turbulent velocity field [49, 68] and trailing edge noise is deduced from a statistical description of the wall pressure fluctuations field near the trailing edge [13].
Amiet's [16] analytical approach for predicting broadband noise from rotating blades has been widely used for its simplicity. It consists of approximating the circular motion of the blades by a series of translations of the blades over an infinitesimally short distance. This approach was proved to be valid at high frequencies and low rotor speed, where the effects of rotation on the noise are small. Amiet's method has been first applied to the leading edge rotor noise by Paterson and Amiet [17] and to trailing edge rotor noise by Schlinker and Amiet [18]. This formulation has since been extensively

used in recent years and applied to the prediction of leading edge and trailing edge broadband noise of low-speed fans [25,69], helicopter rotors [17,18], wind turbines [19] and open propellers broadband noise [70]. Later, the validity of the approximations made in Amiet's approach has been studied in detail and validated for propellers trailing edge noise by Blandeau et al. [20]

## Time-domain and frequency-domain methods

Propeller noise prediction theories are divided into two groups: time-domain and frequency-domain methods. Time-domain methods solve the wave equation directly in terms of the space-time variables and yield a time record for a given number of revolutions of the propeller. They are advantageous because they can treat the blade geometry with any desired level of precision. If noise harmonics are needed, the time signal is Fourier transformed numerically. However, this type of prediction requires numerical differentiations and the calculation of retarded times that are computationally expensive. Frequency-domain methods eliminate time from the wave equation by means of Fourier transformation. The transformation causes a loss in precision in the representation of the blade geometry but this loss is generally acceptable for harmonics to a higher order. Furthermore, it gives rise to Bessel functions which are indicators of radiation efficiency. Harmonics are computed one at a time and the time signal is generated by summing a Fourier series [1].

For prediction purposes, the decision of which method will be used is usually made on grounds of convenience. Time-domain methods are difficult to implement and usually work by calculating the sound from one blade and then summing suitably shifted records, one for each blade, to find the net signal from the rotor. While for frequency-domain methods, which are easier for mathematical analysis, only the strength of harmonics need to be calculated. Overall, there is no particular preferred method for low speed, low blade number rotors.

## 3.4 Amiet's analytical formulation

In this thesis, Amiet's extended model, which assumes finite span and accounts for the leading edge back scattering, is used to predict noise from straight blades and validate the formulation implemented to predict noise from serrated trailing/leading edge noise. Therefore, a detailed description of the analytical formulation will be presented in this section.

### Schwarzschild's solution

Let $\Phi$ be a 2D scalar field solution of the following wave problem:

$$\begin{aligned} &\frac{\partial^2\Phi}{\partial x^2} + \frac{\partial^2\Phi}{\partial z^2} + \mu^2\Phi = 0 \\ &\Phi(x,0) = f(x) \qquad\qquad x \geq 0 \\ &\frac{\partial\Phi}{\partial z}(x,0) = f(x) \qquad\qquad x < 0 \end{aligned}$$

Then for any $x < 0$

$$\Phi(x,0) = \frac{1}{\pi}\int_0^\infty G\left(x,\xi,0\right) f(\xi) d\xi$$

With

$$G\left(x,\xi,0\right) = \sqrt{\frac{-x}{\xi}}\frac{e^{-i\mu(\xi-x)}}{\xi - x}$$

When addressing scattering problems, Amiet applies this result to determine the disturbance wall pressure generated when an incident vortical velocity field impinges on the leading edge of an airfoil [49] or when an incident wall pressure field is convected past the trailing edge [13].

Amiet's development starting point is a 2D Fourier decomposition of the incident wall pressure, defining pressure gusts with wave fronts parallel to the trailing edge, induced by the boundary layer developing on a flat plate with zero thickness and angle of attack, and with chord length $c = 2b$. The observer position is defined by a coordinate system centred at the trailing edge of the airfoil at the mid-span (figure 3.4).

The convected wave equation in the plane normal to the airfoil is written as

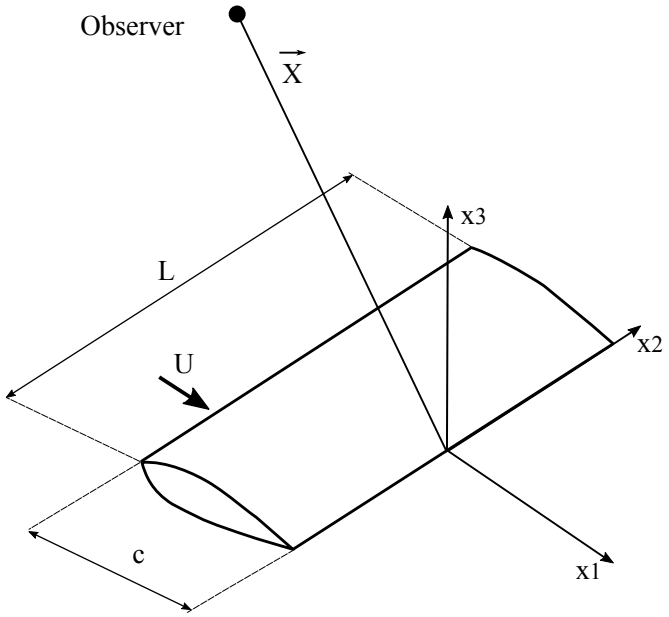


Figure 3.4: Coordinate system used in airfoil model.

$$\frac{\partial^2 p^{'}}{\partial x^2} + \frac{\partial^2 p^{'}}{\partial z^2} - \frac{1}{c_0^2}\left(\frac{\partial}{\partial t} + U\frac{\partial}{\partial x}\right)^2 p^{'} = 0 \tag{3.1}$$

with $p^{'}(x,z,t) = P(x,z)\,e^{i\omega t}$ is the disturbance pressure at reduced frequency $\omega$. Therefore, the complex equation is obtained

$$\beta^2\frac{\partial^2 P}{\partial x^2} + \frac{\partial^2 P}{\partial z^2} - 2ikM\frac{\partial P}{\partial x} + k^2 P = 0 \tag{3.2}$$

with $k = \omega/c_0$ and $\beta^2 = 1 - M^2$, $M = U/c_0$ is the free stream Mach number.

Performing the change of variable $P(x,z) = p(x,z)e^{i(kM/\beta^2)x}$ yields

$$\beta^2\frac{\partial^2 p}{\partial x^2} + \frac{\partial^2 p}{\partial z^2} + \left(\frac{KM}{\beta}\right)^2 p = 0 \tag{3.3}$$

with $k = KM$ and $K = \omega/U$. By further transforming the problem with

$X = \frac{x}{b}$, $Z = \frac{\beta z}{b}$, $\bar{K} = Kb$, $\bar{\mu} = \frac{\bar{K}M}{\beta^2}$

The canonical wave equation is obtained

$$\frac{\partial^2 p}{\partial X^2} + \frac{\partial^2 p}{\partial Z^2} + \bar{\mu}^2 p = 0 \tag{3.4}$$

Upstream of the trailing edge, the incident gust is written as $p^{'}(x,0,t) = e^{i\omega t}e^{-iK_1 x} = e^{i\omega t}e^{-i\alpha K x}$, with $\alpha = U/U_c$, $U_c$ being the convection velocity. This gust equals a pressure

difference on the two sides of the flat plate. The flat plate surface is assumed perfectly rigid. The application of the Kutta condition yields the following equations:

$$\frac{\partial \Delta P_1}{\partial Z}(X,0) = 0 \; X < 0 \tag{3.5a}$$

$$\Delta P_1(X,0) = -e^{-i\bar{K}X[\alpha+(M^2/\beta^2)]} \; X \geq 0 \tag{3.5b}$$

Equation (3.4) along with equations (3.5a) and (3.5b) is a Schwarzschild's problem [71]. The solution is written for $X < 0$ and $Z = 0$ as

$$\Delta P_1(X,0) = -\frac{e^{i\bar{\mu}X}}{\pi} \int_0^\infty \sqrt{\frac{-X}{\zeta}} \frac{e^{-i[\alpha\bar{K}+(1+M)\bar{\mu}]\zeta}}{\zeta - X} d\zeta \tag{3.6}$$

The preceding integral is calculated after manipulations [72] as

$$\int_0^\infty \sqrt{\frac{-X}{\zeta}} \frac{e^{-iA\zeta}}{\zeta - X} d\zeta = \pi e^{-iAX} \left[1 - \frac{e^{i\pi/4}}{\sqrt{\pi}} \int_0^{-AX} \frac{e^{-it}}{\sqrt{t}} dt\right] \tag{3.7}$$

Introducing the complex function

$$E^*(x) = \int_0^x \frac{e^{-it}}{\sqrt{2\pi t}} dt = C_2(x) - iS_2(x)$$

where $C_2$ and $S_2$ are Fresnel integrals [73]. Then since $\sqrt{2}e^{i\pi/4} = 1 + i$, we get for $X < 0$

$$\Delta P_1(X,0) = e^{-i\alpha\bar{K}X} \left[(1+i)\, E^*\left(-\left[\alpha\bar{K} + (1+M)\,\bar{\mu}\right] X\right) - 1\right] \tag{3.8}$$

Finally, expression (3.8) is written in terms of dimensional variables as

$$\Delta p_1(X,0,t) = e^{-i\alpha K x} \left[(1+i)\, E^*\left(-\left[\alpha K + (1+M)\, k/\beta^2\right] x\right) - 1\right] e^{i\omega t} \tag{3.9}$$

Equation (3.9) is the result derived by Amiet [13] for the pressure difference induced on a flat plate. It does not provide an exact solution, except for an infinite chord and does not take into account the the presence of the leading edge.

The far field sound spectrum approximated expression for an observer in the $x_2 = 0$ plane is therefore written as

$$S_{pp}(X,\omega) = \left(\frac{\omega b x_3}{2\pi c_0 S_0^2}\right)^2 l_y(\omega)\left|L(\omega)\right|^2 \Phi_{pp}(\omega) \tag{3.10}$$

This expression shows that Amiet's model requires the spanwise correlation length $l_y$ as a factor that quantifies the coherence between turbulent structures close to the trailing edge. The terms $\left(\frac{\omega b x_3}{2\pi c_0 S_0^2}\right)^2$ and $L(\omega)$ are, respectively, a dipole type radiation function to the observer location and the acoustically weighted airfoil response function that quantifies the unsteady load over the blade. $\Phi_{pp}(\omega)$ is the fluctuating pressure in the boundary layer of the airfoil close to the trailing edge.

## 3.5 Trailing edge noise formulae

The main theoretical contribution in [22] is a corrected form of the aeroacoustic transfer function $L$ that accounts for a leading edge correction. When the turbulent structures are scattered at the trailing edge, acoustic waves propagate upstream of the flow. Back-scattered waves from the trailing edge are then scattered again at the leading edge of the airfoil. A three-dimensional extension of Amiet's result has been achieved by taking three-dimensional gusts that can be factorized to apply the Schwarzschild's technique. The sound pressure PSD reads

$$\begin{aligned} S_{pp}^{TE}(\mathbf{x},\omega) = &\left(\frac{kcx_3}{4\pi S_0^2}\right)^2 2c \\ &\times \int_{-\infty}^{\infty} \Pi\left(\frac{\omega}{U_c}, K_2\right) sinc^2\left[\frac{L}{c}\left(\bar{K}_2 - \bar{k}\frac{x_2}{S_0}\right)\right] \left|L_{TE}\left(\frac{\bar{\omega}}{U_c}, K_2\right)\right|^2 dK_2 \end{aligned} \tag{3.11}$$

with $\bar{k} = kc/2$. The corresponding large aspect ratio approximation is

$$S_{pp}^{TE}(\mathbf{x},\omega) = \left(\frac{kcx_3}{4\pi S_0^2}\right)^2 2\pi L \left|L_{TE}\left(\frac{\bar{\omega}}{U_c}, \bar{k}\frac{x_2}{S_0}\right)\right|^2 \Pi\left(\frac{\omega}{U_c}, k\frac{x_2}{S_0}\right) \tag{3.12}$$

The statistical function $\Pi$ is related to the wall pressure spectrum $\Phi_{pp}$ upstream of the trailing edge for the assumed homogeneous boundary layer turbulence (see next section) and the associated spanwise correlation length $l_y$ by

$$\Pi\left(\frac{\omega}{U_c}, k_2\right) = \frac{1}{\pi}\Phi_{pp}(\omega)\, l_y(k_2,\omega)$$

The aeroacoustic transfer function is written as a sum of two terms $L_{TE} = I_{TE1} + I_{TE2}$ [74]. It has different expressions for the subcritical and supercritical gusts [22] corresponding to subsonic or supersonic phase speeds of their trace on the plate with respect to the incident mean flow, respectively. The main trailing-edge contribution is obtained as

$$I_{TE1} = -\frac{e^{2iC}}{iC}\left\{(1+i)\,e^{-2iC}\sqrt{\frac{B}{B-C}}E^*\left[2\left(B-C\right)\right] - (1+i)\,E^*\left[2B\right] + 1 - e^{-2iC}\right\} \tag{3.13}$$

with

$$C = \bar{K}_1 - \bar{\mu}\left(\frac{x_1}{S_0} - M\right), \quad B = \bar{K}_1 + M\bar{\mu} + \bar{\kappa}, \quad \bar{\kappa}^2 = \bar{\mu}^2 - \frac{\bar{K}_2^2}{\beta^2}, \quad \bar{K}_1 = \frac{\omega c}{2U_c} = K_1\frac{c}{2}$$

The leading edge back scattering correction is

$$I_{TE2} = H\left\{e^{4i\bar{\kappa}}\left[1-(1+i)\,E^*\left(4\bar{\kappa}\right)\right]\right\}^c - e^{2iD} + i\left[D + \bar{K} + M\bar{\mu} - \bar{\kappa}\right]G \tag{3.14}$$

with

$$H = \frac{(1+i)\,e^{-4i\bar{\kappa}}\left(1-\theta^2\right)}{2\sqrt{\pi}\left(\alpha-1\right)\bar{K}\sqrt{B}} \quad D = \bar{\kappa} - \bar{\mu}x_1/S_0 \quad \Theta = \sqrt{\frac{\bar{K}_1 + \bar{\mu}M + \bar{\kappa}}{\bar{K} + \bar{\mu}M + \bar{\kappa}}}$$

$$\begin{aligned} G = {} & (1+\epsilon)\,e^{i(2\bar{\kappa}+D)}\frac{sin\left(D-2\bar{\kappa}\right)}{D-2\bar{\kappa}} + (1-\epsilon)\,e^{i(-2\bar{\kappa}+D)}\frac{sin\left(D+2\bar{\kappa}\right)}{D+2\bar{\kappa}} \\ & + \frac{(1+\epsilon)\left(1-i\right)}{2\left(D-2\bar{\kappa}\right)}e^{4i\bar{\kappa}}E^*\left(4\bar{\kappa}\right) - \frac{(1-\epsilon)\left(1+i\right)}{2\left(D+2\bar{\kappa}\right)}e^{-4i\bar{\kappa}}E\left(4\bar{\kappa}\right) \\ & + \frac{e^{2iD}}{2}\sqrt{\frac{2\bar{\kappa}}{D}}E^*\left(2D\right)\left[\frac{(1+i)\left(1-\epsilon\right)}{D+2\bar{\kappa}} - \frac{(1-i)\left(1+\epsilon\right)}{D-2\bar{\kappa}}\right] \end{aligned}$$

The notation $\{\cdot\}^c$ means that the imaginary part must be multiplied by the factor $\epsilon = \left(\sqrt{1+1/(4\bar{\mu})}\right)^{-1}$.

For the sub-critical gusts ($\bar{\kappa}^2 < 0$), the solution read

$$I_{TE1}^{'} = -\frac{e^{-2iC}}{iC} \left\{ e^{-2iC} \sqrt{\frac{A_1^{'}}{\bar{\mu}(x_1/S_0) - i\bar{\kappa}^{'}}} \Phi^0 \left( \left[ 2i \left( \bar{\mu}(x_1/S_0) - i\bar{\kappa}^{'} \right) \right]^{1/2} \right) - \Phi^0 \left( \left[ 2iA_1^{'} \right]^{1/2} \right) + 1 \right\} \tag{3.15}$$

and

$$I_{TE2}^{'} = \frac{e^{-2iB^{'}}}{B^{'}} H^{'} \left\{ A^{'} \left( e^{2iB^{'}} \left[ 1 - erf\left( \sqrt{4\bar{\kappa}^{'}} \right) \right] - 1 \right) + \sqrt{2\bar{\kappa}^{'}} \left( \bar{K} + (M - x_1/S_0)\bar{\mu} \right) \frac{\Phi^0(\sqrt{-2iB^{'}})}{\sqrt{-iB^{'}}} \right\} \tag{3.16}$$

where $\Phi^0$ stands for the complementary error function of complex argument and where

$$H^{'} = \frac{(1+i)\left(1 - \Theta^{'2}\right)}{2\sqrt{\pi}\,(\alpha - 1)\,\bar{K}\sqrt{A_1^{'}}} \qquad A_1^{'} = \bar{K}_1 + M\bar{\mu} - i\bar{\kappa}^{'}$$

$$A^{'} = \bar{K} + M\bar{\mu} - i\bar{\kappa}^{'} \qquad \Theta^{'} = \sqrt{\frac{A_1^{'}}{A^{'}}}$$

$$B^{'} = \bar{\mu}\left(\frac{x_1}{S_0}\right) - i\bar{\kappa}^{'}$$

### 3.5.1 Wall pressure statistics models

The main input data for Amiet's model are the wall pressure statistics. The turbulent boundary layer is considered as the hydrodynamic excitation passing the trailing edge, the reorganization of the pressure field induces acoustic radiation. In the trailing edge noise model, the knowledge of the convection velocity, the spanwise coherence length and the wall pressure spectra just upstream of the trailing edge is necessary. The convection velocity is taken as $U_c = \alpha U$ with $0.6 < \alpha < 0.8$. The average value of $\alpha = 0.7$ will be used in the following sections. The spanwise coherence length is deduced from Corcos' model [75]:

$$l_y(\omega) = \frac{bU_c}{\omega} \tag{3.17}$$

The constant $b$ has to be determined experimentally. It has been found to be equal

to 1.4 for turbulent boundary layer over a flat plate with no pressure gradient [75]. In the case of an airfoil or a blade, this value was found to vary between 1.2 and 1.7 in different airfoil experiments [67]. The value of $b = 1.4$ is acceptable as a mean value.
The far field PSD is directly proportional to the wall pressure PSD. As the turbulent boundary layer is characterized by a large range of relevant length, velocity and pressure scales, numerous semi-empirical models have been developed. A two layer model is widely used to scale the turbulent boundary layer. The nearest flow to the wall, the viscous sub-layer, provides a first set of length, velocity and pressure scales; the outer layer, a second one. Based on this description, Keith et al. [76] compared the wall pressure spectra from various experiments in a normalized form. The high frequency range of the pressure spectra collapses when it is normalized by inner-layer scales, such as the wall shear stress $\tau_w$ for the pressure scale and $\nu/u_\tau^2$ for the time scale, with $\nu$ is the kinematic viscosity and $u_\tau$ the friction velocity. For low frequencies a collapse is observed with outer-layer scaling, such as the velocity at the boundary layer edge $U_e$, the boundary layer thickness $\delta$ or the boundary layer displacement thickness $\delta^*$. Based on these observations, three wall pressure statistics models are implemented in this study and then combined with RANS simulations providing the mean flow properties around the propeller blade to calculate the trailing edge noise.

**Schlinker and Amiet's model**

Based on data gathered from experiments, Schlinker and Amiet [18] proposed an analytical formulation using outer variables of the boundary layer:

$$\frac{\Phi_{pp}(\omega)}{\rho_0^2 \delta^* U_e^3} = 2.10^{-5} \frac{F(\tilde{\omega})}{2} \tag{3.18}$$

with $F(\tilde{\omega}) = (1 + \tilde{\omega} + 0.217\tilde{\omega}^2 + 0.00562\tilde{\omega}^4)^{-1}$, and $\tilde{\omega} = \frac{\omega \delta^*}{U_e}$.
Figure 3.5 compares the model with the data collected by Keith et al. [76] and scaled by the outer variables of the boundary layer. It can be seen that the model represents a good mean value while the data are spread out, in particular at high frequencies. At low frequencies, data collapse well globally.

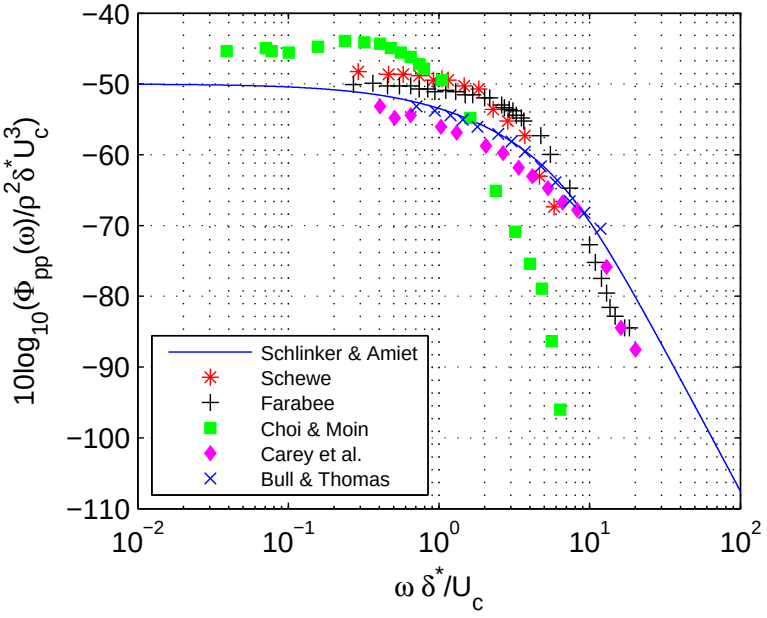


Figure 3.5: Wall pressure spectra scaled by outer variables. Schlinker and Amiet's model [18] vs data collected from experiments [77–81].

### Goody's model

Goody [29] proposed a wall pressure model which takes into account the effect of the Reynolds number using an empirical approach based on experimental results. In this model, the only effect of Reynolds number on the shape of the wall pressure spectrum is to increase the size of the overlap range. Moreover, $\delta$ is used instead of $\delta^*$ because the largest coherent structures are in the order of $\delta$. The final expression of the semi empirical model is

$$\frac{\Phi_{pp}(\omega)U_e}{\tau_w^2\delta} = \frac{C_2\tilde{\omega}^2}{[\tilde{\omega}^{0.75} + C_1]^{3.7} + [C_3\tilde{\omega}]^7} \tag{3.19}$$

where $\tilde{\omega} = \omega\delta/U_e$, $C_1$, $C_2$ and $C_3$ are empirical constants with the following recommended values: 0.5, 3.0 and $1.1R_T^{-0.57}$ respectively. $R_T = (\delta/U_e)/(\nu/u_\tau^2) = (u_\tau\delta/\nu)\sqrt{C_f/2}$ is the ratio of the outer to inner boundary layer time scale.

Figure 3.6 compares the wall pressure spectra calculated by Goody's model with experimental data. It can be seen that the model shows good agreement with experiments. Moreover, it has captured the spectral features correctly for zero pressure gradient turbulent flows over a wide range of Reynolds number. Discrepancies at high frequencies

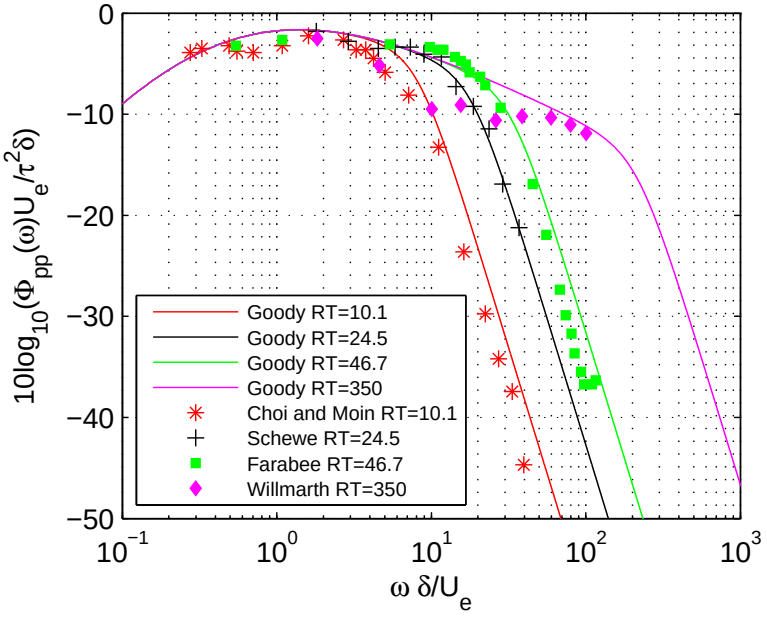


Figure 3.6: Wall pressure spectra scaled by mixed variables. Goody's model [18] vs data collected from experiments [79–82].

are related to the ratio of outer to inner layer timescale $R_T$ [30].

### Mean pressure gradient model

Based on Goody's model, Rozenberg et al. [30] proposed an empirical improved model taking into account the effect of an adverse pressure gradient on the wall pressure spectra expressed by:

$$\frac{\Phi_{pp}(\omega)U_e}{\tau_w^2\delta^*} = \frac{0.78(1.8\Pi\beta_c + 6)\,(\tilde{\omega})^2}{\left[(\tilde{\omega})^{0.75} + C_1'\right]^{3.7} + \left[C_3'\,(\tilde{\omega})\right]^7} \tag{3.20}$$

with $\tilde{\omega} = \omega\delta^*/U_e$, $C_1' = 0.105$, $C_3' = 3.76R_T^{-0.57}$, $\beta_c = (\theta/\tau_w)(dp/dx)$ is the Clauser's parameter [83] and $\Pi$ is the parameter of the wake's law defined by Coles [84] and obtained by solving the equation:

$$2\Pi - ln(1+\Pi) = \frac{\kappa U_e}{u_\tau} - ln\left(\frac{\delta^* U_e}{\nu}\right) - \kappa C - ln\kappa \tag{3.21}$$

with $\kappa = 0.41$ and $C = 5.1$.

Figure 3.7 compares the wall pressure spectra calculated by Schlinker and Amiet's model, Goody's model and the mean pressure gradient model with experimental data

of the CD airfoil [30]. The results show that the mean pressure gradient model gives a good approximation of the wall pressure spectrum around the airfoil over all the frequency range.

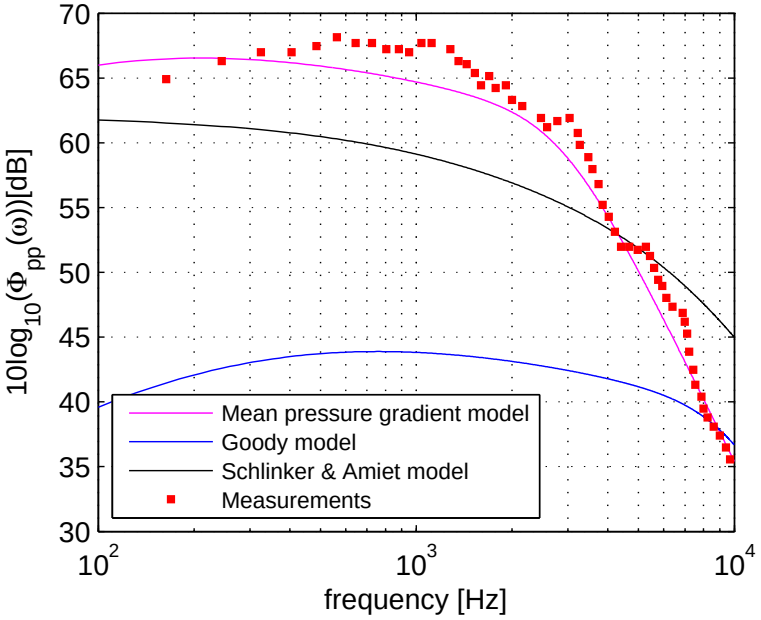


Figure 3.7: Wall pressure spectra comparison for the CD airfoil [30].

### 3.5.2 Models validation

The trailing edge model for a single airfoil with straight edge is validated by using the airfoil self noise data collected by Brooks and Hudgson [27]. The airfoil considered is a NACA0012 of chord $c = 0.6096m$ and span $L = 0.46m$, placed at zero angle of attack for two free stream velocities: $U = 38.6m/s$ and $U = 69.5m/s$. The boundary layer quantities are: $\delta^* = 4mm$, $U_c = 0.6U$ and $b = 1.724$ and $b = 1.613$ for the higher and the lower velocities respectively.

Figure 3.8 plots the sound pressure levels at a distance of $1.2m$ from the trailing edge obtained by using Schlinker and Amiet's model for wall pressure statistics. Both the frequency and velocity trends of the noise levels are well predicted by the present implementation of Amiet's formulation.

Amiet's formulation is also validated by using the parameters of two types of airfoils the V2 airfoil [85] which is a low subsonic profile designed for automotive cooling fans

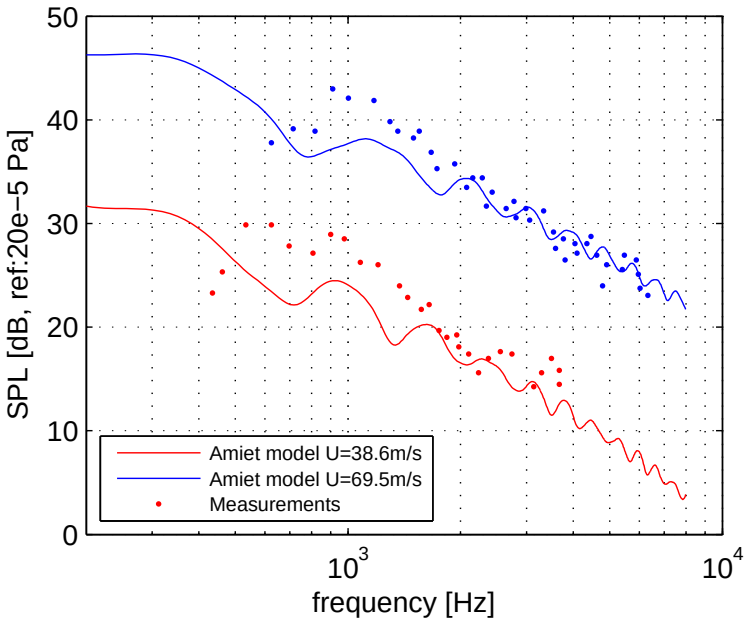


Figure 3.8: Comparison of the NACA 0012 trailing edge noise calculated by using Schlinker and Amiet's wall pressure spectrum model and the measurement obtained by Brooks and Hudgson [27].

and the low speed Controlled Diffusion (CD) airfoil [30]. The V2 and CD airfoils are of chord $c = 0.136m$ and span $L = 0.3m$, and are placed in an inflow velocity $U = 16m/s$. The sound radiated in the mid span plane ($\theta = 90^0$) has been measured at a distance of $1.2m$ for the V2 airfoil and $2m$ for the CD airfoil. The data of the boundary layer for the two airfoils are summarized in table 3.1.

| Boundary layer parameters | V2 airfoil | CD airfoil |
|---|---|---|
| $U_e(m/s)$ | 19.8 | 16.9 |
| $\delta(mm)$ | $3.87e-3$ | $4.98e-3$ |
| $\delta^*(mm)$ | $9.92e-4$ | $2.24e-3$ |
| $\theta(mm)$ | $5.59e-4$ | $8.76e-4$ |
| $\tau_w(Pa)$ | 0.72 | 0.11 |
| $\beta_c$ | 1.68 | 20.9 |
| $\Pi$ | 1.59 | 8.18 |

Table 3.1: V2 and CD Airfoils boundary layer parameters [30].

The three wall pressure spectral models are compared in figures 3.9 and 3.10. Schlinker and Amiet and Goody's models underestimate the pressure spectrum due to the mean pressure gradient effect not being taken into account in these forlulations. However,

the mean pressure gradient model provides a better agreement with the experimental results [30] over the whole range of frequencies when all the boundary layer parameters are determined.

Overall, Amiet's model combined with the wall pressure spectra models implemented in the present study, can predict the trailing edge noise of single airfoils. Schlinker and Amiet's model gives a good mean average of the acoustic spectrum shape whatever the conditions are but underestimates the noise levels. Goody's model works well with the zero-pressure gradient flows with the conditions to provide it the precise boundary layer parameters. For flows with adverse pressure gradient, Shlinker and Amiet and Goody's models underestimate the wall pressure spectrum directly affecting the far field noise spectrum when applied with the trailing edge model, while the use of the mean pressure gradient model improves the pressure level prediction and the shape of the spactra. It was demonstrated that this latter can be used for flows on the verge of separating, as long as they remain attached [30].

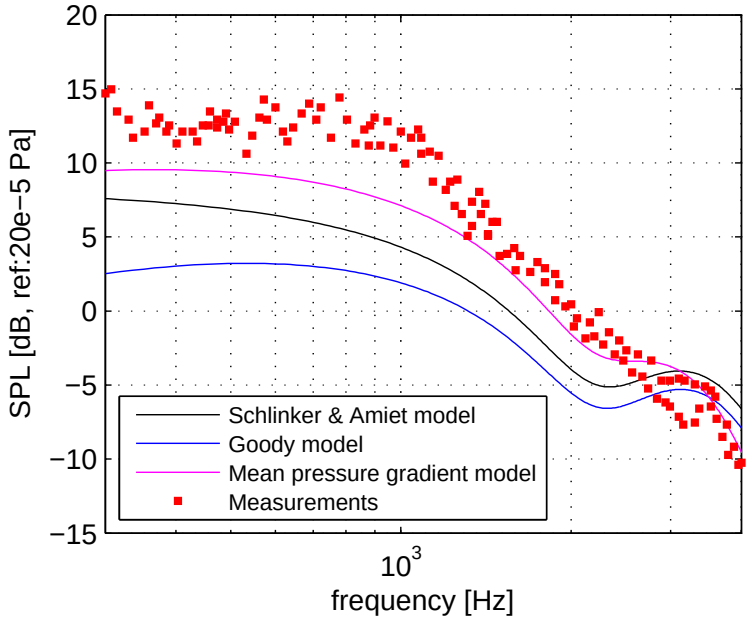


Figure 3.9: Trailing edge noise spectra in the mid-span plane of the V2 airfoil [85].

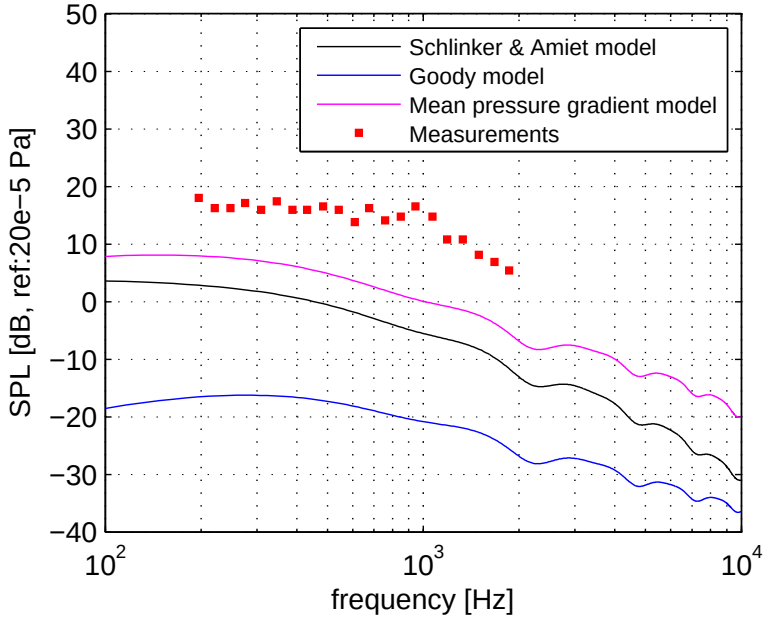


Figure 3.10: Trailing edge noise spectra in the mid-span plane of the CD airfoil [30].

## 3.6 Turbulence interaction noise formulae

Considering the airfoil configuration of figure 3.4 with the coordinate system centred at the leading edge, the far field sound PSD in the mid span is given by [74]

$$\begin{aligned} S_{pp}^{LE}(x,\omega) &= \left(\frac{k\rho c x_3}{2S_0^2}\right)^2 \\ &\times \pi U \frac{L}{2}\int_{-\infty}^{+\infty}\left[\Phi_{ww}\left(\frac{\omega}{U},K_2\right)\left|L_{LE}\left(x_1,\frac{\omega}{U},K_2\right)\right|^2 \frac{sin^2\left[\left(\frac{kx_2}{S_0}-K_2\right)\frac{L}{2}\right]}{\pi\frac{L}{2}\left(\frac{kx_2}{S_0}-K_2\right)^2}\right]dK_2 \end{aligned} \tag{3.22}$$

where $L_{LE}$ is the non-dimensional chordwise aeroacoustic transfer function [49]. $S_0 = [x_1^2+\beta^2(x_2^2+x_3^2)]^{1/2}$ is the convection corrected distance. $\Phi_{ww}(K_1,K_2)$ is the two dimensional wavenumber spectrum of the incident turbulence, and $K_1=\omega/U$ is imposed by the frozen turbulence assumption.

The transfer function $L_{LE}$ has different expressions for the subcritical and supercritical gusts [22] corresponding to subsonic or supersonic phase speeds of their trace on the plate with respect to the incident mean flow, respectively. Very often, only the large aspect ratio approximation is considered:

$$S_{pp}^{LE}(x,\omega) = \left(\frac{\rho k c x_3}{2S_0^2}\right)^2 \pi U \frac{L}{2}\Phi_{ww}\left(\frac{\omega}{U},\frac{kx_2}{S_0}\right)\left|L_{LE}\left(x_1,\frac{\omega}{U},\frac{kx_2}{S_0}\right)\right|^2 \tag{3.23}$$

The transfer function is a sum of two contributions $L_{LE}=L_{LE1}+L_{LE2}$. For sub-critical gusts corresponding to $\Theta_0<1$

$$L_{LE1} = -\frac{1}{\pi}\sqrt{\frac{2}{\left(\bar{K}_1+i\beta^2\bar{\kappa}'\right)i\Theta_3}}e^{-i\Theta_2}E\left[2i\Theta_3\right] \tag{3.24}$$

$$\begin{aligned} L_{LE2} &= \frac{e^{-i\Theta_2}}{\pi\sqrt{2\pi\left(\bar{K}_1+i\beta^2\bar{\kappa}'\right)\Theta_3}} \\ &\times\left\{1-e^{-2\Theta_3}-erf\left(\sqrt{4\bar{\kappa}'}\right)+2e^{-2\Theta_3}\sqrt{\frac{\bar{\kappa}'}{i\bar{\kappa}'+\bar{\mu}x_1/S_0}}E\left[2\left(i\bar{\kappa}'+\bar{\mu}x_1/S_0\right)\right]\right\} \end{aligned} \tag{3.25}$$

where

$$\Theta_0 = \frac{\bar{K}_1 M}{\beta \bar{K} 2}$$

$$\Theta_2 = \bar{\mu}\left(M - x_1 S_0\right) - \frac{\pi}{4} \qquad \Theta_3 = \bar{\kappa}^{'} + i\bar{\mu}\frac{x_1}{S_0}$$

$$\bar{\kappa}^{'} = \sqrt{\frac{\bar{K}_2}{\beta^2} - \bar{\mu}^2} \qquad \bar{\kappa}^{'2} = \bar{\mu}^2\left(\frac{1}{\Theta_0^2} - 1\right)$$

$$\bar{\mu} = \frac{kc}{2\beta^2} = \frac{\bar{K}_1 M}{\beta^2} \qquad \bar{K}_j = \frac{K_j c}{2}$$

$E$ is related to the Fresnel integrals: $E(\xi) = \int_0^{\xi} \frac{e^{it}}{\sqrt{2\pi t}} dt$

For the supercritical gusts where $\Theta_0 > 1$ and $\bar{\kappa}^{'2} < 0$

$$L_{LE1}^{'} = -\frac{1}{\pi}\sqrt{\frac{2}{\left(\bar{K}_1 + \beta^2\bar{\kappa}\right)\Theta_4}} e^{-i\Theta_2} E\left[2\Theta_4\right] \tag{3.26}$$

$$L_{LE2}^{'} = \frac{e^{-i\Theta_2}}{\pi\sqrt{2\pi\left(\bar{K}_1 + \beta^2\bar{\kappa}\right)\Theta_4}}$$
$$\times \left\{ i\left(1 - e^{2i\Theta_4}\right) - (1+i)\left[E(4\bar{\kappa}) - e^{2i\Theta_4}\sqrt{\frac{2\bar{\kappa}}{\bar{\kappa} + \bar{\mu}x_1/S_0}} E\left[2\left(\bar{\kappa} + \bar{\mu}x_1/S_0\right)\right]\right]\right\}$$

with

$$\Theta_4 = \bar{\kappa} - \bar{\mu}\frac{x_1}{S_0}$$

In this study, the Von Karman model for the isotropic turbulence $\Phi_{ww}$ is adopted. This model has been validated by experimental measurements in [69].

$$\Phi_{ww}\left(\frac{\omega}{U_0}, 0\right) = \frac{U_0}{\pi}\phi_{ww}(\omega) l_y(\omega) \tag{3.28}$$

The PSD of the velocity fluctuations $\phi_{ww}$ and the correlation length of the velocity $l_y$ [69] are defined as:

$$\phi_{ww}(\omega) = \frac{\bar{u}^2 L_t}{6\pi U_0} \frac{3 + 8\left(\frac{K}{k_e}\right)^2}{\left[1 + \left(\frac{K}{k_e}\right)^2\right]^{11/6}} \tag{3.29}$$

$$l_y(\omega) = \frac{8Lt}{3}\left(\frac{\Gamma(1/3)}{\Gamma(5/6)}\right)^2 \frac{\left(\frac{K}{k_e}\right)^2}{\left[3+8\left(\frac{K}{k_e}\right)^2\right]\sqrt{1+\left(\frac{K}{k_e}\right)^2}} \tag{3.30}$$

with $k_e = \frac{\sqrt{\pi}}{L_t}\frac{\Gamma(5/6)}{\Gamma(1/3)}$, $K = \frac{K_1}{k_e}$ and $\Gamma$ the Euler's gamma function. $\bar{u}^2$ denotes the rms value of the streamwise velocity fluctuations and $L_t$ is the integral scale of the turbulent streamwise velocity.

### Model validation

The leading edge noise model is validated by using the airfoil turbulence interaction noise data collected by Paterson and Amiet [68]. A NACA0012 airfoil of chord $c = 0.23m$ and span $L = 0.53m$ at zero incidence is tested at five free-stream velocities in the range $40 - 165m/s$. The sound pressure levels at a distance of $2.25m$ from the leading edge are shown in figure 3.11. The analytical results have been obtained by assuming the measured turbulence intensity and integral length scale. The spectra show that the frequency and velocity trends of the noise levels are quite well predicted, and that the confidence level of the prediction is about $3dB$ in the maximum noise frequency range.

Figure 3.12 presents the predicted acoustic far field spectrum of the turbulence interaction noise of the V2 airfoil, compared to the experimental results [85]. The model is used with turbulence length scale $L_t = 0.009m$ and turbulence intensity $Tu = 5\%$ at observer position $R = 2m$ and $\theta = 90^o$ . It can be seen that the agreement is good in the low frequencies however, the model overpredicts the SPL levels at high frequencies due to thickness effects not taken into account in this implementation .

## 3.7 Extension of the single airfoil model to rotating blades

Since the relative mean flow and the aerodynamic parameters on a blade vary along the span, the analytical models are applied by means of a strip theory approach [17,25]. The blade is split into segments as suggested in Figure 3.13, each of which is attributed a set of appropriate input parameters. The contributions to the far field sound are calculated

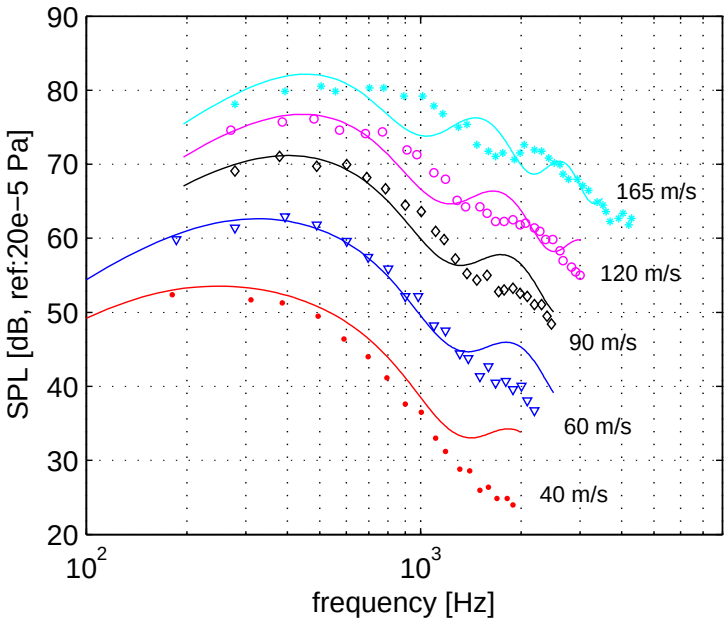


Figure 3.11: NACA0012 interaction noise measurements [68] (symbols) are compared to semi-analytical results (lines) at different free-stream velocities.

for each segment considered as an isolated airfoil and summed as uncorrelated. In this approach, the motion of a blade segment relative to the observer is introduced as a correction by assuming the rotating motion locally equivalent to a translation motion. The relative motion of the blade is then taken into account by adding a Doppler factor. [18]

### 3.7.1 Expression of the Doppler factor

The blade segment rotates around $Z$ axis with the angular velocity $\Omega$ where $\Omega t = \Psi$ as illustrated in figure 3.13. The blade is placed in a flow of axial velocity $U_z$. The observer position in the moving reference frame is defined by the vector sum $\vec{x} = \vec{R_0} - \vec{R_A}$ where $\vec{R_A} = (0, R, 0)$ denotes the middle of the trailing edge in the $(x_1, x_2, x_3)$ coordinates system.

The first step is to calculate the retarded time and position. At $t = 0$, a fictive marker is placed on the acoustic source i.e. on the blade segment. At $t = T_e$, the observer hears the sound emitted at $t = 0$. The marker displacement is $\vec{x_s}$. The observer is located by $\vec{x_0} = R_0(sin\Theta\vec{i} + cos\Theta\vec{k})$. He is placed at a distance $r_e$ from the source

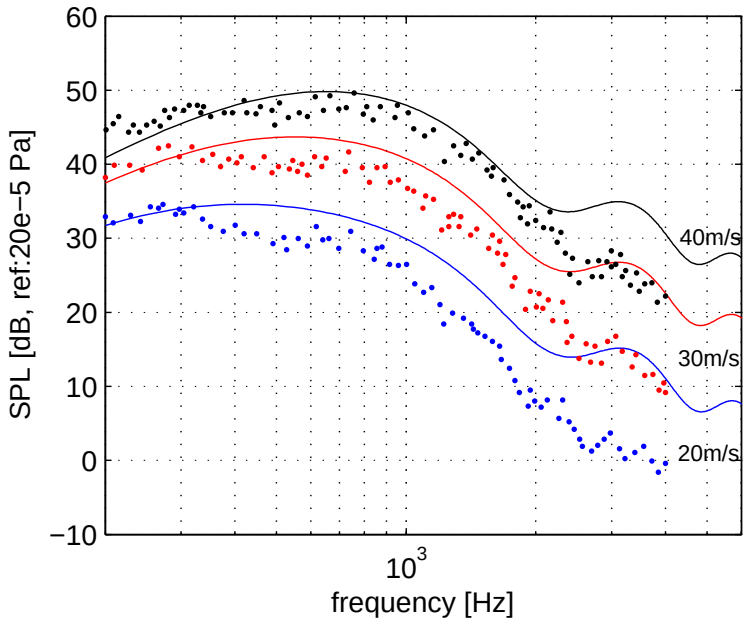


Figure 3.12: Turbulence interaction predictions compared to measurements for the V2 airfoil [85] in the mid-span plane.

point at the retarded time $T_e$:

$$r_e^2 = (R_0 sin\Theta - x_s)^2 + y_s^2 + (R_0 cos\Theta - z_s)^2 \tag{3.31}$$

where $T_e = r_e/c_0$, $\vec{x_s} = (0, 0, M_z r_e)$ and $M_z = U_z/c_0$ is the axial Mach number. The solution of equation 3.31 reads

$$r_e = \frac{R_0}{1 - M_z^2}\left(-M_z cos\Theta + \sqrt{1 - M_z^2 sin^2\Theta}\right) \tag{3.32}$$

The instantaneous emitted frequency $\omega_e(\Psi)$ at the current position $\Psi = \Omega t$ is related to the received frequency $\omega(\Psi)$ by the Doppler factor as

$$\frac{\omega}{\omega_e} = 1 + \frac{\vec{M}_t.\widehat{OS}}{1 - \vec{M}_r.\widehat{OS}} \tag{3.33}$$

where $M_r$ is the Mach number of the source relative to the fluid, $M_t = \Omega r/c_0$ is the Mach number of the source relative to the observer, and $\widehat{OS} = \frac{\vec{OS}}{|\vec{OS}|}$ is the unit vector from the retarded source position to the observer.

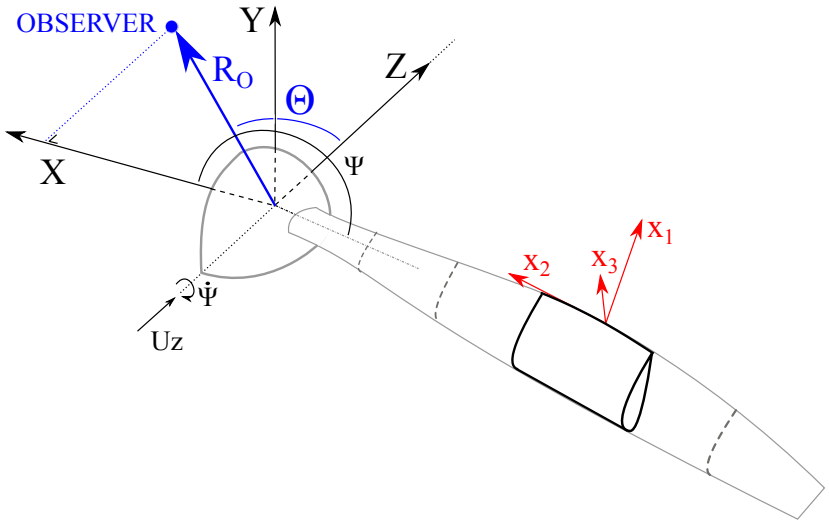


Figure 3.13: Coordinates system used in the rotating blade model.

$$\vec{M_t} = M_t \left(-sin\Psi\vec{i} + cos\Psi\vec{j}\right)$$
$$\vec{M_r} = -M_t sin\Psi\vec{i} + M_t cos\Psi\vec{j} - M_z\vec{k}$$
$$\vec{OS} = (x - x_s)\,\vec{i} + (y - y_s)\,\vec{j} + (z - z_s)\,\vec{k}$$
$$\widehat{OS} = \frac{x}{r_e}\vec{i} + \left(\frac{z}{r_e} - M_z\right)\vec{k}$$

Finally, the Doppler factor is expressed by

$$\frac{\omega}{\omega_e} = 1 + \frac{-M_t x sin\Psi}{r_e(1 - M_z^2) + M_t x sin\Psi + M_z z} \tag{3.34}$$

Replacing $r_e$ by its expression (equation 3.32), this result is simplified by

$$\frac{\omega_e}{\omega} = 1 + \frac{M_t sin\Psi sin\Theta}{\sqrt{1 - M_z^2 sin^2\Theta}} \tag{3.35}$$

The far-field noise PSD for a rotor with B independent blades is calculated by averaging over all possible angular locations of the blade segments and by weighting with the Doppler factor:

$$S_{pp}^{\Psi}(\vec{X}, \omega) = \frac{B}{2\pi}\int_0^{2\pi}\left(\frac{\omega_e(\Psi)}{\omega}\right)^2 S_{pp}^{\Psi}(\vec{x}, \omega_e)d\Psi \tag{3.36}$$

where $S_{pp}^{\Psi}(\vec{x}, \omega)$ is given by the single airfoil theory with the observer coordinates defined in the $(x_1, x_2, x_3)$ local coordinates system relative to the trailing/leading edge.

The exponent of the Doppler shift in formulation (3.36) is different from the one derived by Amiet. A comparative study conducted by Sinayoko et al. [21] highlighted that it should take a value of 2 rather than 1 in Amiet [16] and Rozenberg et al. [25] and -2 in Schlinker and Amiet [18] so that it accounts for the the additional weighting of the time increment when averaging the instantaneous PSD.

### 3.7.2 Validation

The implementation of the analytical trailing edge noise model for a single airfoil combined to the strip approach is applied to the fan test case presented in [24]. For the wall pressure statistics, the models of Schlinker and Amiet and Goody are used. Results are calculated at $R = 1.7m$ for the microphone angle $\Theta = 60^0$. The blade is taken as one segment.

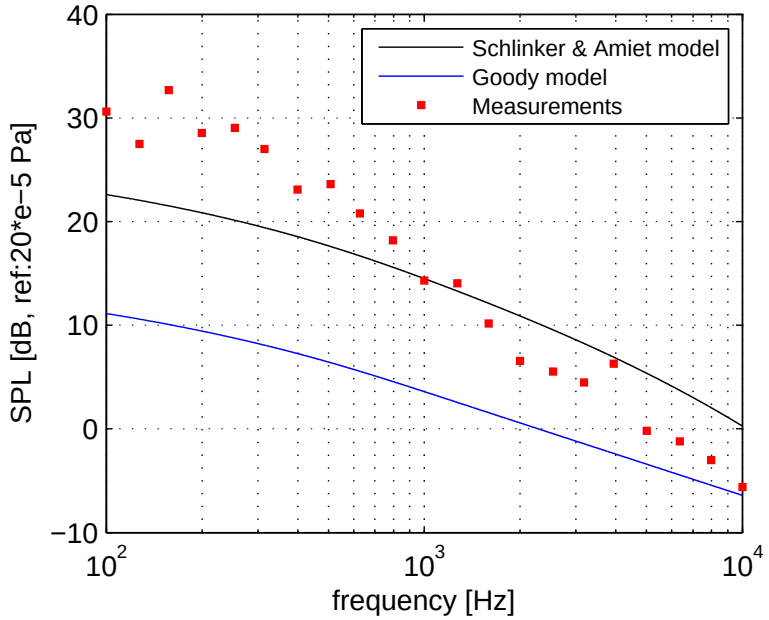


Figure 3.14: Acoustic spectrum for the compressor.

The spectra presented in figure 3.14 show that the model of Schlinker and Amiet predicts with a good agreement the tendency and the SPL levels compared to experiment data, whereas Goody's model underpredicts the SPL levels.

The strip approach is justified as far as the characteristic sound frequencies remain high enough when compared to the rotational frequency and hold as well for other

broadband noise mechanisms [74]. Reliable results have been obtained this way for fan, helicopter and propeller blades [17, 18, 86]. Note that the single airfoil theories are devoted to subsonic rotating blade noise predictions.

# *Chapter 4*
# *Numerical modelling and simulations set up*

# Chapter 4
# Numerical modelling and simulations set up

## 4.1 Introduction

The significant advances that have recently been made in numerical techniques and computer hardware have made a major influence on the approaches used to understand and predict noise generated by unsteady flows. The use of Direct Numerical Simulation (DNS) of aerodynamic noise requiring the full Navier-Stokes equations is possible but it is time consuming and given its huge numerical cost can be used only for simplified configurations, where it can help to better understand the basic noise generating mechanisms. Large Eddy Simulation (LES) can be more appropriate but still remains far from industrial applications and requires a high level of expertise. Less sophisticated averaged approaches, such as Reynolds-Averaged Navier-Stokes (RANS) computations, are currently widely used, but do not provide an explicit description of the random fields that would be required to predict the broadband noise [64]. To overcome these problems, hybrid approaches, coupling efficient CFD tools and some acoustical post-processing based on the acoustic analogy are used.
Meanwhile, a new approach based on the kinetic equation has evolved and made significant progress over the past decade [87, 88]. The Lattice Boltzmann Method (LBM) has developed into an alternative and promising numerical scheme for simulating fluid flows and modelling physics in fluids. Unlike conventional numerical schemes based on discretizations of macroscopic continuum equations, the LBM is based on microscopic models and mesoscopic kinetic equations. The base of this approach is the construction of simplified kinetic models incorporating only the essential physics of microscopic or mesoscopic processes so that the macroscopic averaged properties obey the desired macroscopic equations [89]. The basic premise for using these simplified kinetic-type methods for macroscopic fluid flows is that the macroscopic dynamics of a fluid is the result of the collective behaviour of many microscopic particles in the system and that the macroscopic dynamics is not sensitive to the underlying details in microscopic

physics. The LBM originates from Lattice Gas Automata (LGA) which replaces the macroscopic picture underlying the Navier-Stokes framework by discrete sets of fictive particles carrying some properties of real fluid portions regarded as coarse-grained groups of fluid (or gas) molecules [90]. The fluid portions in the lattice gas move at different speeds in different directions on a fixed lattice and interact by simple local rules. During each time step they move according to their current momentum vector. If two particles happen to end up on the same lattice site, they collide and change their velocities according to a set of discrete collision rules. The only restriction is that collisions have to conserve the particle number, the momentum and the energy [91]. Using this small set of rules offers the first and coarsest way of approximating fluid dynamics in terms of lattice gas automata.

The capability of the LBM has been validated for many aerodynamics [92–94] and aeroacoustics [95,96] applications. It has been demonstrated that it presents advantages over the Navier-Stokes based methods [97]:

- LBM is based on a simpler representation of the flow physics and the algorithmic implementation is hence less complicated;
- LBM is most efficiently implemented on Cartesian grids;
- LBM is inherently unsteady, it is about one order less expensive than Navier-Stokes methods;
- LBM offers low numerical dissipation which makes it well suited for simulations of wake and detached flows and for aeroacoustics;
- LBM is easily parallelized and can run efficiently on modern HPC architectures.

The Lattice-Boltzmann method, including its implementation in the commercial software PowerFLOW as it was used for the simulations presented in the manuscript, is detailed in the next sections.

## 4.2 The Lattice-Boltzmann approach

To understand the physics behind the LBM, we first point out that a fluid can be described on three levels: the molecular level at which motion, usually Hamiltonian, is reversible; the kinetic level, in the irreversible low-density Boltzmann approximation;

and the macroscopic level, in the continuum approximation (figure 4.1). At the first two levels of description, the fluid is near thermodynamic equilibrium. In the last, there are free thermodynamic variables: local density, momentum, temperature, etc. [98].

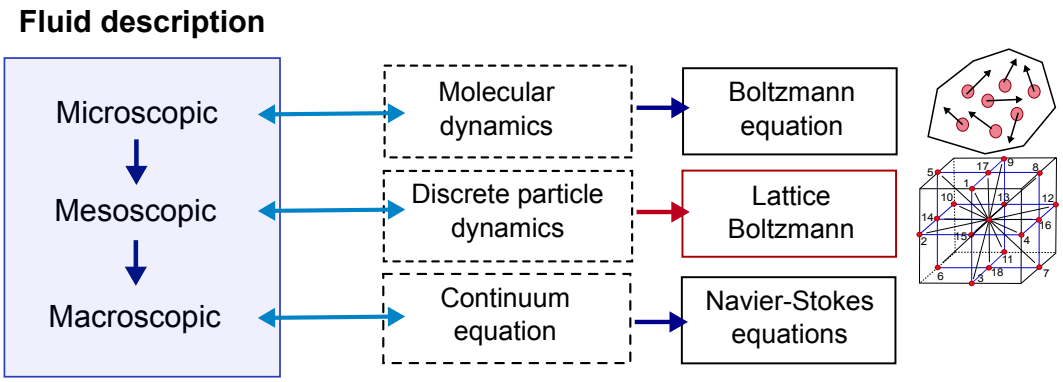


Figure 4.1: Physics representations of fluids adapted from [97].

The LBM is based on a simple and more general physics formulation compared to methods based on the Navier-Stokes (N-S) equations [97]. Its motivation is to simulate a fluid at a microscopic level where the physics is simpler and more general than the macroscopic, continuum approach taken by the N-S equations. However, as the complete microscopic reproduction of molecular dynamics is computationally expensive, a simplified mesoscopic description is constructed.

### 4.2.1 Mesh type for the LBM

Lattice Boltzmann models are spatially discrete approaches to fluid dynamics. This means that the underlying grids of such simulations must fulfil certain symmetry conditions in order to recover hydrodynamic behaviour with full rotational symmetry of space [90] i.e.

$$\begin{aligned}
&\sum_{i=0}^{M} w_i = 1, \qquad \sum_{i}^{M} w_i e_{i\alpha} = 0, \\
&\sum_{i=0}^{M} w_i e_{i\alpha} e_{i\beta} = \Pi^{(2)} \delta_{\alpha\beta}, \qquad \sum_{i}^{M} w_i e_{i\alpha} e_{i\beta} e_{i\gamma} = 0, \\
&\sum_{i=0}^{M} w_i e_{i\alpha} e_{i\beta} e_{i\gamma} e_{i\theta} = \Pi^{(4)} \left( \delta_{\alpha\beta}\delta_{\gamma\theta} + \delta_{\alpha\gamma}\delta_{\beta\theta} + \delta_{\alpha\theta}\delta_{\beta\gamma} \right)
\end{aligned} \tag{4.1}$$

where $w_i$ represent weight factors which must be properly chosen for each grid type in order to correct the lattice with respect to isotropy, $e_i$ are the lattice vectors with the Greek indices $\alpha, \beta, \gamma$ and $\theta$ for the spatial directions, and $\Pi^{(2)}$ and $\Pi^{(4)}$ are lattice constants which are related to the lattice sound speed.

The most frequent mesh types for lattice Boltzmann simulations are the $D2Q9$ and the $D3Q19$ lattice, shown in figure 4.2. The terminology $D_kQ_n$ refers to the number k of dimensional sub-lattices and to the discrete number n of spatial translation vectors $e_i$ constituting the vector basis of the distribution function. In three dimensions, isotropy generally requires a multi-speed lattice [90].

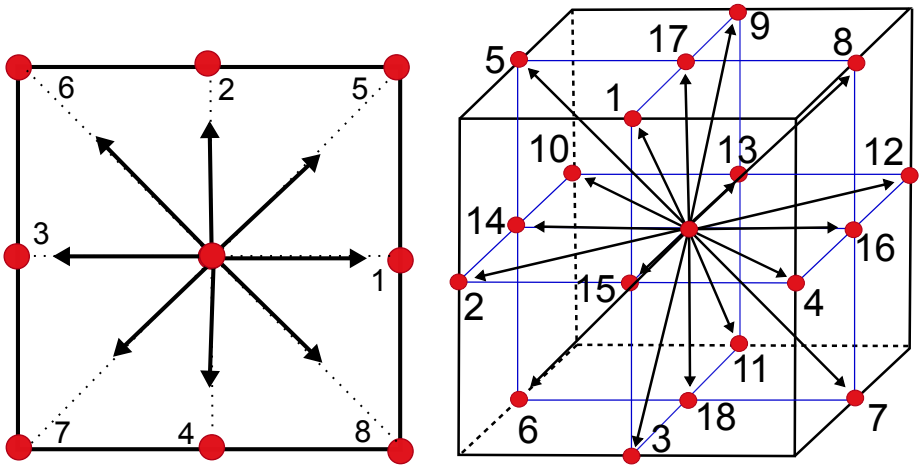


(a) The $D2Q9$ model. (b) The $D3Q19$ model.

Figure 4.2: Illustration of the lattice nodes in LBM [97, 99].

Note that the PowerFLOW solver uses the $D3Q19$ model [100]. The $D3Q19$ lattice has 3 sub-lattices and 19 discrete velocity vectors (identity, 6 velocities to the face centres and 12 towards edge centres of a cube).

### 4.2.2 Lattice-Boltzmann equations

The fundamental idea is that gases/fluids can be imagined as consisting of a large number of small particles moving randomly. The exchange of momentum and energy is achieved through particle movement and billiard like particle collision. Starting from an initial state, the configuration of particles at each time step evolves in two sequential sub-steps, (a) streaming, in which each particle moves to the nearest node in

the direction of its velocity, and (b) collision, which occurs when particles arriving at a node interact and change their velocity directions according to scattering rules [90]. The Lattice-Boltzmann Equation is introduced beginning from a discrete kinetic equation for the particle distribution function

$$f_i\left(x + e_i\Delta x, t + \Delta t\right) - f_i\left(x, t\right) = \Omega_i\left(f\left(x, t\right)\right), \quad (i = 0, 1..., M) \tag{4.2}$$

where $f_i$ is the particle velocity distribution function along the ith direction; $\Omega_i = \Omega_i\left(f\left(x, t\right)\right)$ is the collision operator which represents the rate of change of $f_i$ resulting from collision. $\Delta t$ and $\Delta x$ are time and space increments, respectively. M is the number of directions of the particle velocities at each node and $e_i$ are the local particle velocities. The left hand term $f_i\left(x + e_i\Delta x, t + \Delta t\right) - f_i\left(x, t\right)$ is the advection term which represents free propagation of the particle packets along the lattice links. The term $f_i\left(x + e_i\Delta x, t + \Delta t\right)$ is the new distribution function after advection and redistribution.

The density $\rho$ and momentum $\rho u$ are defined as particle velocity moments of the distribution function, $f_i$

$$\rho = \sum_{i=1}^{M} f_i, \quad \rho u = \sum_{i=1}^{M} f_i e_i \tag{4.3}$$

If only the physics in the long-wave-length and low frequency limit are of interest, the lattice spacing $\Delta x$ and the time increment $\Delta t$ in equation (4.2) can be regarded as small parameters of the same order $\epsilon$. Performing a Taylor expansion in time and space, the following continuum form of the kinetic equation accurate to second order in $\epsilon$ is obtained:

$$\frac{\partial f_i}{\partial t} + e_i \cdot \nabla f_i + \epsilon\left(\frac{1}{2} e_i e_i \cdot \nabla\nabla f_i + e_i \cdot \nabla \frac{\partial f_i}{\partial t} + \frac{1}{2}\frac{\partial^2 f_i}{\partial t^2}\right) = \frac{\Omega_i}{\epsilon} \tag{4.4}$$

To derive the macroscopic hydrodynamic equation, the Chapman-Enskog expansion [90] is used

$$\frac{\partial}{\partial t} = \epsilon\frac{\partial}{\partial t_1} + \epsilon^2\frac{\partial}{\partial t_2}, \qquad \frac{\partial}{\partial x} = \epsilon\frac{\partial}{\partial x_1}$$

The above formula assumes that the diffusion time scale $t_2$ is much slower than the convection time scale $t_1$. Likewise, the one-particle distribution function $f_i$ can be expanded about the local equilibrium distribution function $f_i^{eq}$,

$$f_i = f_i^{eq} + \epsilon f_i^{neq} \tag{4.5}$$

$f_i^{eq}$ depends on the local macroscopic variables ($\rho$ and $\rho u$) and should satisfy the following constraints:

$$\sum_{i=1}^{M} f_i^{eq} = \rho, \quad \sum_{i=1}^{M} f_i^{eq} e_i = \rho u \tag{4.6}$$

$f_i^{neq} = f_i^{(1)} + \epsilon f_i^{(2)} + O(\epsilon^2)$ is the non-equilibrium distribution function, which has the following constraints:

$$\sum_{i=1}^{M} f_i^{k} = 0, \quad \sum_{i=1}^{M} f_i^{k} e_i = 0 \tag{4.7}$$

for both $k = 1$ and $k = 2$.

Inserting $f_i$ into the collision operator $\Omega_i$, the Taylor expansion gives:

$$\begin{aligned} \Omega_i\left(f\right) =& \Omega_i\left(f^{eq}\right) + \epsilon \frac{\partial \Omega_i\left(f^{eq}\right)}{\partial f_j} f_j^{(1)} \\ &+ \epsilon^2 \left( \frac{\partial \Omega_i\left(f^{eq}\right)}{\partial f_j} f_j^{(2)} + \frac{\partial^2 \Omega_i\left(f^{eq}\right)}{\partial f_j \partial f_k} f_j^{(1)} f_k^{(1)} \right) + O\left(\epsilon^2\right) \end{aligned} \tag{4.8}$$

From equation (4.4), when $\epsilon \longrightarrow 0$, $\Omega_i(f^{eq}) = 0$. This leads to a linearised collision operator,

$$\frac{\Omega_i(f)}{\epsilon} = \frac{M_{ij}}{\epsilon}\left(f_j - f_j^{eq}\right) \tag{4.9}$$

where $M_{ij} \equiv \frac{\partial \Omega_i(f^{eq})}{\partial f_j}$ is the collision matrix, which determines the scattering rate between directions i and j. For a given lattice, $M_{ij}$ only depends on the angle between directions i and j and has a limited set of values.

If the local distribution is assumed to relax to an equilibrium state at a single rate $\tau$,

$$M_{ij} = -\frac{1}{\tau}\delta_{ij} \tag{4.10}$$

The key steps in LBM are the streaming and collision processes. The two processes are computed separately, and special attention is given when dealing with boundary lattice nodes. The collision term is modelled using Bhatnagar-Gross-Krook (BGK) model [101]:

$$\frac{\Omega_i}{\epsilon} = -\frac{1}{\tau} f_i^{neq} = -\frac{1}{\epsilon\tau}\left(f_i^{(1)} + \epsilon f_i^{(1)}\right) \tag{4.11}$$

and the LBGK equation reads:

$$f_i\left(x + e_i, t + 1\right) = f_i\left(x, t\right) - \frac{f_i - f_i^{eq}}{\tau} \tag{4.12}$$

Figure 4.3 shows graphically how the particle movement step takes place for the interior nodes.

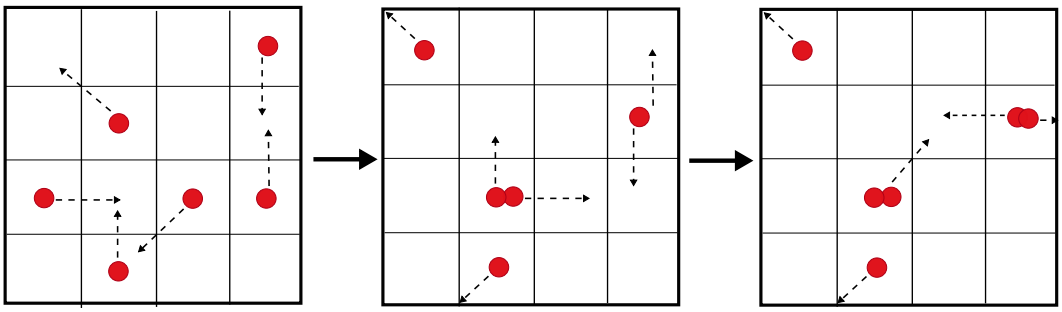


Figure 4.3: Process of particle streaming and collision adapted from [100].

From equation (4.4), the following equations are obtained:

$$\frac{\partial f_i^{eq}}{\partial t_1} + e_i \cdot \nabla_1 f_i^{eq} = -\frac{f_i^{(1)}}{\tau} \tag{4.13}$$

to order $\epsilon^0$ and

$$\begin{aligned} &\frac{\partial}{\partial t_1} f_i^{(1)} + \frac{\partial}{\partial t_2} f_i^{(eq)} + e_i \cdot \nabla f_i^{(1)} + \frac{1}{2} e_i e_i : \nabla\nabla f_i^{eq} \\ &\quad + e_i \cdot \nabla \frac{\partial}{\partial t_1} f_i^{eq} + \frac{1}{2}\frac{\partial^2}{\partial t_1^2} f_i^{eq} = \frac{1}{\tau} f_i^{(2)} \end{aligned} \tag{4.14}$$

to order $\epsilon^1$. Using equation (4.13) and some algebra, the first order equation can be written as

$$\frac{\partial f_i^{(1)}}{\partial t_2} + \left(1 - \frac{2}{\tau}\right)\left[\frac{\partial f_i^{(1)}}{\partial t_1} + e_i \cdot \nabla_1 f_i^{(1)}\right] = -\frac{f_i^{(2)}}{\tau} \tag{4.15}$$

From equations (4.13) and (4.15), the mass and momentum equations are obtained

$$\frac{\partial \rho}{\partial t} + \nabla \cdot \rho u = 0 \tag{4.16}$$

$$\frac{\partial \rho u}{\partial t} + \nabla \cdot \Pi = 0 \tag{4.17}$$

which are accurate to second order in $\epsilon$ for equation (4.2). The momentum flux tensor $\Pi$ has the form:

$$\Pi_{\alpha\beta} = \sum_i \left(e_i\right)_\alpha \left(e_i\right)_\beta \left[f_i^{eq} + \left(1 - \frac{1}{2\tau}\right) f_i^1\right] \tag{4.18}$$

$(e_i)_\alpha$ is the component of the velocity vector $e_i$ in the $\alpha$-coordinate direction.
To specify the detailed form of $\Pi_{\alpha\beta}$, the lattice structure and the corresponding equilibrium distribution have to be specified. For simplicity, we use the square lattice commonly known as the $D2Q9$ model as it is two dimensional and involves 9 velocity vectors defined by

$$\begin{aligned} e_i &= (0,0) && i = 0 \\ e_i &= \left(cos\left(\pi/2\left(i-1\right)\right), sin\left(\pi/2\left(i-1\right)\right)\right) && i = 1,3,5,7 \\ e_i &= \sqrt{2}\left(cos\left(\pi/2\left(i-1\right)\right) + \pi/4, sin\left(\pi/2\left(i-1\right)\right) + \pi/4\right) && i = 2,4,6,8 \end{aligned}$$

The general form of the equilibrium distribution function can be written up to $O(u^2)$ as:

$$f_i^{eq} = \rho\left[a + be_i \cdot u + c\left(e_i \cdot u\right)^2 + du^2\right] \tag{4.19}$$

where a, b and c are lattice constants. Using the constraints in equation (4.5), the coefficients in equation (4.20) can be obtained analytically [91]:

$$f_i^{eq} = \rho w_i \left[1 + 3e_i \cdot u + \frac{9}{2}\left(e_i \cdot u\right)^2 - \frac{3}{2}u^2\right] \tag{4.20}$$

with $w_0 = 4/9$, $w_1 = w_3 = w_5 = w_7 = 1/9$ and $w_2 = w_4 = w_6 = w_8 = 1/36$. Inserting these formula in equation (4.18) gives:

$$\begin{aligned} \Pi^{(0)}_{\alpha\beta} &= \sum_i (e_i)_\alpha (e_i)_\beta f_i^{eq} = p\delta_{\alpha\beta} + \rho u_\alpha u_\beta \\ \Pi^{(1)}_{\alpha\beta} &= \left(1 - \frac{1}{2\tau}\right) \sum_i (e_i)_\alpha (e_i)_\beta f_i^1 = \nu \left(\nabla_\alpha(\rho u_\beta) + \nabla_\beta(\rho u_\alpha)\right) \end{aligned} \tag{4.21}$$

where $p = \rho/3$ is the pressure, which gives a constant sound speed $c = 1/\sqrt{3}$, and $\nu = (2\tau - 1)/6$ is the kinematic viscosity.

The resulting momentum equation is

$$\rho \left(\frac{\partial u_\alpha}{\partial t} + \nabla_\beta \cdot u_\alpha u_\beta\right) = -\nabla_\alpha p + \nu \nabla_\beta \cdot (\nabla_\alpha \rho u_\beta + \nabla_\beta \rho u_\alpha) \tag{4.22}$$

which is exactly the same as the Navier-Stokes equations if the density variation $\delta\rho$ is small enough [91].

It is important to understand that the LBM does not deliver a complete reproduction of molecular dynamics, as this would be much too expensive. Instead, it successfully constructs a simplified mesoscopic description that still contains the essential micro-physics to achieve desired macroscopic behaviour.

### 4.2.3 Wall boundary conditions treatment

For the LBM, the discrete distribution functions on the boundary have to be used with care to reflect the macroscopic boundary conditions of the fluid. PowerFLOW makes use of the standard Lattice-Boltzmann bounce back boundary condition for no-slip or the specular reflection for free-slip condition which are generalized through a volumetric formulation [102] near the wall for arbitrarily oriented surface elements (surfels) within the Cartesian volume elements (voxels).

The first step in the set-up of the boundary conditions for a lattice Boltzmann simulation consists in the definition of the character of each lattice node. Fluid nodes are those grid points on which the flow collision operator is fully applied. All other grid points are referred to as solid nodes. The relevant ones among them are the boundary nodes. These are the ones where flows impinge on at least one solid node which may belong to a movable particle or to the system wall. Collisions of fluid particles

with solid objects at the boundary nodes can be grouped into three types of obstacle situations [103], namely collision with static solid objects, collision with moving wall and collision with moving particles. Such contact situations are in lattice Boltzmann simulations usually implemented by applying so-called no-slip, or stick, boundary conditions in the case when a solid obstacle imposes friction (figure 4.4). This is achieved by implementing a bounce-back algorithm: during streaming, the component of the distribution function that would propagate into the solid node is bounced back and ends up back at the fluid node, but pointing in the opposite direction. This means that incoming particle portions are reflected back towards the nodes they came from. This rule produces stick boundary conditions at roughly one-half the distance along the link vector joining the solid and fluid nodes, ensuring that the velocity of the fluid in contact with the solid equals the velocity of the latter. In the case when the zero velocity plane must be located exactly inside the boundary layer, i.e. on the corresponding boundary layer nodes rather than being shifted from the location of the boundary nodes halfway into the fluid, one can use suited interpolation algorithms [103]. An alternative to the introduction of a nodal bounce-back interpolation rule is to place the boundary nodes midway between solid and fluid nodes. Frictional slip or the limiting case of free-slip boundary conditions may be appropriate for smooth boundaries with small or negligible friction exerted on the flow.

### 4.2.4 Initial conditions

Initial conditions are defined by starting from an equilibrium distribution. This means that the flow density is equal to a constant everywhere on the grid, since $\rho(x,t) = m\sum_{i=0}^{M} f_i^{eq}(x,t)$ and the speed is equal to 0 at each node in the system before the first translation and collision operations. The initiation of flows can than be induced by imposing constant velocity boundary conditions at the fluid inlet for instance in conjunction with periodic boundary conditions. Such settings can typically approximate the experimental practice of constant flow rates. Periodic boundary conditions are particularly useful for modelling bulk systems because they tend to minimize finite-size edge effects. Another important initial standard condition is the assumption

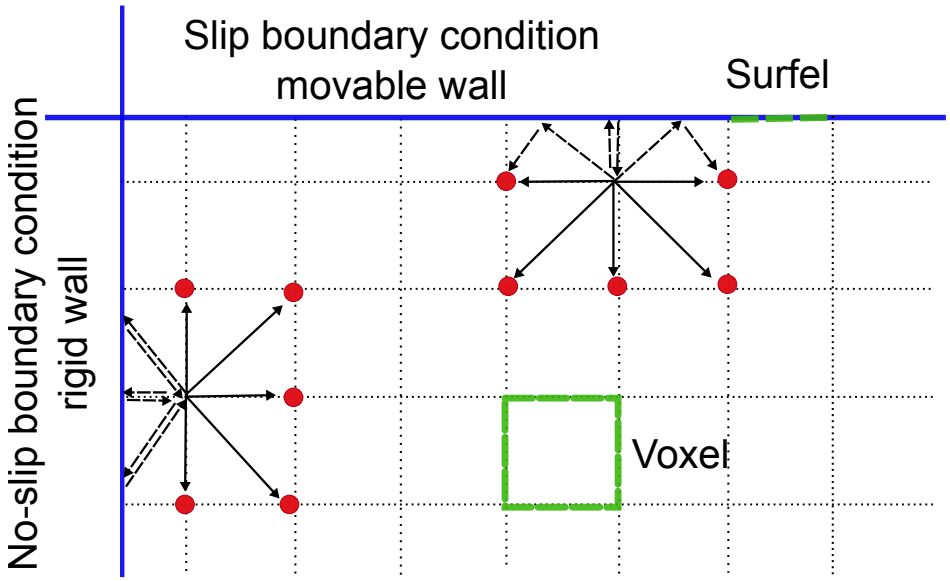


Figure 4.4: Implementation of the bounce-back boundary conditions [99]

of constant pressure.

### 4.2.5 Turbulence modelling

The lattice Boltzmann flow simulation is equivalent to a Direct Numerical Simulation (DNS) of the flow. For high Reynolds number flows, turbulence modelling is incorporated into the lattice Boltzmann model by replacing the relaxation time, which is related to the thermodynamic chaotic motion of fluid particles, by a turbulent relaxation time that models the effect of turbulent chaotic motion on the statistics of fluid particle collisions. The turbulent kinetic energy and the turbulent dissipation are obtained by solving a variant of the RNG $k-\epsilon$ model [104]:

$$\rho\frac{Dk}{Dt} = \frac{\partial}{\partial x_j}\left[\left(\frac{\rho\nu_0}{\sigma_{k_0}} + \frac{\rho\nu_T}{\sigma_{k_T}}\right)\frac{\partial k}{\partial x_j}\right] + \tau_{ij}S_{ij} - \rho\epsilon \tag{4.23a}$$

$$\rho\frac{D\epsilon}{Dt} = \frac{\partial}{\partial x_j}\left[\left(\frac{\rho\nu_0}{\sigma_{\epsilon_0}} + \frac{\rho\nu_T}{\sigma_{\epsilon_T}}\right)\right] + C_{\epsilon_1}\frac{\epsilon}{k}\tau_{ij}S_{ij} - \left[C_{\epsilon_2} + C_\mu\frac{\tilde{\eta}^3\left(1-\tilde{\eta}/\eta_0\right)}{1+\beta\tilde{\eta}^3}\right]\rho\frac{\epsilon^2}{k} \tag{4.23b}$$

The parameter $\nu_T = C_\mu k^2/\epsilon$ is the eddy viscosity in the RNG formulation. All dimensionless coefficients are the same as in the original models. The above equations are solved on the same lattice using a modified Lax-Wendroff explicit time marching finite difference scheme.

In order to model the turbulent fluctuations, the LBM is extended by replacing its molecular relaxation time scale with an effective turbulent relaxation time scale derived from a systematic renormalization group (RNG) procedure [97] as

$$\tau_{eff} = \tau + C_{\mu}\frac{k^2/\epsilon}{T\left(1+\tilde{\eta}^2\right)^{1/2}} \tag{4.24}$$

where $\tilde{\eta}$ is a combination of a local strain parameter ($\eta = k\left|S\right|/\epsilon$), local vorticity parameter ($\eta_{\omega} = k\left|\Omega\right|/\epsilon$), and local helicity parameters. This swirl correction for the local relaxation time, detects the occurrence of large-scale three-dimensional turbulent structures and reduces the influence of the turbulence model on the simulated flow accordingly. The swirl model together with the inherently unsteady nature of the lattice Boltzmann equation adequately reproduces the large scale turbulent vortices. This represents a key factor in predicting LES similar solutions on coarse grids using an unsteady turbulence model, a methodology referred to as Very Large Eddy Simulation (VLES). This LBE-VLES based description of turbulent fluctuation carries flow history and upstream information, and contains high order terms to account for the non-linearity of the Reynolds stress [93].

To reduce the resolution requirements near the wall for high Reynolds number flows, an extended wall function is used to model the boundary layer on the solid surfaces. The wall function model is an extension of the standard formulation and includes the effects of favorable and adverse pressure gradients on the outer boundary-layer variables [97].

## 4.3 Geometry and operating conditions

In order to investigate the effects of sawtooth trailing edge and leading edge serrations on the noise produced by the propellers, different serrated blades geometries will be tested and compared to the reference blade. Note that in this study, the serrations are not inserted onto a classical rounded leading edge or on the trailing edge but are obtained by variation of the spanwise distribution of chord and thickness which results in the existence of streamwise streaks into both sides of the blade. In the next sections, serrated trailing edge geometries will be referred as $STE$ and serrated leading edge geometries as $SLE$.

### 4.3.1 Baseline blade geometry

The baseline configuration has been released by Marinus et al. [105] It features a four-bladed single rotation propeller with a diameter $D$ of $1m$, composed of NACA 16 airfoils along the entire span (figures 4.5(a), 4.5(b)). The blade angle at 75%-radius $\beta_{ref}$ is of 40° with respect to the plane of rotation (figure 4.5(c)).

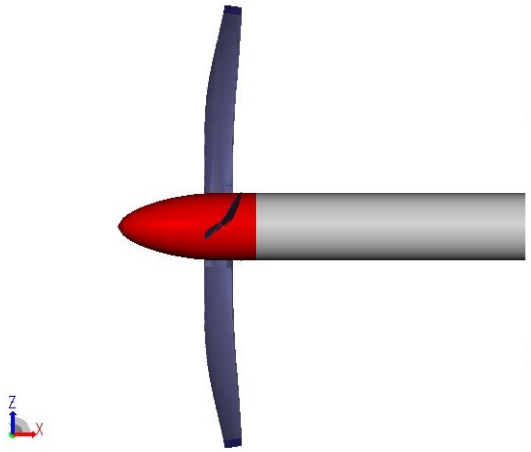


(a) Baseline propeller.

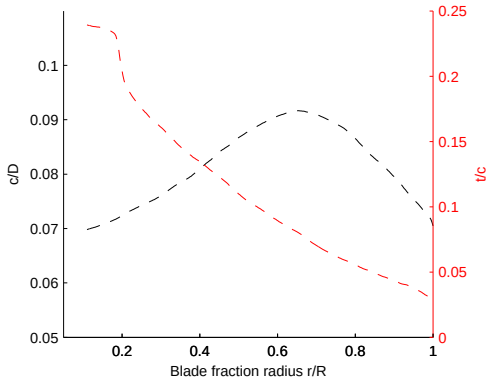


(b) Chord $c(r)/D$ and Thickness $t(r)/c$ distribution.

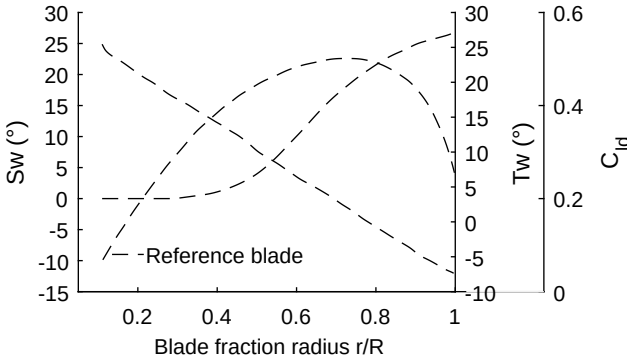


(c) Sweep $S_w(r)$, twist $T_w(r)$ and design lift coefficient $C_{ld}(r)$ distribution.

Figure 4.5: Geometry of the baseline propeller.

### 4.3.2 Serrated blades geometries

The sawtooth serrated geometries (figures 4.6(a), 4.6(b)) are derived from the baseline blade, they conserve the same geometric characteristics of the baseline blade except for the chord and thickness distributions as shown in figures 4.7(a) and 4.7(b) for the

trailing edge serrated blades $STE1$ and $STE4$, while the sawtooth edge extends from 20% to 100% radius for all serrated geometries. The parameters of serrations in terms of root-to-tip distance $2h$ and wavelength $\lambda$ reported to the boundary layer thickness $\delta$ for the serrated trailing edge geometries and to the turbulence length scale $L_t$ for the serrated leading edge geometries are shown in table 4.1.

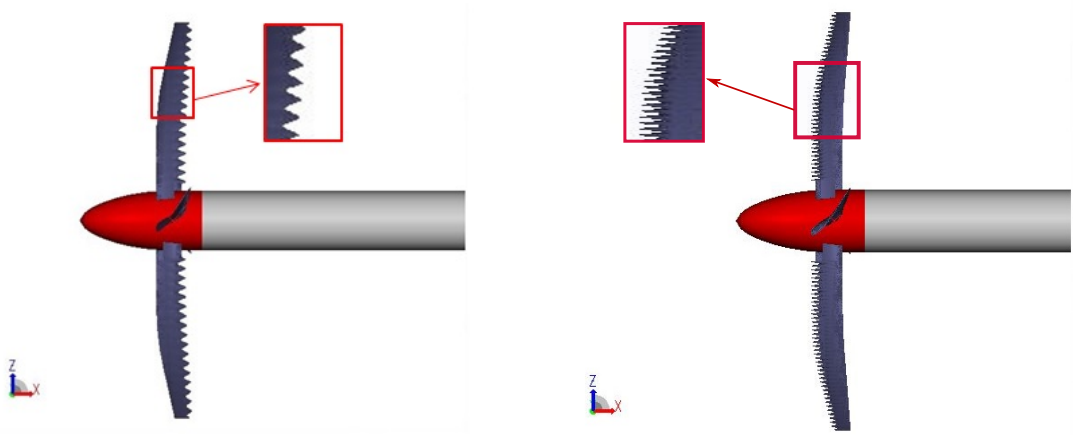

(a) Serrated blade $STE1$. (b) Serrated blade $SLE7$.

Figure 4.6: Geometry of the serrated blades $STE1$ and $SLE7$.

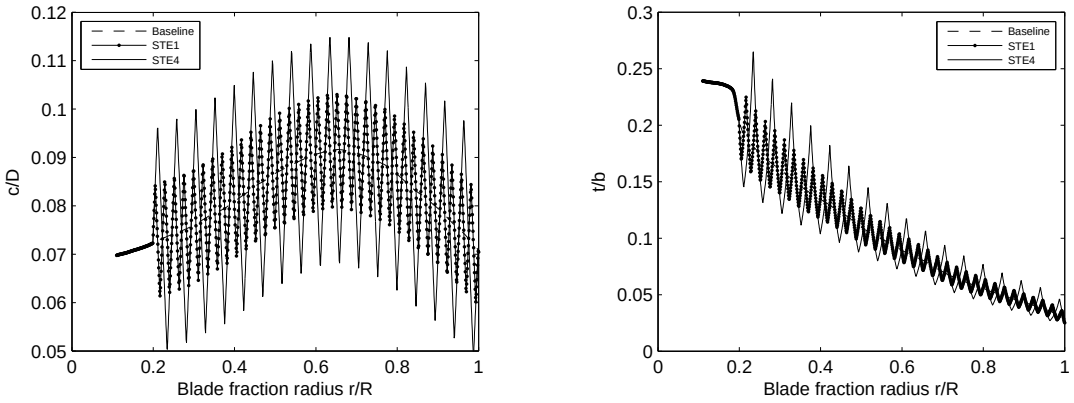


(a) Chord $c(r)/D$ distribution. (b) Thickness $t(r)/c$ distribution.

Figure 4.7: Chord and thickness distributions for the serrated blades $STE1$ and $STE4$.

| STE blade | $h/\delta$ | $h/\lambda$ |
|---|---|---|
| STE1 | 2 | 1 |
| STE2 | 2 | 4 |
| STE3 | 4 | 4 |
| STE4 | 4 | 1 |
| STE5 | 5 | 4 |
| STE6 | 4 | 5 |
| STE6 | 4 | 5 |

| SLE blade | $h/L_t$ | $h/\lambda$ |
|---|---|---|
| SLE3 | 10 | 2.5 |
| SLE4 | 10 | 5 |
| SLE5 | 12 | 5 |
| SLE6 | 15 | 5 |
| SLE7 | 12 | 2.5 |
| SLE9 | 25 | 5 |
| SLE12 | 12 | 7 |

Table 4.1: Serrations parameters

### 4.3.3 Operating conditions

The propellers operate at an altitude of 1000m in cruise conditions (zero incidence) with a flight Mach number $M_\infty$ of 0.2. The Reynolds number based on the chord of the reference blade at 75% radius is of $8.28e5$ and the reference advance ratio $J = v/(n.D)$ is of 1.4 with $n$ the rotational velocity in rps. This corresponds to a subsonic tip Mach number of 0.49 obtained from the vector sum of the rotational and flight velocities. In these conditions, the reference blade develops a power coefficient $C_P = 0.31$ for a thrust coefficient $C_T = 0.17$ and an efficiency of 76%.

## 4.4 Numerical set up

### 4.4.1 Mics positions

The Sound Pressure Level (SPL) is computed at various receiver locations. 19 receivers were distributed around the propeller at different angular locations on a circular array of 3 tip radii, with a constant angular spacing of $5^o$ from $5^o$ to $175^o$ as shown in figure 4.8. These receivers are limited to a maximum frequency of 11kHz. The human ear perceives frequencies between 20Hz and 20kHz. However, frequencies between 1 and 4kHz are best perceived. From this frequency, the more it increases, the less the perception is easy [106]. The simulations of this study are therefore limited to 11kHz. The pressure is measured at the location of the receivers for the duration of the simulation (including during the use of the source file) at a frequency of $1.844e3$ kHz.

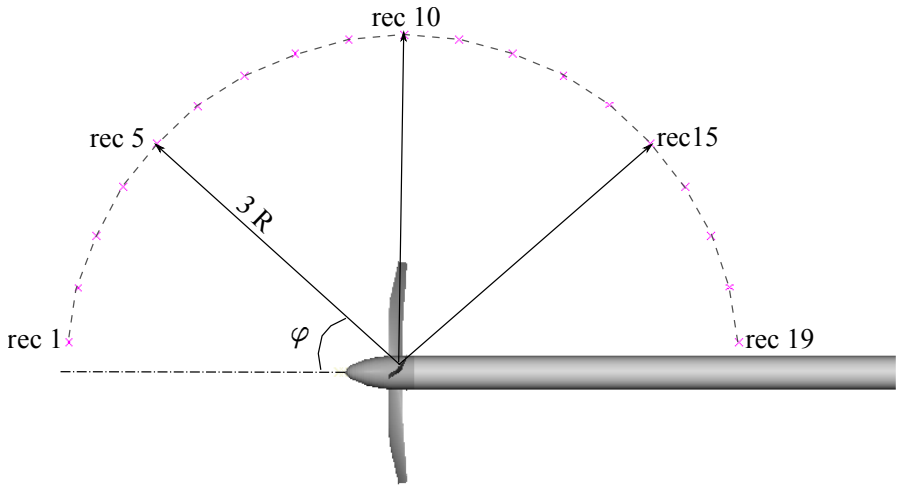


Figure 4.8: Location of acoustic receivers.

### 4.4.2 Space and time discretization

The cubic Cartesian lattice (voxel) for the LBM-solver [100] is generated automatically from the CAD file of the propeller which is enclosed in a sliding-mesh region. As visible in figure 4.9 the blades (blue) and the rotating spinner (red) are enclosed by a volume that define the rotating mesh region (green) and the spinner is extended with a solid non rotating cylinder (grey). All these surfaces have a no-slip wall-boundary condition. A series of variable resolution or Voxel Refinement (VR) regions are set around the propeller from the coarsest one (VR0) to the finest one (VR13) (figure 4.9) with the mesh resolution varying by a factor 2 between two adjacent VR levels. VR10 corresponds to the rotating mesh region (green). VR levels from 12 onwards are generated by offsetting the geometry parts in the wall normal direction. Details about the VR regions are summarized in table 4.2. Solid surfaces are covered automatically by intersecting the mesh with the wall geometry using planar surface elements (surfels). In the standard configuration (here after referred to as v8), for aeroacoustic calculations, 600 voxels are generated along the blade chord at 75% radius for VR13 as shown in figure 4.10, for the baseline and the serrated blades, resulting in about 114 million voxels in total. All unsteady simulations are conducted for three full rotations of the propeller after a transient period of three rotations to yield satisfactory periodic

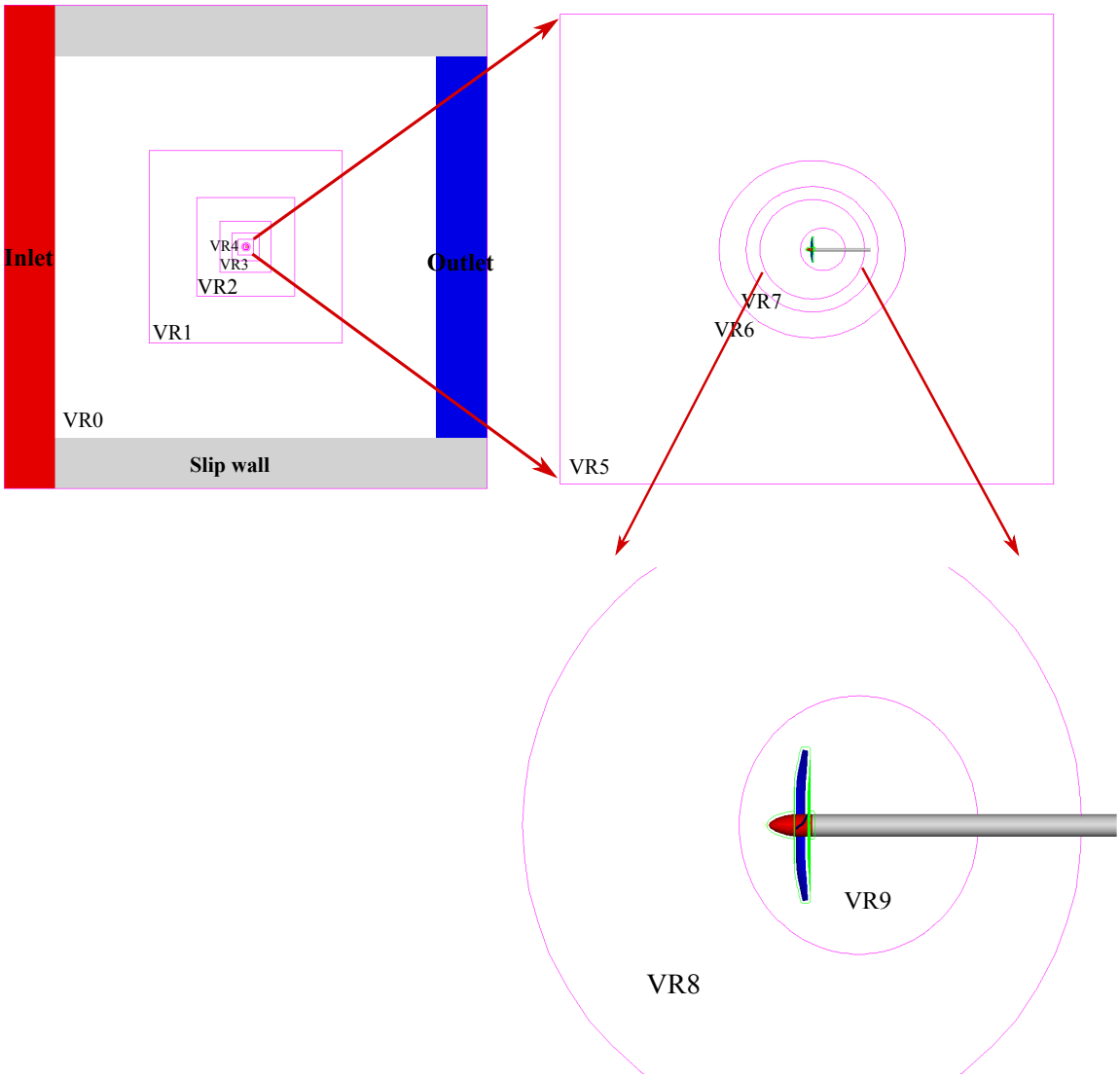


Figure 4.9: Voxel Refinement (VR) regions and boundary conditions.

| VR | voxel size (m) | shape of the bounding domain |
|---|---|---|
| 0 | 4.95 | cube |
| 1 | 2.475 | cube |
| 2 | 1.237 | cube |
| 3 | 0.619 | cube |
| 4 | 0.309 | cube |
| 5 | 0.155 | cube |
| 6 | 0.077 | sphere |
| 7 | 0.039 | sphere |
| 8 | 0.019 | sphere |
| 9 | 9.67e-3 | sphere |
| 10 | 4.83e-3 | around the blade (rotating) |
| 11 | 2.42e-3 | around the blade (rotating) |
| 12 | 1.21e-3 | offset (spinner and blade- rotating) |
| 13 | 0.604e-3 | offset (blade- rotating) |

Table 4.2: Properties of VR levels.

convergence. The computations are started using the seeding technique from previous converged cases. With the maximum acoustic frequency of interest set at 11kHz and taking an anti-aliasing factor of 2 into account and at least 7 time steps per wave, this results in $6.5e6$ time steps of the order of $5.5e-7$s each.

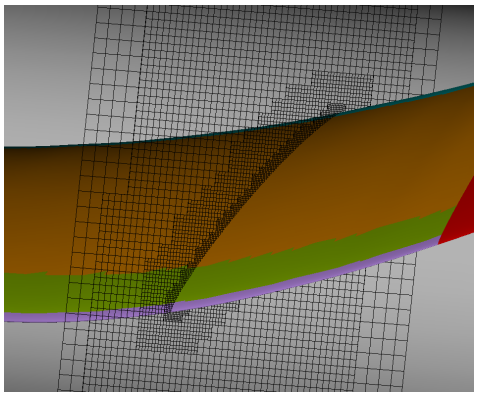

(a) Baseline blade.

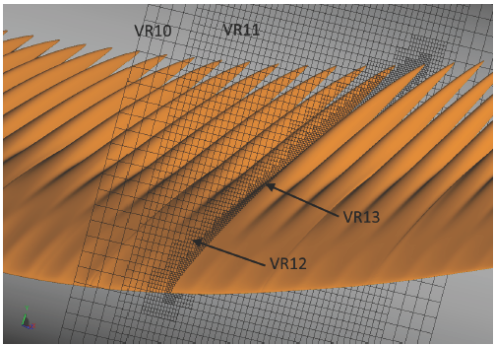


(b) STE blade.

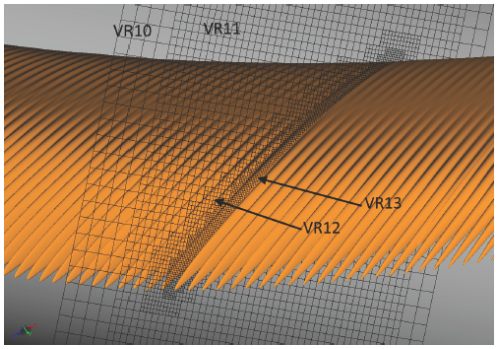


(c) SLE blade.

Figure 4.10: Highest refinement in VR12 and VR13 (blocks of 2x2 voxels shown for clarity).

## 4.5 Influence of model parameters on the prediction of aerodynamic performance

The influence of several model parameters is first assessed according to table 4.3 in order to yield adequate grid independence. The aerodynamic coefficients for propellers are calculated as follows, where $T$ is the net propeller thrust and $P$ is the net power. The thrust coefficient

$$C_T = \frac{T}{\rho n^2 D^4} \tag{4.25}$$

The power coefficient is given by

$$C_P = \frac{P}{\rho n^3 D^5} \tag{4.26}$$

The resulting efficiency is

$$\eta = \frac{JC_T}{C_P} \tag{4.27}$$

As can be seen from table 4.3, the v8 setting offers an accurate solution for a less expensive cost since the computational time scales roughly with the number of voxels whenever the number of CPUs is kept constant. From a purely aerodynamic point of view, this setting satisfies the requirement on accuracy of the solutions as can be seen from table 4.4 which shows the results from a grid dependency study performed according to Celik et al. [107]. The computed order of the extrapolation polynomial is of 3.3 for $C_T$ and 0.3 for $C_P$.

| Version | | VR region of the blade | #vovels per chord | frequency of interest | $C_T$ | $C_P$ | $\eta$ |
|---|---|---|---|---|---|---|---|
| v2 | | 12 | 450 | 11kHz | 0.158 | 0.289 | 0.76 |
| v3 | | 13 | 450 | 11kHz | 0.163 | 0.309 | 0.74 |
| v4 | raw | 13 | 450 | 12kHz | 0.162 | 0.309 | 0.73 |
| v5 | | 12 | 600 | 11kHz | 0.160 | 0.299 | 0.75 |
| v6 | fine | 13 | 700 | 11kHz | 0.167 | 0.314 | 0.74 |
| v8 | standard | 13 | 600 | 11kHz | 0.166 | 0.313 | 0.74 |

Table 4.3: Influence of model parameters on the aerodynamic performance (STE4 at $J$ =1.4).

| $\phi$ | $C_T$ | $C_P$ |
|---|---|---|
| $\phi^{\text{ext}}_{\text{fine,std}}$ | 0.1685 | 0.3155 |
| $e^{\text{a}}_{\text{fine,std}}$ | 0.60% | 0.32% |
| $e^{\text{ext}}_{\text{fine,std}}$ | 0.89% | 0.47% |
| $GCI_{\text{fine}}$ | 1.12% | 0.59% |

Table 4.4: Grid convergence study with the refinement factors $r_{\text{fine,std}} = 1.17$ and $r_{\text{raw,std}} = 1.33$.

Using the v8 set up, different geometries were analyzed under constant flow conditions. The aerodynamic performance of the trailing edge serrated blades $STE1$ and $STE4$ and the leading edge serrated blades $SLE4$ and $SLE7$ in comparison with the baseline blade is shown in figure 4.11. It appears that although differences exist in terms of net thrust and power, the penalty from trailing edge serrations is limited in terms of efficiency. Leading edge serrations lead to a larger efficiency.

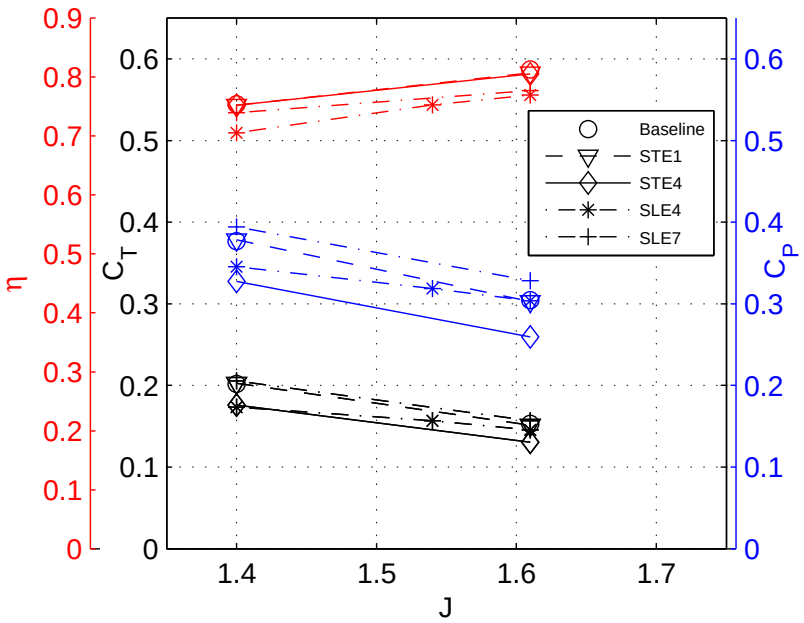


Figure 4.11: Aerodynamic performance in terms of $C_T$, $C_P$ and $\eta$ from different individuals.

## 4.6 Aeroacoustic prediction capability

PowerFLOW simulations produce a variety of information about the flow, such as pressure, velocity, and temperature as functions of space and time. Due to the transient nature of the method, in addition to the time-averaged results, fluctuating quantities are available, potentially at each fluid and surface location in the simulation at each time step. PowerACOUSTICS is used to post-process this time-dependent data, using time-series analysis such as statistics and Fourier transform-based frequency analysis [108]. All the LBM spectra presented in this study were post-processed using PowerACOUSTICS.

Using the v8 set-up, the noise spectrum emitted by the reference blade is compared in figure 4.12 with the predicted spectrum from Amiet's analytical model combined with the mean pressure gradient model for the wall pressure statistics for the calculation of the trailing edge noise. It can be seen that the analytical method captures the trend and estimates with a good precision the SPL levels of the noise at high frequencies. The discrepancies at low frequencies are due to the presence of the tonal components carried out by the LBM spectrum. This figure illustrates the potential of both methods

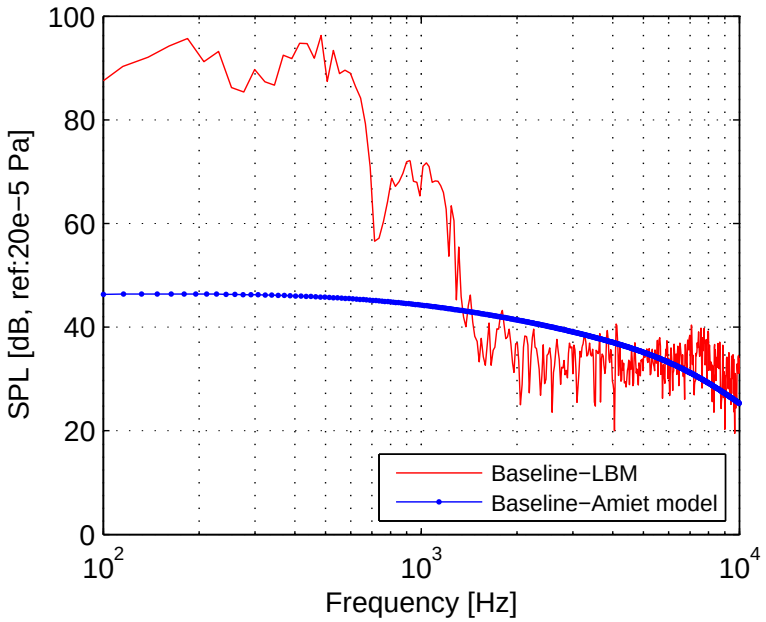


Figure 4.12: Power Spectral Density for different geometries compared to the results from the analytical model.

to predict the noise emitted by the blades. The analytical method requirement in resources and computational time are at least one order of magnitude less than for the LBM approach. Nevertheless, one should be careful not to miss some of the physics going on around the blades.

# *Chapter 5*
# *Propellers trailing edge noise reduction using sawtooth serrations*

# Chapter 5
# Propellers trailing edge noise reduction using sawtooth serrations

The main aim of this chapter is to investigate the trailing edge noise reduction performance of sawtooth serrations applied to propellers. First, the analytical formulation used to predict trailing edge noise from serrated airfoils is detailed and validated against experimental data. Then the formulation is extended to predict trailing edge noise from rotating blades. The model is assessed by comparison to the LBM simulations results and the effect of the order approximation and the number of segments on the predicted spectra is studied. A parametric study is conducted with different serrations parameters to define the geometry which yields the maximum noise reduction. Furthermore, the effect of flow conditions on the predicted spectra is investigated along with the directivity patterns. A further objective of this chapter is to investigate the physical mechanisms responsible for the change in the trailing edge noise radiation due to the introduction of sawtooth serrations.

The results presented in this chapter have been the subject of a publication in the International Journal of Aeroacoustics [109] and presented in AIAA aeroacoustics conferences [110, 111].

## 5.1 Analytical formulation

In this section, the detailed derivation of the self noise model for single airfoil with sawtooth serrated trailing edge developed by Lyu et al. [37] is presented.

### 5.1.1 The mathematical model

Consider an airfoil with trailing edge serrations as an infinitesimally flat plate as shown in figure 5.1, with an averaged chord length c and a span L. $x^{'}$ and $y^{'}$ are the streamwise and spanwise coordinates, respectively. The direction perpendicular to the airfoil plane is parallel to $z^{'}$ axis. The observer is located at $(x_1, x_2, x_3)$.

The sawtooth serrations are characterised by the root-to-tip length of $2h$, the periodic

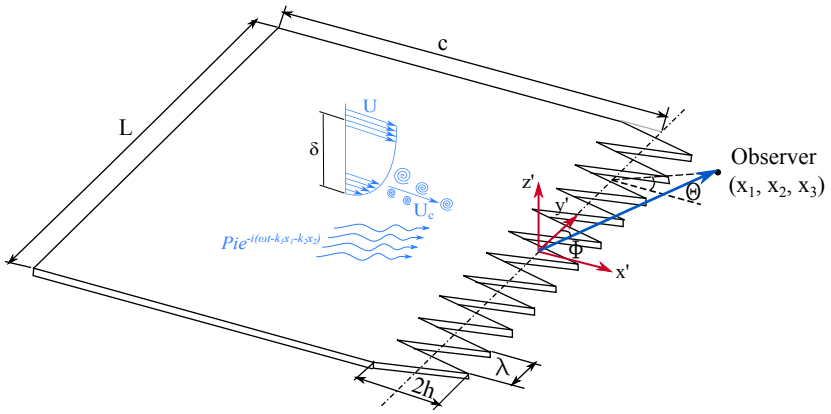


Figure 5.1: Sketch of a flat plate with serrated trailing edge and the related local coordinates system.

wavelength $\lambda$ and the sharpness $\sigma = 4h/\lambda$. The profile function $H(y^{'})$ describes the serrated edges. The origin of the coordinates is chosen in such a way that $H(y^{'})$ is an oscillatory function of zero mean and that $H(y^{'}) = 0$ in the absence of serrations.
Consider the surface pressure beneath the turbulent boundary layer that would exist when the trailing edge is absent. After implementing a Fourier transformation, the surface pressure can be expressed as an integral of different wall pressure gust components. The specific component of frequency $\omega$ takes the form of

$$p_i = P_i e^{-i(\omega t - k_1 x^{'} - k_2 y^{'})} \tag{5.1}$$

where $P_i$ is the magnitude of the incident wall pressure gust and $k_1$ and $k_2$ are the wavenumbers in the chordwise and spanwise directions, respectively.
Amiet [49] stated that the presence of a half rigid surface leads to a scattered pressure distribution. The total pressure may be decomposed into an incident part $p_i$ and a scattered part $p$. The boundary conditions at $z^{'} = 0$ read

$$\begin{cases} \frac{\partial p}{\partial z^{'}} = 0 & x^{'} < H(y^{'}) \\ p = -P_i e^{-i(\omega t - k_1 x^{'} - k_2 y^{'})} & x^{'} \geq H(y^{'}) \end{cases} \tag{5.2}$$

In the airfoil fixed frame $(x^{'}, y^{'}, z^{'})$, the wave equation governing the scattered ressure field $p$ remains the same as in the straight edge cases

$$\nabla^2 p - \frac{1}{c^2}\left(\frac{\partial}{\partial t} + U\frac{\partial}{\partial x^{'}}\right)^2 p = 0 \tag{5.3}$$

with the assumption of harmonic perturbation $p = P(x^{'}, y^{'}, z^{'})e^{-i\omega t}$, the above equation reduces to

$$\beta^2 \frac{\partial^2 P}{\partial x'^2} + \frac{\partial^2 P}{\partial y'^2} + \frac{\partial^2 P}{\partial z'^2} + 2ikM\frac{\partial P}{\partial x'} + k^2 P = 0 \tag{5.4}$$

where $k = \omega/c$, $\beta^2 = 1 - M^2$ and $M = U/c$.

A coordinate transformation is then applied where: $x = x^{'} - H(y^{'})$, $y = y^{'}$, $z = z^{'}$ and leads to the following differential equation:

$$\left(\beta^2 + H^{'2}(y)\right)\frac{\partial^2 P}{\partial x^2} + \frac{\partial^2 P}{\partial y^2} + \frac{\partial^2 P}{\partial z^2} - 2H^{'}(y)\frac{\partial^2 P}{\partial x \partial y} + \left(2iMk - H^{''}(y)\right)\frac{\partial P}{\partial x} + k^2 P = 0 \tag{5.5}$$

where $H^{'}(y)$ and $H^{''}(y)$ denote the first and second derivatives of $H(y)$. The boundary conditions now read

$$\begin{cases} P(x,y,0) = -P_i e^{i(k_1 x + k_2 y)} e^{ik_1 H(y)} & x \geq 0 \\ \partial P(x,y,0)/\partial z = 0 & x < 0 \end{cases} \tag{5.6}$$

The Fourier expansion is used to solve equation (5.5) as it will be explained in the following section.

### 5.1.2 Fourier expansion

The scattered pressure can be expanded using Fourier series in terms of the new coordinates $(x, y, z)$ as

$$P(x,y,z) = \sum_{-\infty}^{\infty} P_n(x,z)\, e^{ik_{2n}y} \tag{5.7}$$

where $k_{2n} = k_2 + 2n\pi/\lambda$

Substituting the above expression into equation (5.5) yields

$$\left(\beta^2 + H^{'2}(y)\right)\frac{\partial^2}{\partial x^2} + \frac{\partial^2}{\partial y^2} + \frac{\partial^2}{\partial z^2} - 2H^{'}(y)\frac{\partial^2}{\partial x \partial y} + \left(2iMk - H^{''}(y)\right)\frac{\partial}{\partial x} + k^2 \times \left\{\sum_{-\infty}^{\infty} P_n(x,z)\, e^{ik_{2n}y}\right\} = 0 \tag{5.8}$$

Multiplying equation (5.8) by $e^{-ik_{2n'}y}$, then integrating it over $y$ from $-\lambda/2$ to $\lambda/2$ gives

$$\begin{aligned}&\left\{\beta^2\frac{\partial^2}{\partial x^2}+\frac{\partial^2}{\partial z^2}+2iMk\frac{\partial}{\partial x}+\left(k^2-k_{2n'}^2\right)\right\}P_{n'}\\&+\frac{1}{\lambda}\int_{-\lambda/2}^{\lambda/2}\sum_{-\infty}^{\infty}\left\{H'^2\frac{\partial^2}{\partial x^2}-\left(H''+2ik_{2n}H'\right)\frac{\partial}{\partial x}\right\}P_n e^{i2(n-n')\pi/\lambda y}dy=0\end{aligned}\tag{5.9}$$

Now, to obtain an equation which involves only one mode $n'$, $H'(y)$ and $H''(y)$ must be constants within the entire wavelength so that the summation over different modes can be dropped. Consider the sawtooth presented in figure 5.2 with the joint points denoted as $(\lambda_0,\epsilon_0)$, $(\lambda_1,\epsilon_1)$ and $(\lambda_2,\epsilon_2)$.

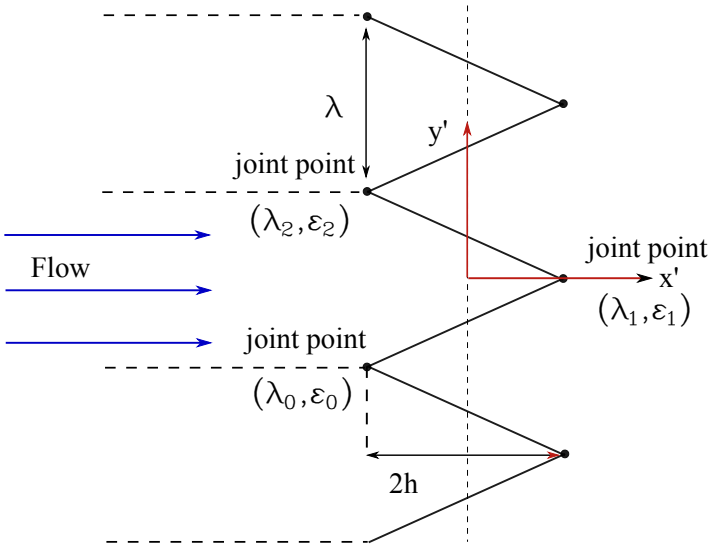


Figure 5.2: The schematic of trailing edge serration profile.

The serration profile function $H(y)$ can therefore be defined as

$$H(y)=\begin{cases}\sigma_0\left(y-\lambda_0-m\lambda\right)+\epsilon_0 & \lambda_0+m\lambda<y\leq\lambda_1+m\lambda\\ \sigma_1\left(y-\lambda_1-m\lambda\right)+\epsilon_1 & \lambda_1+m\lambda<y\leq\lambda_2+m\lambda\end{cases}\tag{5.10}$$

where $\sigma_j=(\epsilon_{j+1}-\epsilon_j)/(\lambda_{j+1}-\lambda_j)$, $j=0,1$ and $m=0,\pm1,\pm2,....$ For this sawtooth profile, $H'(y)$ is not continuous and $H''(y)$ is thus singular at the joint points. The conventional generalized function $\delta(x)$ is used to describe the singularities at these points:

$$H^{'}(y) = \begin{cases} \sigma_0 & \lambda_0 + m\lambda < y \leq \lambda_1 + m\lambda \\ \sigma_1 & \lambda_1 + m\lambda < y \leq \lambda_2 + m\lambda \end{cases} \tag{5.11}$$

$$H^{''}(y) = \sum_{-\infty}^{\infty} (-1)^(m+1) 2\sigma\delta\left(x - m\lambda/2\right) \tag{5.12}$$

Substituting the serration profile function and its derivatives into equation 5.9, and making use of the fact that $\int_{-\infty}^{\infty} f(x)\delta(x-\tau)dx = f(\tau)$ gives

$$\begin{aligned} &\left\{ \left(\beta^2 + \sigma^2\right) \frac{\partial^2}{\partial x^2} + \frac{\partial^2}{\partial z^2} + 2iMk\frac{\partial}{\partial x} + \left(k^2 - k_{2n'}^2\right) \right\} P_{n'} \\ &= \frac{-4\sigma}{\lambda} \sum_{n-n^{'}=odd} \left(1 - \frac{k_2\lambda + 2n\pi}{(n-n^{'})\pi}\right) \frac{\partial P_n}{\partial x} \end{aligned} \tag{5.13}$$

The set of differential equations can be written as

$$DP = AP + B\frac{\partial P}{\partial x} \tag{5.14}$$

where $D$ is a linear operator expressed as $D = \left\{ \left(\beta^2 + \sigma^2\right) \frac{\partial^2}{\partial x^2} + \frac{\partial^2}{\partial z^2} + 2iMk\frac{\partial}{\partial x} \right\}$ and $P = \left(...P_{-n'}(x,z), P_{-n'+1}(x,z), ...P_{n'-1}(x,z), P_{n'}(x,z)\right)^T$. $T$ denotes the transpose of the matrix. Matrices $A$ and $B$ denote the coefficient matrices of $P$ and $\partial P/\partial x$. $A_{ml}$ and $B_{ml}$ represent the entry corresponding to mode $m$ in row and $l$ in column of matrix $A$ and $B$

$$\begin{aligned} A_{ml} &= \left(k_{2m}^2 - k^2\right)\delta_{ml} \\ B_{ml} &= \begin{cases} \frac{4\sigma}{\lambda}\frac{m+l+k_2\lambda/\pi}{l-m} & m-l = odd \\ 0 & m-l = even \end{cases} \end{aligned} \tag{5.15}$$

where $\delta_{ml}$ is the Kronecker delta.

Substituting the profile geometry into the boundary conditions (equation 5.6) and performing the same Fourier expansions gives

$$\begin{cases} P_n(x,0) = -P_i a_n e^{ik_1 x} & x > 0 \\ \partial P_n(x,0)/\partial z = 0 & x < 0 \end{cases} \tag{5.16}$$

where $a_n$ is defined as

$$a_n = \frac{1}{\lambda}\int_{-\lambda/2}^{\lambda/2} e^{ik_1 H(y)} e^{-i2n\pi/\lambda y} dy \tag{5.17}$$

### 5.1.3 Acoustic formulation

Following the same procedure used by Amiet [13, 112], the scattered surface pressure is solved then the far field sound is evaluated.

To obtain the scattered surface pressure, equation 5.14 together with the boundary conditions in equation 5.16 are solved using an iteration process [37]. The exact solutions $P$ can be expressed as

$$P(x,0) = N(x) + C^{(1)}(x) + C^{(2)}(x) + C^{(3)}(x) + ... \tag{5.18}$$

where $N$ denotes the non-coupled part, while the the coupled parts are denoted by $C^{(i)}$ $(i = 1, 2, 3...)$. The entries of $N$ and $C^{(1)}$ of the first iteration corresponding to mode $n^{'}$ are expressed by

$$N_{n'}(x) = P_i e^{ik_1 x} a_{n'} \left((1-i)E(-\mu_{n'}x) - 1\right) \tag{5.19}$$

$$\begin{aligned} C^1_{n'}(x) =& P_i e^{ik_1 x}(1-i) \sum_{m=-\infty}^{\infty} \alpha_{n'm} a_m \Bigg( ik_1 \left(E(-\mu_{n'}x) - E(-\mu_m x)\right) \\ & - \sqrt{\frac{\mu_m}{-2\pi x}} \left(e^{-i\mu_{n'}x} - e^{-i\mu_m x}\right) \Bigg) \end{aligned} \tag{5.20}$$

where $\alpha_{ml}$ is a coefficient matrix expressed by

$$\alpha_{ml} = \begin{cases} \frac{B_{ml}}{k_{2m}^2 - k_{2l}^2} = \frac{-4h}{\pi^2(m-l)^2} & m-l = odd \\ 0 & m-l = even \end{cases} \tag{5.21}$$

and

$$\begin{aligned} \mu_{n'} &= K_{n'} + k_1 + \frac{kM}{\beta^2 + \sigma^2} \\ K_{n'} &= \sqrt{k^2(1+\sigma^2) - k_{2n'}^2(\beta^2+\sigma^2)}/(\beta^2+\sigma^2) \end{aligned} \tag{5.22}$$

The scattered surface pressure is finally obtained by summing the modal pressure over all different modes and transforming back to the physical coordinate system.

$$P(x^{'}, y^{'}, 0) = \sum_{n'=-\infty}^{\infty} \left[N_{n'} + C^{(1)}_{n'} + C^{(2)}_{n'} + ...\right] \left(x^{'} - H(y^{'}), 0\right) e^{ik_{2n'}y^{'}} \tag{5.23}$$

where the functions $N_{n'}$ and $C_{n'}^{(1)}$ are defined in equations (5.19, 5.20), $C_{n'}^{(2)}$ is the result of the second order iteration and the terms in the parenthesis are the arguments for the $N_{n'}$ and $C_{n'}^{(i)}$ functions.

Having obtained the scattered surface pressure, the far field sound induced by the scattered surface pressure is found using the surface pressure integral. It is expressed as

$$p_f\left(x,\omega,k_2\right)=\left(\frac{-i\omega x_3 c}{4\pi c_0 S_0^2}\right)\lambda\frac{sin\left(\left(N+1/2\right)\lambda\left(k_2-kx_2/S_0\right)\right)}{sin\left(\lambda/2\left(k_2-kx_2/S_0\right)\right)}I(\omega,k_1,k_2)P_i \tag{5.24}$$

where $S_0=\sqrt{x_1^2+\beta^2\left(x_2^2+x_3^2\right)}$ is the corrected distance for convection effects and $(2N+1)$ is the number of sawtooth on the trailing edge.

$I$ is the far field sound gust response function defined as:

$$\begin{aligned}I(\omega,k_1,k_2)=&(1-i)\frac{1}{\lambda c}\left(\sum_{n'=-\infty}^{+\infty}\left(\Theta_{n'}^{(0)}+\Theta_{n'}^{(1)}+\Theta_{n'}^{(2)}+...\right)\right)\\&\times e^{-ik(Mx_1-S_0)/\beta^2}e^{ik(Mx_1/S_0)h/\beta^2}\end{aligned} \tag{5.25}$$

The radiation functions of order 0 and 1 are defined as:

$$\Theta_{n'}^{(0)}=a_{n'}Q_{n'n'} \tag{5.26a}$$

$$\Theta_{n'}^{(1)}=\sum_{m=-\infty}^{+\infty}\alpha_{n'm}ik_1a_m\left(Q_{n'n'}-Q_{n'm}\right)-\alpha_{n'm}\sqrt{\mu_m}a_m\left(S_{n'n'}-S_{n'm}\right) \tag{5.26b}$$

The functions $Q_{nm}$ and $S_{nm}$ are given by

$$\begin{aligned}Q_{nm}=&\sum_{j=0}^{1}\frac{1}{\kappa_{nj}}\left\{\frac{1}{\mu_A}\left(e^{i\kappa_{nj}\lambda_{j+1}}\Gamma(c+\epsilon_{j+1};\mu_m,\mu_A)-e^{i\kappa_{nj}\lambda_j}\Gamma(c+\epsilon_j;\mu_m,\mu_A)\right)\right.\\&\left.-\frac{1}{\mu_{Bnj}}e^{i\kappa_{nj}(\lambda_j-(c+\epsilon_j)/\sigma_j)}\left(\Gamma(c+\epsilon_{j+1};\mu_m,\mu_{Bnj})-\Gamma(c+\epsilon_j;\mu_m,\mu_{Bnj})\right)\right\}\end{aligned} \tag{5.27}$$

$$\begin{aligned}S_{nm}=&\sum_{j=0}^{1}\frac{1}{i\kappa_{nj}}\left\{\frac{1}{\sqrt{\eta_{Am}}}\left(e^{i\kappa_{nj}\lambda_{j+1}}E(\eta_{Am}(c+\epsilon_{j+1}))-e^{i\kappa_{nj}\lambda_j}E(\eta_{Am}(c+\epsilon_j))\right)\right.\\&\left.-\frac{1}{\sqrt{\eta_{Bmj}}}e^{i\kappa_{nj}(\lambda_j-(c+\epsilon_j)/\sigma_j)}\left(E(\eta_{Bmj}(c+\epsilon_{j+1}))-E(\eta_{Bmj}(c+\epsilon_j))\right)\right\}\end{aligned} \tag{5.28}$$

where

$$\Gamma(x;\mu,\nu) = e^{-i\nu x}E(\mu x) - \sqrt{\frac{\mu}{\mu-\nu}}E((\mu-\nu)x) + \frac{1}{1-i}(1-e^{i\nu x}) \tag{5.29}$$

$$\begin{aligned}
\eta_{Am} &= K_m + kM/(\beta^2+\sigma^2) - k(M - x_1/S_0)/\beta^2 \\
\eta_{Bmj} &= K_m + kM/(\beta^2+\sigma^2) + (k_{2n} - kx_2/S_0)/\sigma_j \\
\mu_A &= k_1 + k(M - x_1/S_0)/\beta^2 \\
\mu_{Bnj} &= k_1 - (k_{2n} - kx_2/S_0)/\sigma_j \\
\kappa_{nj} &= k_{2n} - kx_2/S_0 + k(M - x_1/S_0)\sigma_j/\beta^2
\end{aligned} \tag{5.30}$$

**Far field sound spectrum density**

Rather than working with deterministic pressure, it is necessary to work with the statistical power spectrum that can be measured experimentally. The hypothetical surface pressure of frequency $\omega$ beneath a turbulent boundary layer that would exist when the trailing edge is absent can be expressed as

$$P_{int}\left(\omega, x^{'}, y^{'}\right) = \int_{-\infty}^{\infty} P_i(\omega, k_2) e^{i(k_1 x^{'} + k_2 y^{'})} dk_2 \tag{5.31}$$

The far field sound pressure induced by this wall pressure is

$$p_f\left(x, \omega, k_2\right) = \left(\frac{-i\omega x_3 c}{4\pi c_0 S_0^2}\right) \int_{-\infty}^{\infty} \lambda \frac{sin\left(\left(N + 1/2\right)\lambda\left(k_2 - kx_2/S_0\right)\right)}{sin\left(\lambda/2\left(k_2 - kx_2/S_0\right)\right)} I(\omega, k_1, k_2) P_i(\omega, k_2) dk_2 \tag{5.32}$$

According to Amiet [49], the PSD of the far field sound is given by

$$S_{pp} = \lim_{T\to\infty}\left(\frac{\pi}{T}\left\langle p_f(x,\omega) p_f^*(x,\omega)\right\rangle\right) \tag{5.33}$$

where $p_f^*(x,\omega)$ denotes the conjugate of $p_f(x,\omega)$, and $2T$ is the time length used to obtain $p_f(x,\omega)$ by performing Fourier transformation. Substituting equation 5.32 into equation 5.33 yields

$$S_{pp}(x,\omega) = \left(\frac{\omega x_3 c}{4\pi c_0 S_0^2}\right)^2 \int_{-\infty}^{\infty} \lambda^2 \left(\frac{sin\left(\left(N + 1/2\right)\lambda\left(k_2 - kx_2/S_0\right)\right)}{sin\left(\lambda/2\left(k_2 - kx_2/S_0\right)\right)}\right) |I|^2 \Pi(\omega, k_2) dk_2 \tag{5.34}$$

where $\Pi(\omega, k_2)$ is the wavenumber spectral density [22] of the surface pressure beneath the turbulent boundary layer on the airfoil surface. A simplification of equation 5.34 is possible by assuming a very large span. The PSD of the far field sound in the plane $y^{'} = 0$ is then given by

$$S_{pp}\left(\vec{x}, \omega\right) = \left(\frac{\omega x_3 c}{4\pi c_0 S_0^2}\right)^2 2\pi L \sum_{m=-\infty}^{+\infty} |I(\omega, k_1, 2m\pi/\lambda)|^2 \Pi(\omega, 2m\pi/\lambda) \tag{5.35}$$

The wavenumber spectral density of the surface pressure is approximated [31, 37] by:

$$\Pi(\omega, k_2) \approx \frac{4C_m \rho_0^2 \upsilon_*^4 (\omega/U_c)^2 \delta^4}{U_c \left(\left((\omega/U_c)^2 + k_2^2\right)\delta^2 + \chi^2\right)^2} \tag{5.36}$$

where $\rho_0$ and $\delta$ are the fluid density and the boundary layer thickness respectively, $C_m \approx 0.1553$, $\chi \approx 1.33$ and $\upsilon_* = 0.03U$.

The convection velocity is taken as $U_c = \alpha U$ with $U$ the flow velocity and $\alpha = 0.7$.

**Model's validation**

In this section, the serrated trailing edge noise model for airfoils is validated using measured radiated noise for different serrated geometries.

The influence of the presence of serrations and the flow velocity on the emitted noise levels is assessed in figure 5.3 (shown in third-octave bands). Experiments [113] were conducted on a NACA0018 airfoil of chord $20cm$ and span of $40cm$ in flow velocity of $30 - 40m/s$. Results are presented for sawtooth serration of amplitude $2h = 4cm$ ($2h \approx 4\delta$) and wavelength $\lambda = h$.

These results are compared to those of figure 30 from [113] to assess the sensitivity of the model to flow velocity. The present receivers array differs from [113] in that it is composed of 64 microphones forming a Cartesian grid. No beamforming treatment is applied on the present results. The boundary layer thickness is obtained by:

$$\delta/c \;=\; 0.382\, Re_c^{1/5} \tag{5.37}$$

Despite the simplifications, the results in figure 5.3 show that the dependance of noise to the inflow velocity is captured even though it overpredicts the reduction. Moreover, it can be seen that the present model is able to predict the noise from a serrated trailing

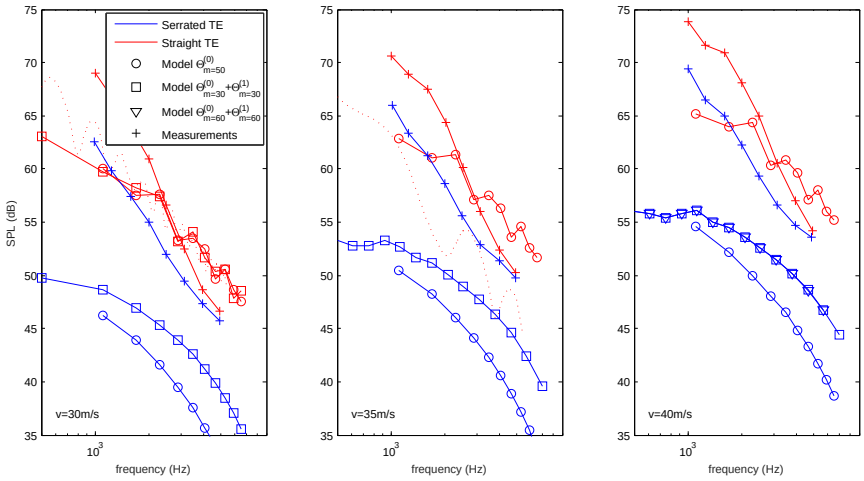


Figure 5.3: Influence of the presence of serrations and the flow velocity on the radiated noise of the airfoil. comparison with measurements [113].('...' Schlinker and Amiet straight-edge model)

edge as well as that of straight geometry. In the later case, the model is used in the limit of no serrations (i.e. $\lim h/c \to 0$ and $\lim \lambda/h \to \infty$).

The convergence rate of the $0^{th}$ and $1^{st}$ order solutions (see equations 5.26a and 5.26b) is inspected by presenting the far field sound spectrum obtained for the two approximations. In practice, the sum over $m$ or $n^{'}$ in equations 5.25, 5.26a-5.26b, and 5.35 is truncated. Results presented in figure 5.3 show that the $0^{th}$ order solution with $m$ =50 underestimates the result by about 15dB. The $1^{st}$ order solution with $m$ =30 gives a better approximation when compared to measurements. Another test was conducted with $m$ =60 with no effect on the accuracy of the solution. When using the $1^{st}$ order solution, the model got computationally more expensive, scaling with $(2m+1)^3$ as found in [38]. Nevertheless, the $0^{th}$ order approximation is computationally relatively cheap and is able to capture the relative variations.

Figure 5.4 shows a comparison of the predicted noise spectra for the baseline and two serrated trailing edge geometries with experimental data [38]. The airfoil used in the experiments has a chord length of $0.6m$ and a span of $1.82m$. Two sawtooth shaped trailing edge geometries were tested, with the wavelength to amplitude ratio of $\lambda/h = 1$. The serrations are denoted SER10 and SER15 according to [38] with amplitudes of $2h = 10cm$ and $2h = 15cm$ respectively.

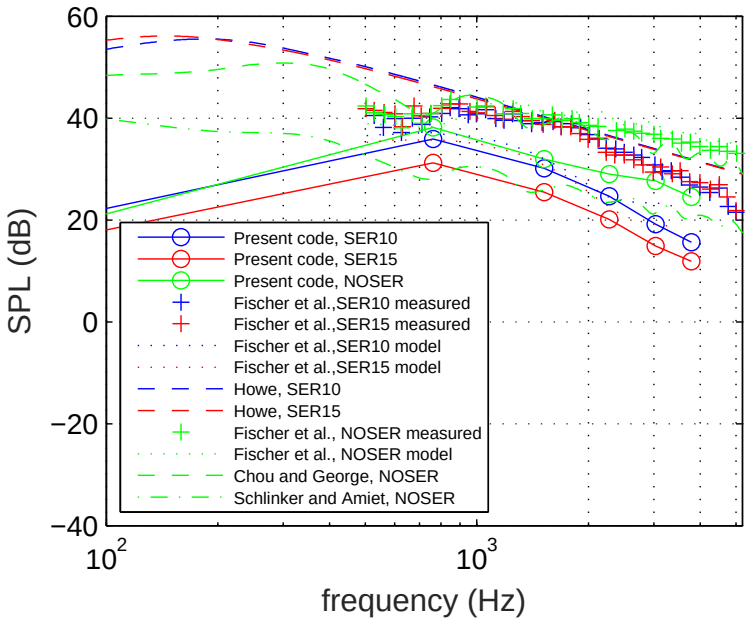


Figure 5.4: Far field spectra calculated with the present model for the baseline and two serrated geometries of the airfoil. Comparison with other analytical models and measurements [38]

The results are obtained using the $0^{th}$ order solution. The present model, used in the limit of no serrations, predicts with a better agreement the solution of the baseline configuration compared to Amiet's model. For the serrated geometries, the model underestimates the measurements, but the frequency dependence is predicted correctly; moreover, the SER10 is found to be louder than SER15 which is confirmed by the measurements. Consequently, this model can be used in the search for optimal serration geometry.

## 5.2 Extension of the single airfoil model to rotating blades

The same approach used to extend the analytical models for single airfoils to rotating blades, explained in section (2.7), is applied to predict the noise spectra emitted by the propellers with serrated trailing edge presented in this section. The far field noise PSD for all propellers is calculated by averaging over all possible angular locations of the blade segments (figure 5.5) and by weighting with the Doppler factor (see section

2.7.1):

$$S_{pp}^{\Psi}(\vec{X},\omega) = \frac{B}{2\pi}\int_0^{2\pi}\left(\frac{\omega_e(\Psi)}{\omega}\right)^2 S_{pp}^{\Psi}(\vec{x},\omega_e)d\Psi \tag{5.38}$$

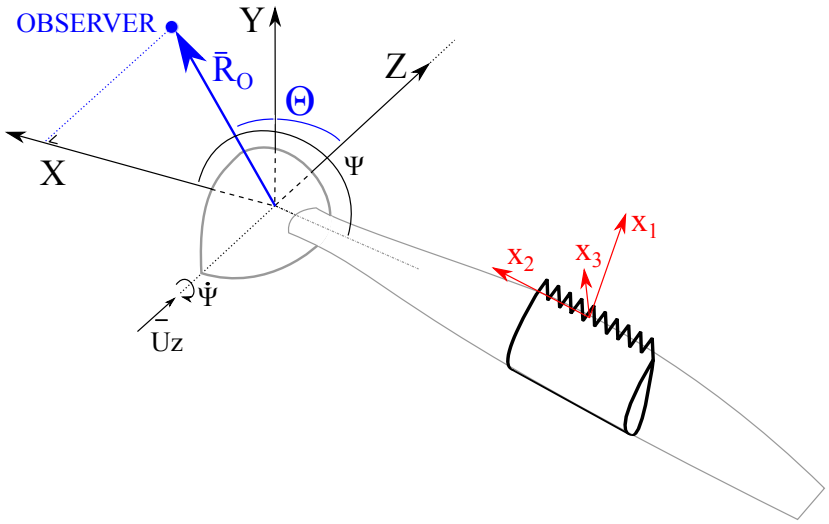


Figure 5.5: Global coordinates system used in the trailing edge serrated rotating blade model $(X, Y, Z)$ and the local relative coordinates system attached to the blade $(x_1, x_2, x_3)$.

## Post-processing boundary layer properties

Since the wall pressure spectrum in the vicinity of the trailing edge is the main input data for the calculation of the PSD expressed by equation 5.35. Steady RANS simulations of a single baseline blade passage were performed using finite volumes solver ANSYS Fluent. Details about the computational set up are presented in [114].

A proper post-processing from the RANS simulations, using a dedicated User Defined Function (UDF), was used to evaluate the boundary layer parameters needed for wall pressure models presented in section (2.5.1). The UDF allows to collect local velocities, pressure gradient $\partial P/\partial x$ and the wall shear stress $\tau_w$ at the desired chordwise and spanwise location. The data are then used to evaluate the following parameters:

– $\delta$: the boundary layer thickness defined as $U(\delta) = 0.99U_e$ where $U_e$ is the outer velocity;

– $\delta^*$: the displacement thickness defined as $\delta^* = \int_0^{\delta}(1 - U(y)/U_e)dy$;

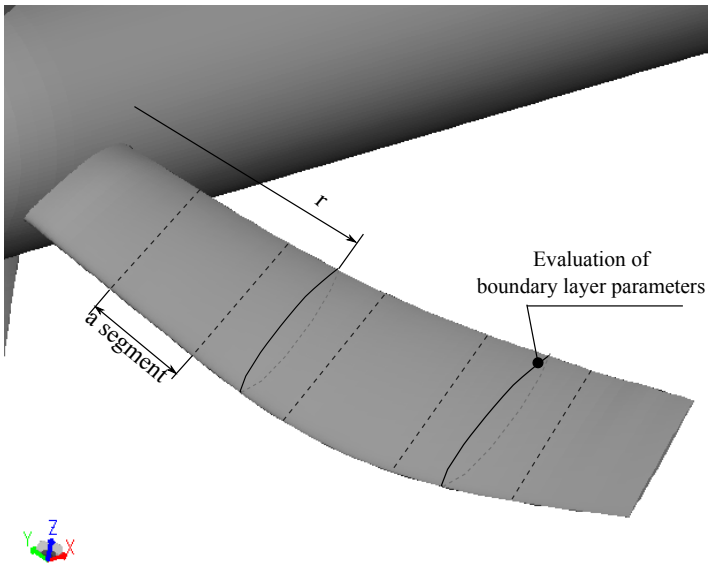


Figure 5.6: Propeller blade split into segments.

– $\theta$: the momentum thickness defined as $\theta = \int_0^\delta U(y)/U_e(1 - U(y)/U_e)dy$;
– $\beta_c$: Clauser's parameter [83] defined as $\beta_c = (\delta^*/\tau_w).(\partial P/\partial x)$;
– $\Pi$: the parameter of the law of the wake [84] defined as $1 + \Pi = (k\delta^* U_e)/(\delta u_\tau)$ where $u_\tau$ is the friction velocity;
– $R_T$: ratio of the outer to inner boundary layer time scale [115] defined as $R_T = (u_\tau \delta/\nu)\sqrt{C_f/2}$ where $\nu$ is the kinematic viscosity and $C_f$ is the skin friction coefficient.

The blade is split into six segments. On each segment the boundary layer properties are evaluated near the trailing edge on the suction side, at 99% of the chord length at the segment mid span as shown in figure 5.6. The data obtained with the post-processing described above are presented in table 5.1 and are used to supply the wall pressure spectra models combined to Amiet's model to predict the trailing edge noise of the baseline propeller in the next section.

## 5.3 Model's assessment

Figure 5.7 compares results for the reference propeller from a time-domain simulation with trailing edge noise results from the frequency-domain analytical models. The sim-

| $Radius(\%span)$ | 15 | 35 | 50 | 65 | 80 | 95 |
|---|---|---|---|---|---|---|
| $U_e(m/s)$ | 71.31 | 78.92 | 91.36 | 102.36 | 112.12 | 126.04 |
| $\delta(mm)$ | 3.98 | 2.91 | 2.26 | 1.96 | 1.97 | 1.99 |
| $\delta^*(mm)$ | 0.72 | 0.42 | 0.26 | 0.21 | 0.19 | 0.17 |
| $\tau_w(Pa)$ | 0.54 | 2.52 | 5.79 | 7.94 | 9.59 | 8.45 |
| $\beta_c$ | 44.38 | 5.38 | $-0.13$ | $-0.77$ | $-1.07$ | $-0.04$ |
| $\Pi$ | 6.03 | 1.86 | 0.78 | 0.56 | 0.39 | 0.50 |
| $R_T$ | 4.70 | 14.41 | 22.19 | 23.57 | 26.12 | 20.68 |

Table 5.1: Boundary layer parameters obtained from RANS simulations for the reference blade.

ulated Sound Pressure Levels (SPL) are obtained by performing the Fourier transform of the acoustic pressure collected by a receiver located at the distance of 3R from the propeller and at the angle $\theta = 90^o$ (receiver $N^o10$).

Amiet's model is combined with the wall pressure spectra models to predict the trailing edge noise radiated by the baseline propeller. The convection velocity is taken as $U_c = 0.7U$ and for the determination of the spanwise coherence length, the constant $b$ is 1.4. The results presented in figure 5.7 show that the model of Schlinker and Amiet predicts the overall tendency of the noise spectrum though it overpredicts the levels, while Goody's model fails to predict the tendency and underestimates the SPL levels. The mean gradient model predicts the correct tendency at high frequencies with a good approximation of the sound levels. Furthermore, the results show also that Lyu's model used with the $1^{st}$ order approximation and in the limit of no serration predicts with a good precision the tendency and the SPL levels of the simulated signal at high frequencies. Discrepancies are observed at low frequencies due to the contribution of the tonal component in the LBM spectrum.

Figure 5.8 presents the spectra obtained from the LBM simulation with those predicted by the serrated trailing edge noise analytical model. The analytical spectrum including the contribution of the trailing edge and the leading edge components emitted by the baseline propeller is presented using the analytical models of Lyu, with the first order approximation, in the limit of no serrations (i.e. $\lim h/c \to 0$ and $\lim \lambda/h \to \infty$). It can be seen that the contribution of the leading edge noise is barely felt at very high frequencies above $6000Hz$ as expected from low speed propellers. Note that the LBM

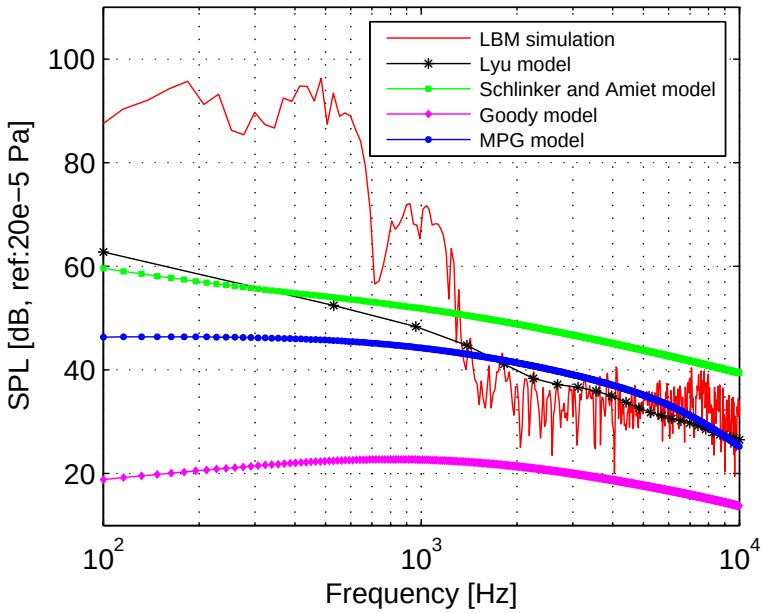


Figure 5.7: Comparison of the result of the time-domain simulation with the trailing edge noise from analytical models for the reference propeller.

spectrum contains the contribution of the leading edge and the trailing edge noise.

### 5.3.1 Effect of the order approximation

Since the analytical models for serrated edges can turn out to be computationally expensive for higher order solutions (Theta function in equation 5.26b) and large values of the truncation parameter m, the convergence rate of different order solutions are investigated. Figure 5.9 presents far field spectra using zero and first order approximations for the straight edge blade (figure 5.9(a)), and the serrated trailing edge blade $STE1$ (figure 5.9(b)).

For the serrated trailing edge model, it is clear that the $0^{th}$ order solution with $m = 30$ can provide an approximation of the solution but it underestimates the SPL levels at high frequencies compared to the LBM solution. The tests conducted with $m = 50$ show no considerable influence on the accuracy of the result. The $1^{st}$ order solution with $m = 30$ gives a better agreement with the LBM result. Further increasing in m doesn't affect the accuracy of the solution but results in a considerable increase in computational time since it scales with $(2m + 1)^3$ as pointed by Fischer et al. [38]

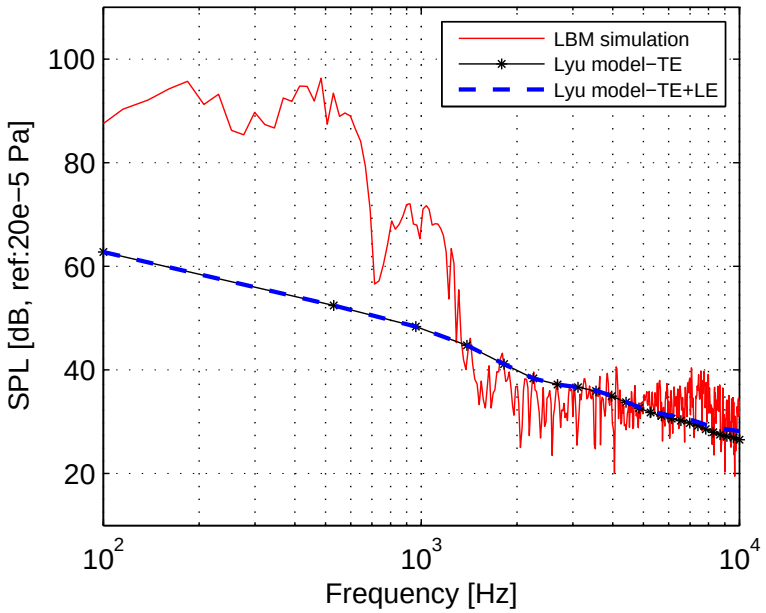


Figure 5.8: Comparison of the analytical result for the baseline blade with the time-domain LBM result.

Figure 5.10 compares the analytical predicted spectra ($1^{st}$ order solution with $m = 50$) for $STE3$ and $STE4$ serrated blades with the LBM results. It is clear that the tendency is well predicted with a good precision result at high frequencies.

### 5.3.2 Effect of segments number

The influence of the segments number on the far field noise is addressed in figure 5.11. Four configurations are tested with 3, 6, 9 and 12 segments on both the baseline and the serrated blade $STE1$. The spectra are calculated using the $1^{st}$ order approximation with $m = 50$.

The results show that the noise level increases and the gap between the spectra becomes smaller with increasing number of segments in all frequency range. The difference between the result calculated with 3 segments and the one calculated with 12 segments reaches the value of about $5dB$. The analytical model seems to converge for a large number of segments. Further investigations are needed to determine the limit of convergence with increasing the segments number.

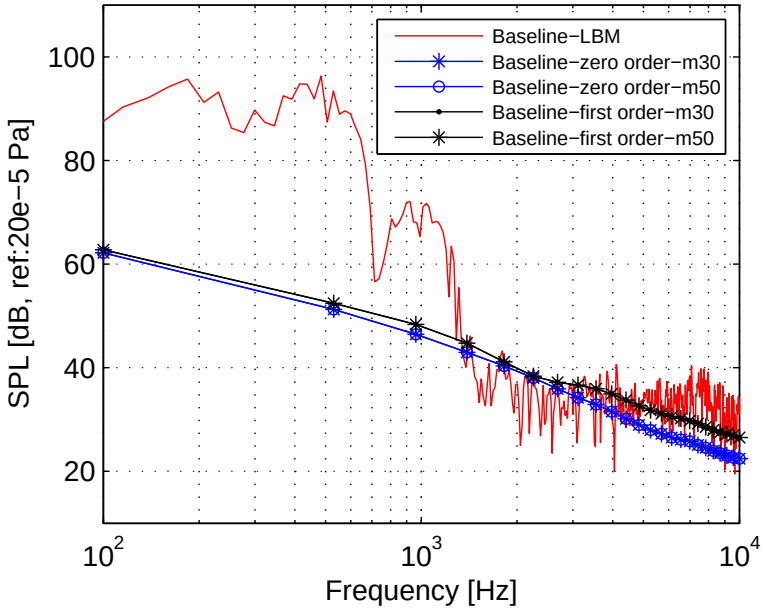


(a) Trailing edge noise of the baseline propeller.

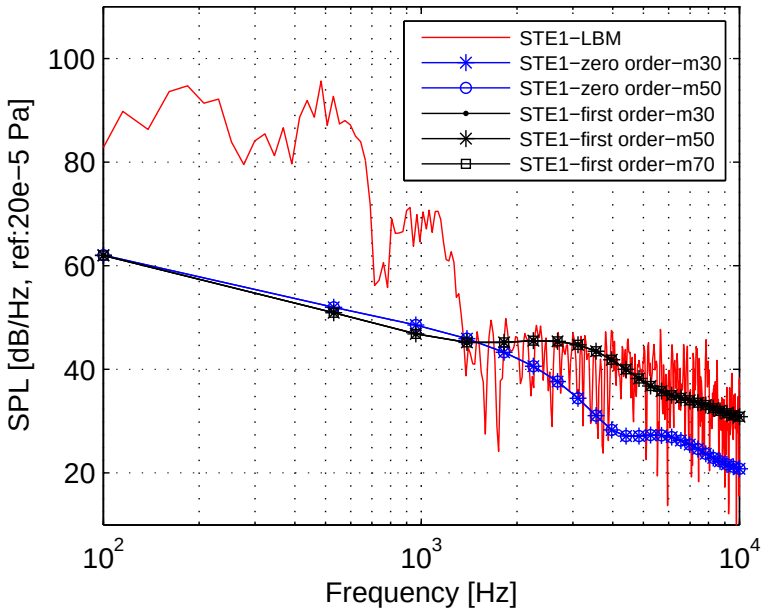


(b) Trailing edge noise of the serrated propeller STE1.

Figure 5.9: Effect of the order approximation on the analytical results.

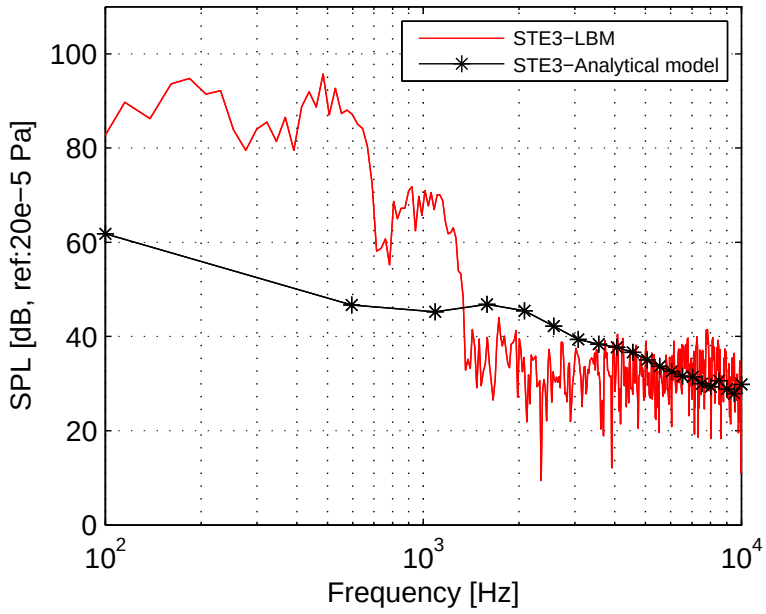


(a) $STE3$ propeller.

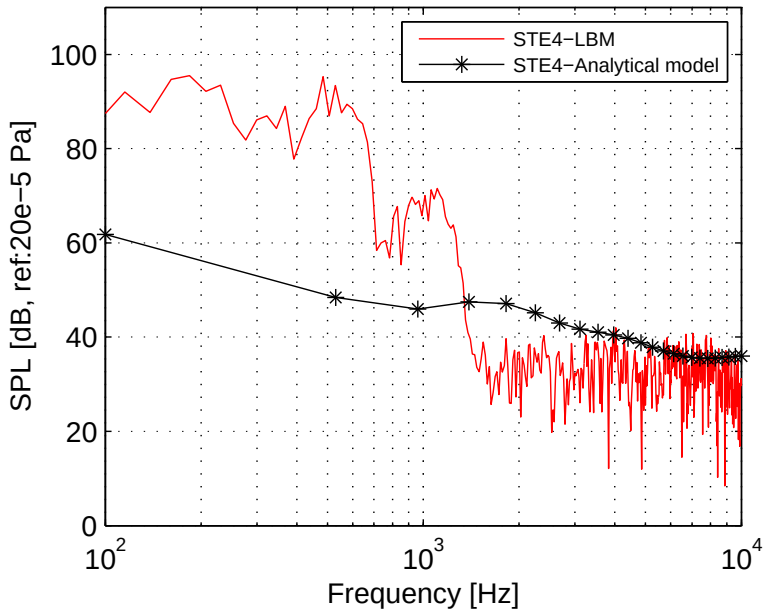


(b) $STE4$ propeller.

Figure 5.10: Comparison of the analytical result for the serrated blades $STE3$ and $STE4$ with the time-domain LBM results.

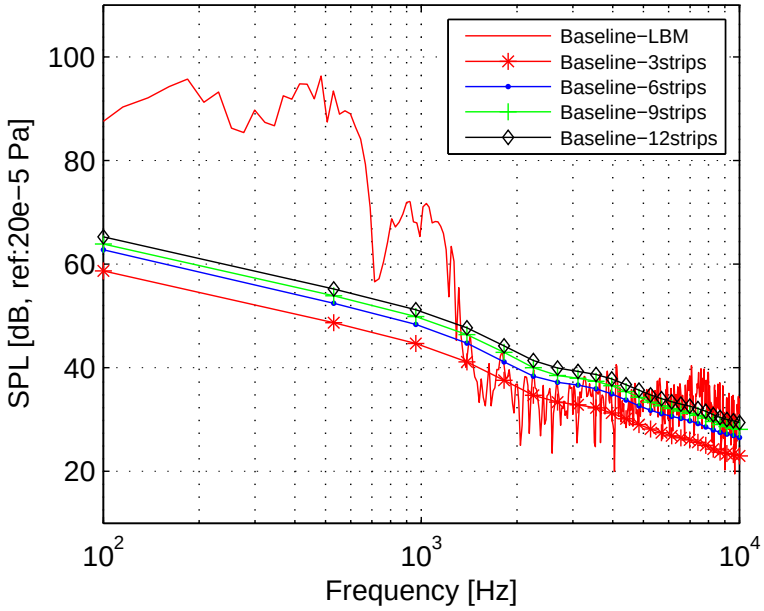


(a) Baseline propeller.

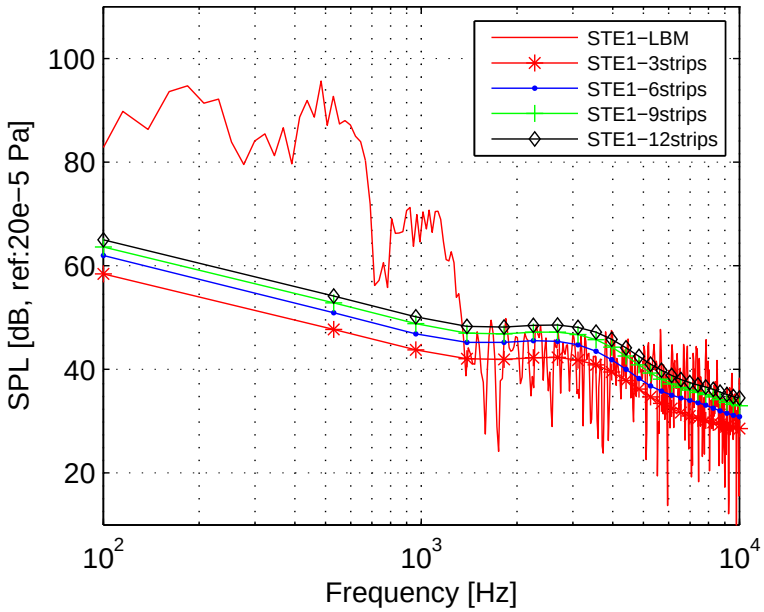


(b) Serrated propeller $STE1$.

Figure 5.11: Effect of the number of segments on the analytical results.

## 5.4 Variation with serrations parameters

Based on the previous results, a parametric numerical study was first conducted using the $0^{th}$ order approximation. Different trailing edge serrated geometries with different serration parameters were tested to select the geometries which provide noise reduction presented in table 4.1.

Figure 5.12 presents the noise spectra emitted by the selected trailing edge serrated blades in comparison with the baseline blade. The results show that all serrated blades produce a noise reduction at low to mid-frequency range ($f < 1200Hz$) however, a noise increase is observed at high frequencies. The noise reduction, associated to the destructive scattering interference effects [37], increases with the sharpness of the serrations i.e with $h/\lambda$ , as is the case with the serrated blades $STE3$, $STE5$ and $STE6$ which achieve the best performance.

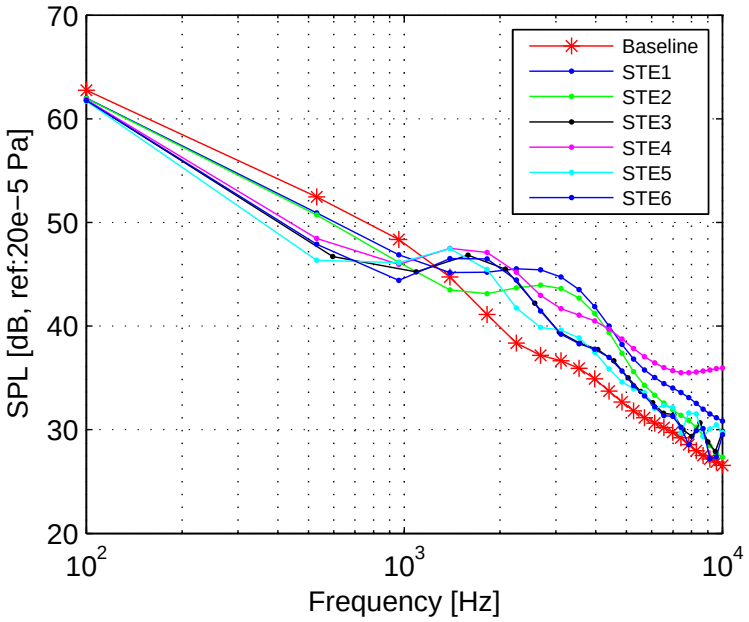


Figure 5.12: Results comparison between the predicted noise spectra of the serrated trailing edge blades and the baseline blade.

These observations are consistent with the experimental results obtained by Gruber et al. [35] for stationnary airfoils and with Oerlemans et al. [40] for a wind turbine, who pointed that the noise increase at high frequency is associated with the blade tips turbulence.

Figure 5.13 compares the spectra obtained by the time-domain LBM simulations for the serrated blades and the baseline blade. The results show that at low frequencies, the serrated blades $STE1$ and $STE3$ produce equivalent noise emission compared to the baseline, where $STE4$ achieves a noise reduction. At high frequencies, a noise increase is observed with all serrated blades with an important impact of $STE1$. In general, the spectra predicted by the analytical model show a good agreement with those predicted by the LBM simulations in terms of tendencies and SPL levels.

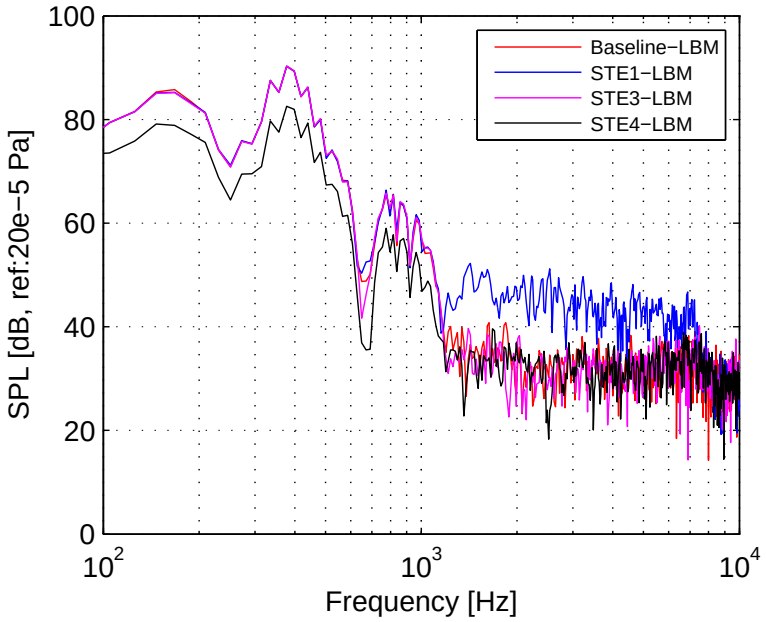


Figure 5.13: Simulated trailing edge noise spectra emitted by the serrated propellers compared to the baseline propeller.

## 5.5 Variation with advance ratio

In order to assess the influence of the presence of serrations with varying advance ratios on the emitted noise levels, tests were conducted with the baseline and $STE1$ blades for different advance ratios. The spectra are presented in figure 5.14.

It can be seen from the results that lower advance ratios, hence higher velocities on the blade, produce higher noise levels. For the advance ratio $J = 1.4$, for which the tip Mach number reaches 0.49, the spectrum presents the higher noise levels. The LBM results present also the same tendencies but with a slight difference in the SPL levels

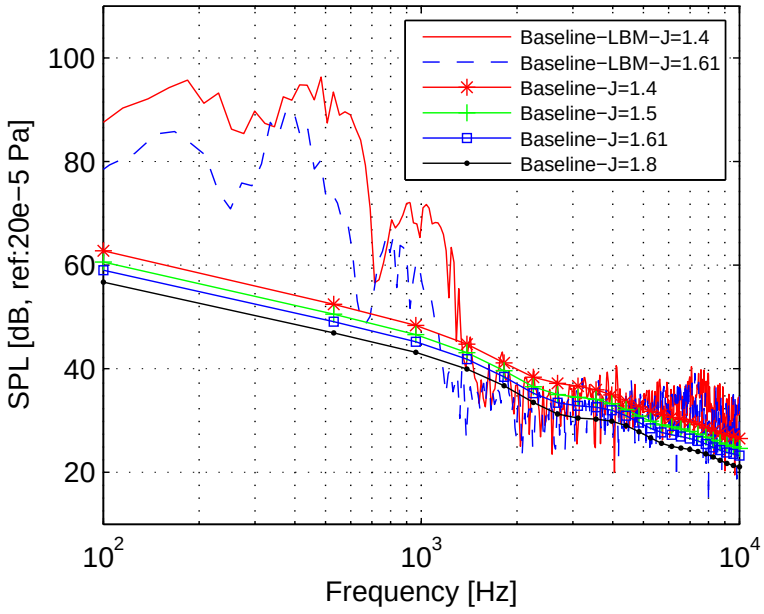


(a) Baseline propeller.

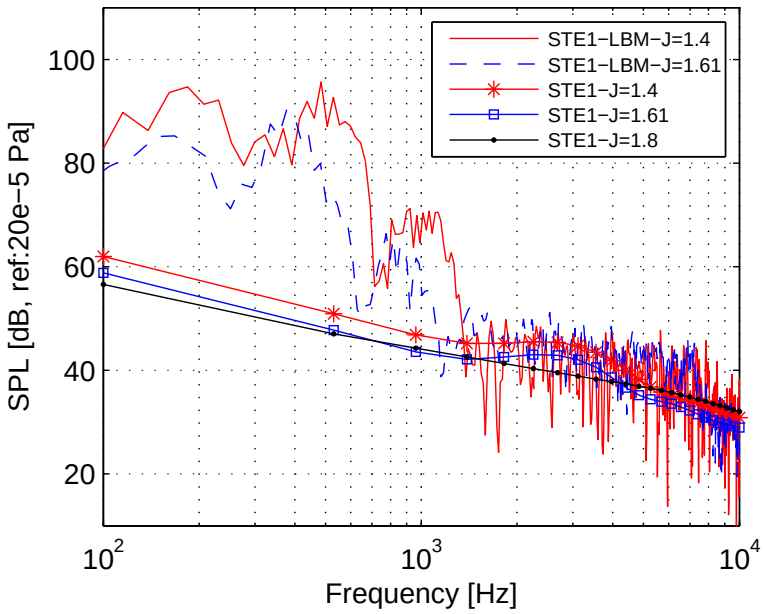


(b) Serrated propeller STE1.

Figure 5.14: Effect of the advance ratio on the trailing edge noise emitted by the baseline and the $STE1$ blades.

at low frequencies. The spectrum of $STE1$ at $J = 1.8$ shows a different behaviour at high frequency, it is not yet understood if this result is physical or not. Further investigations on other serrated blades will be done to clarify this tendency.
Overall, the tendencies of noise emission differences observed in this study for the baseline and the serrated blades are consistent with results of Moreau et al. [36], for a flat plate case and Arce Leon et al. [113] for an isolated airfoil case with different geometries and operating conditions.

## 5.6 Directivity patterns

Figures 5.15 and 5.16 show the sound pressure level directivity pattern, predicted by the analytical model, for the baseline and the serrated blades $STE1$, $STE3$ and $STE6$ at different reduced frequencies $kc = 0.5, 2.375, 4.25, 8$ which correspond respectively to frequencies $f = 330Hz, 1.5kHz, 2.8kHz, 5.3kHz$.
At $kc = 0.5$, figure 5.15 shows that both $STE3$ and $STE6$ blades reduce the noise levels of the baseline blade at all angular positions. However, $STE1$ produces equivalent noise levels to the baseline blade. For higher frequencies a noise increase is observed with all serrated blades. At $kc = 2.375$, $STE1$ produces less noise increase than $STE3$ and $STE6$, when increasing the frequency to $kc = 4.25$ (figure 5.16) the tendency changes, the noise increase generated by $STE1$ surpasses $STE3$ and $STE6$. The same tendency remains at $kc = 8$.
Overall, the results show that serrations reduce noise at low frequencies as discussed earlier, this can be explained by the destructive scattering interference effect [37]. Moreover, the trailing edge serrations do not modify the directivity of the radiated trailing edge noise and their effect on the radiated noise is independent of the observer position. This was found to be the case at all studied frequencies whether a noise reduction occurs or not. The same result was pointed by Moreau et al. [36] for the sawtooth trailing edge noise of a flat plate.

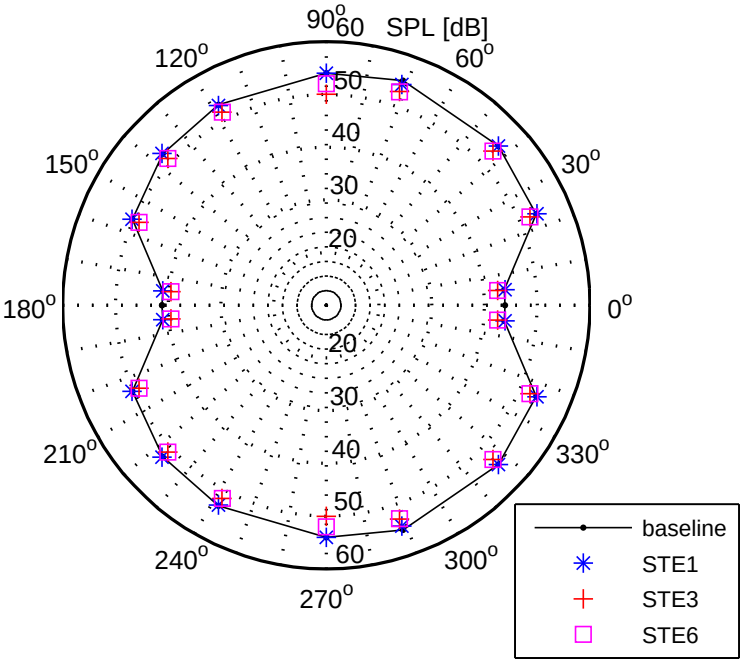


(a) $kc = 0.5$.

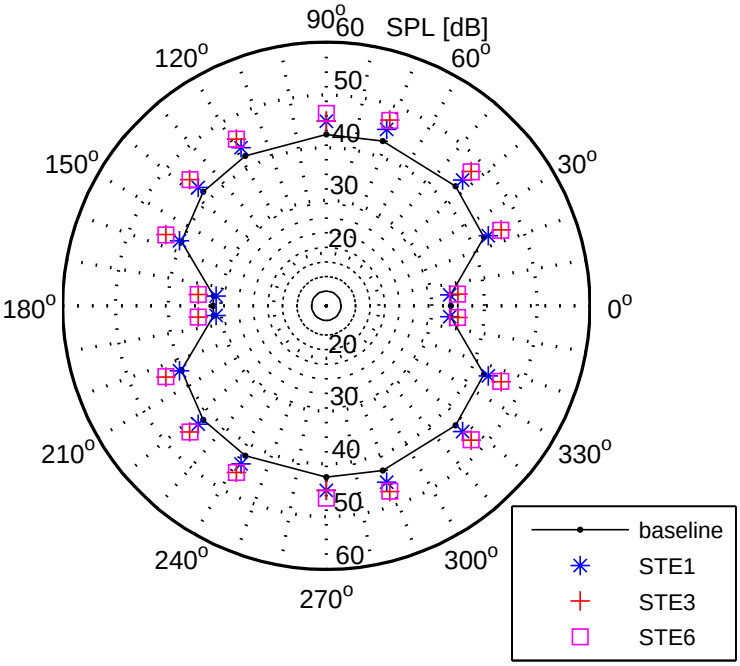


(b) $kc = 2.375$.

Figure 5.15: Trailing edge noise directivity pattern for the baseline and trailing edge serrated blades for $kc = 0.5$ and $kc = 2.375$.

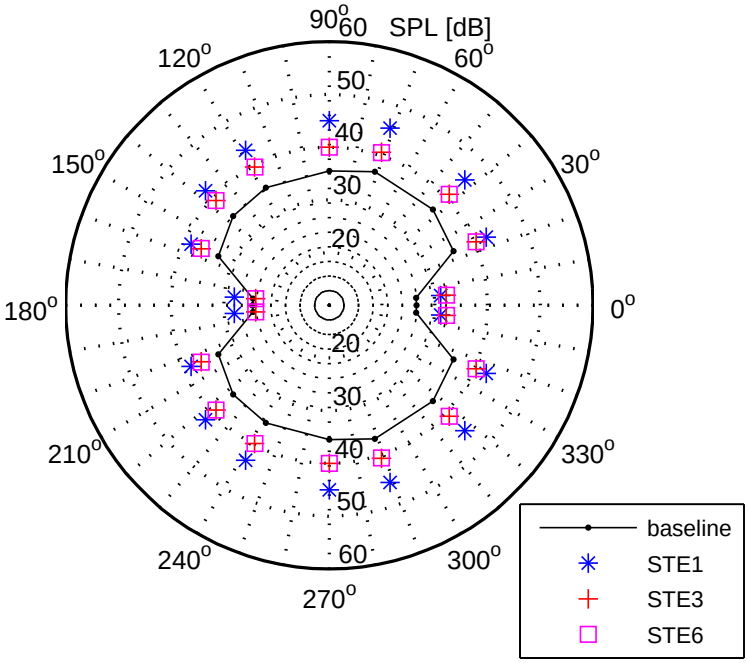


(a) $kc = 4.25$.

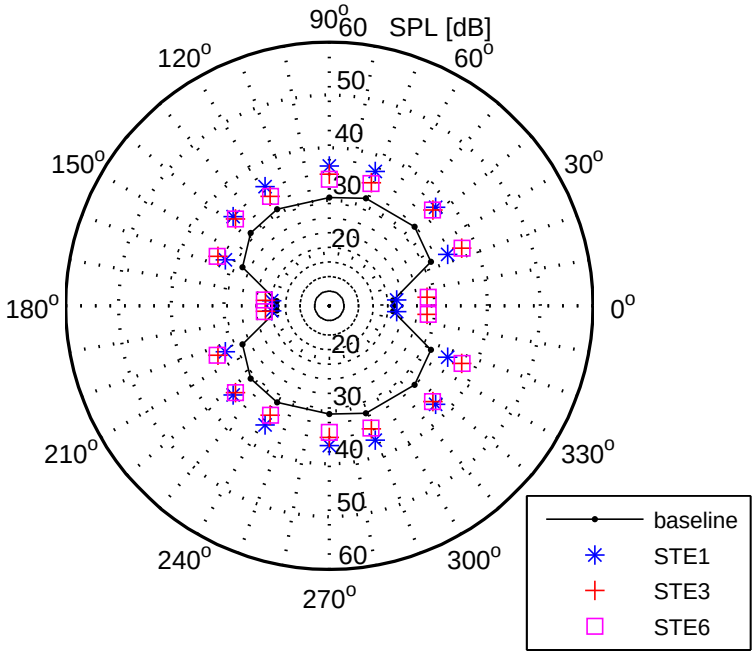


(b) $kc = 8$.

Figure 5.16: Trailing edge noise directivity pattern for the baseline and trailing edge serrated blades for $kc = 4.25$ and $kc = 8$.

## 5.7 Aerodynamic performance

In this section, the effect of the trailing edge serrations on the flow around the baseline and $STE1$, $STE3$ and $STE4$ blades is investigated. Results are extracted from the LBM simulations carried out for $J = 1.4$. The pressure and the skin friction coefficients distributions are evaluated along the blade chord at four spanwise locations: 25%, 50%, 75% and 95% for the nearest peak and valley as shown in figure 5.17.

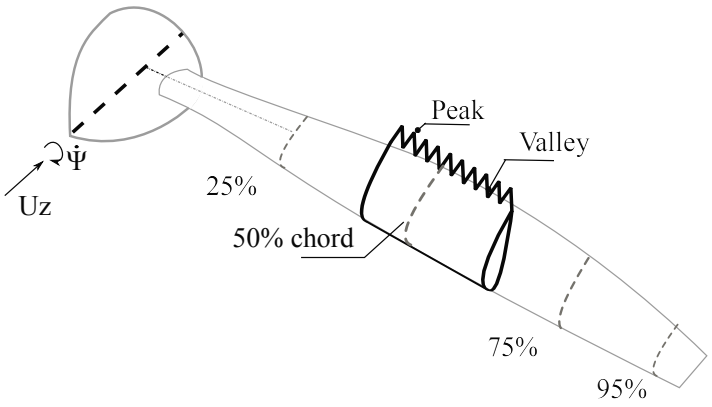


Figure 5.17: Chordwise and spanwise positions for the evaluation of the local flow features around trailing edge serrated blades.

### 5.7.1 Pressure and skin friction coefficients

In terms of pressure distribution shown in figure 5.18, significant differences between blade geometries exist at 25% span, these latter become less marked when moving toward the tip in the region of the blade where thrust is effectively produced. For the 50%, 75%, and 95% spanwise locations, the pressure distribution on the suction side is only lightly affected upstream of the 40% chord location. The main feature is the presence of a vortex attached to the leading edge region that is shaping the pressure and skin friction distributions. This vortex is caused by the small leading edge radius of the NACA16-series and the presence of sweep [116]. Downstream of the 40% chord location, differences become significant depending on the blade geometry and the location near to a peak or a valley. This behaviour contrasts with that of trailing edge inserts which do not modify the pressure distribution upstream [117,118].

The pressure side is essentially unaffected. Peaks have a detrimental influence on the generation of thrust since the area under the $C_p$ curve is less than for the baseline blade. The suction side is mainly affected from about 40% chord to the trailing edge whereas the pressure side in unaffected. Increasing the serration amplitude $h/\delta$ accentuates the deficit. This effect is the strongest at the 50% and 75% span where most of the thrust is made. The area deficit near peaks is at least partially compensated for by an increase in area near valleys. Decreasing the serration wavelength $\lambda$, hence a higher $h/\lambda$, results in an area decrease under the $C_p$ curve.

The skin friction distribution around 25% span exhibits the strongest changes depending on blade geometry and proximity to peak/valley (figure 6.20). Outboard of this location, the pressure side is mostly unaffected as well, but for the region near the trailing edge where peaks come with a decrease in local $C_f$ and valleys come with an increase. On the suction side, the overall trend is toward less skin friction especially near the blade tip. At 50% span, the differences around the leading edge are significant, then, downstream of it, skin friction is reduced. At 75% span, all blade geometries result in a reduction downstream of the 40% chord location; the behaviour upstream of that location depends on the blades geometry. Large serrations of small wavelength (high $h/\delta$ and high $h/\lambda$) are favourable.

### 5.7.2 Vorticity

For the serrated trailing edge blades, the vorticity magnitude upstream of the serrations is unchanged as can be seen in figure 5.20. All blades bear the traces of the leading edge vortex. Downstream, peaks come with low vorticity values in the immediate vicinity of the edge whereas valleys come with high values near the edge. This behaviour could correspond to the smaller velocity deficit, due to increased mixing, observed in the wake of valleys [119].

### 5.7.3 Overall performance

For the serrated trailing edge blades, the reduction in area under the $C_p$ curve results in less thrust as can be seen from the thrust coefficient $C_T$ in figure 5.21 although the paired reduction in pressure drag as well as the decrease of the skin friction thanks to

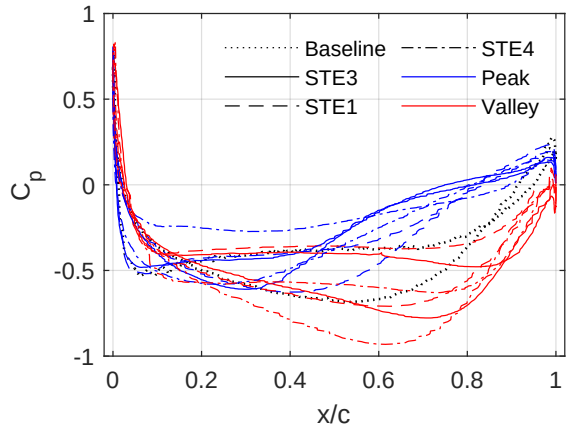


(a) $C_p$ – 25% radius.

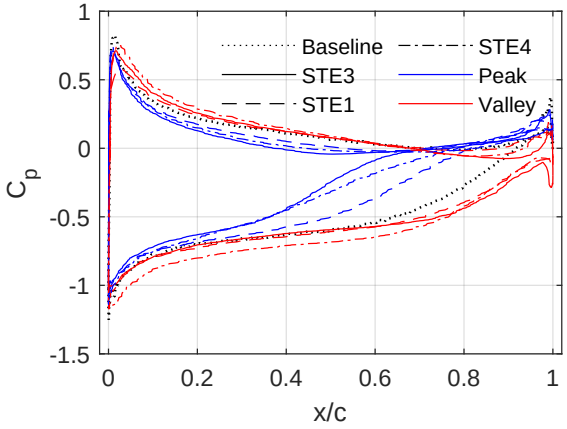


(b) $C_p$ – 50% radius.

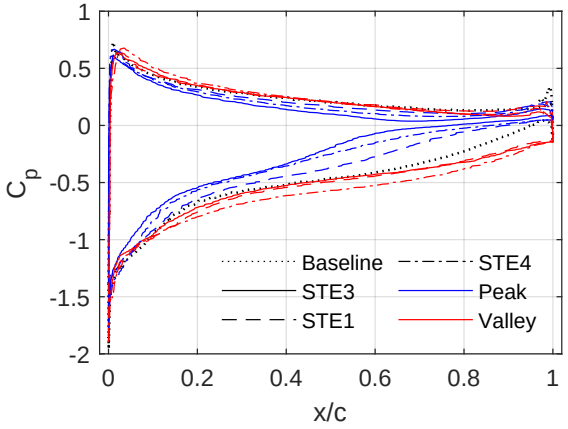


(c) $C_p$ – 75% radius.

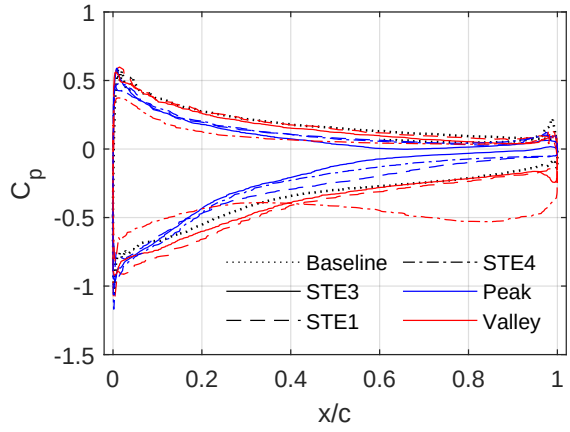


(d) $C_p$ – 95% radius.

Figure 5.18: Pressure coefficient distribution at different spanwise locations for the serrated trailing edge blades.

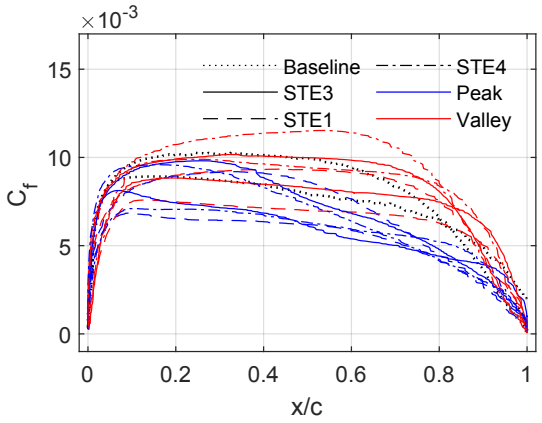


(a) $C_f$ – 25% radius.

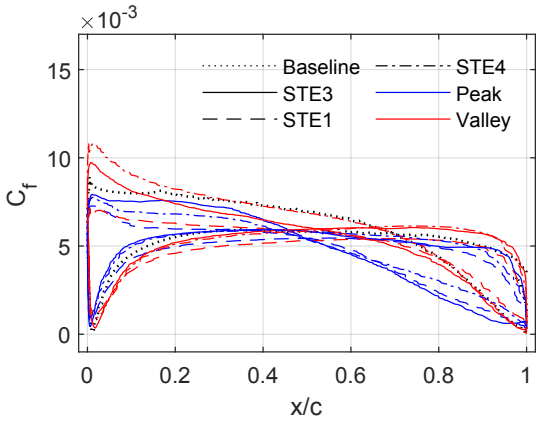


(b) $C_f$ – 50% radius.

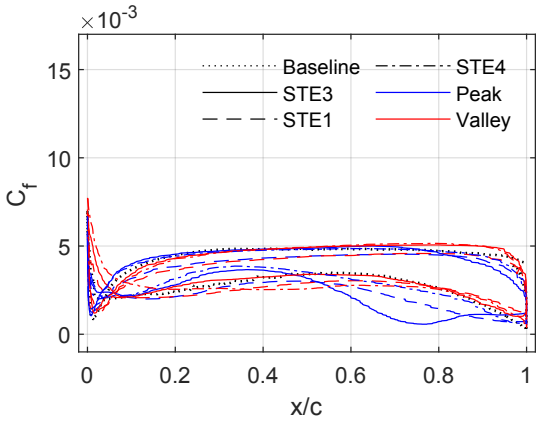


(c) $C_f$ – 75% radius.

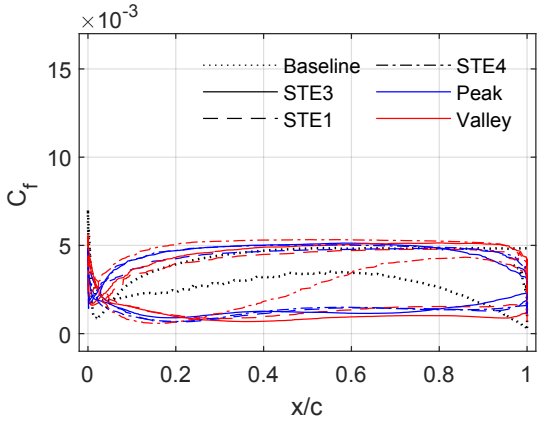


(d) $C_f$ – 95% radius.

Figure 5.19: Skin friction coefficient distribution at different spanwise locations for the serrated trailing edge blades.

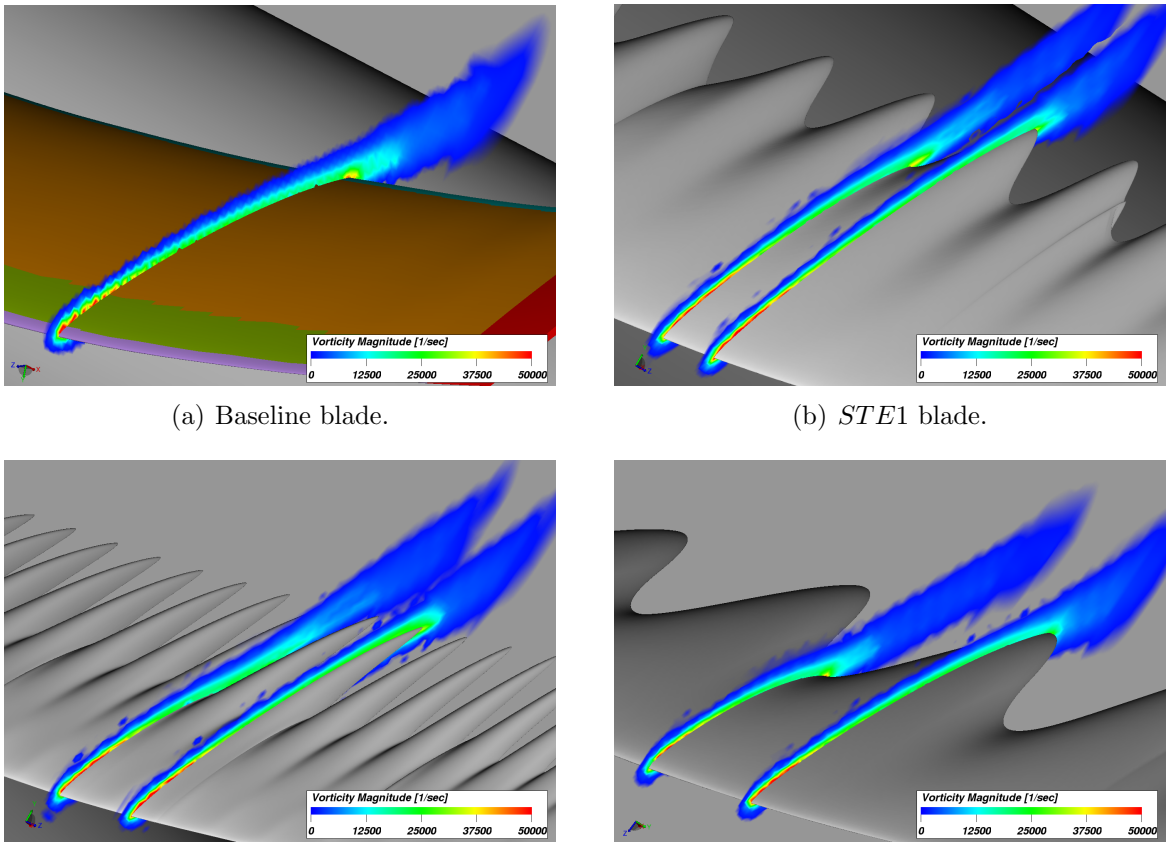


(a) Baseline blade.

(b) $STE1$ blade.

(c) $STE3$ blade.

(d) $STE4$ blade.

Figure 5.20: Vorticity contours around 75% radius for the baseline and the serrated trailing edge blades.

the streamwise streaks also results in less power $C_P$ . Hence the propulsive efficiency is unchanged.

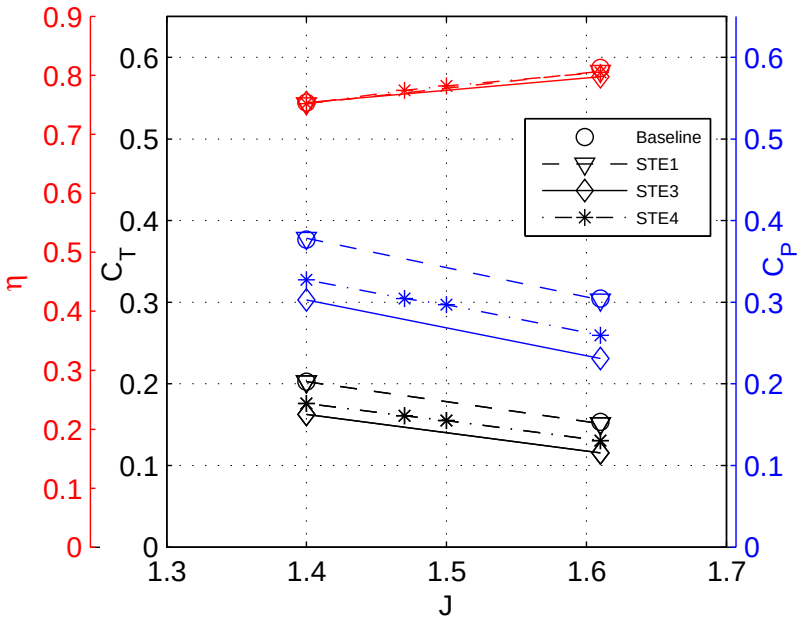


Figure 5.21: Aerodynamic performance for the trailing edge serrated blades.

## 5.8 Conclusion

This chapter investigates the potential of trailing edge noise reduction by applying sawtooth trailing edge serrations on a propeller. Different serrations parameters are tested using two methods: A recent analytical frequency-domain model for predicting noise from airfoils with straight edges to serrated edges, extended to rotating blades by using a strip approach and time-domain simulations based on the Lattice Boltzmann model.

Amiet's model for predicting trailing edge noise was used to predict the trailing edge noise emitted by the baseline propeller and compare the obtained spectrum with the other two methods. The results show that Amiet's model combined with CFD-RANS results used as input for the wall pressure spectra around the blade predicts the tendency of the noise emitted by the blade at high frequencies compared to the LBM spectrum. The precision of the result depends on the wall pressure statistics model. It

was found that Amiet and Schlinker model predicts the overall tendency of the noise spectrum though it overpredicts the levels, while Goody's model fails to predict the tendency and underestimates the SPL levels. The mean gradient model predicts the correct tendency at high frequencies with a good approximation of the sound levels since it was developed for flows with adverse pressure gradient. Furthermore, the spectrum obtained with the analytical model of Lyu predicts the tendency and the SPL levels with a good precision at high frequencies.

A study was conducted to assess Lyu's model, it was found that the zero order approximation is computationally relatively cheap and is able to capture relative variations but comes with a loss of accuracy, while the first order approximation is more expensive in computational time but gives more accurate results. The number of segments affects the analytical solution which seems to converge for a large number of segments. Further investigations are needed to determine the limit of convergence with increasing the segments number since the computational cost scales directly with the number of segments.

The results of the parametric study conducted with sawtooth trailing edge serrated blades show that the use of serrations reduces the noise emitted by the propeller at low to mid frequencies but induces a noise increase at high frequencies. The sharpest serrations are found to achieve the better performance in terms of reducing noise.

The inspection of the skin and pressure coefficients around the serrated blades shows that the flow is highly affected by the introduction of the serrations. The thrust and power performance are also influenced even though the efficiency is not impacted.

# *Chapter 6*
# *Propellers leading edge noise reduction using sawtooth serrations*

# Chapter 6
# Propellers leading edge noise reduction using sawtooth serrations

In this chapter, the leading edge noise reduction performance of sawtooth serrations applied to propellers is investigated. First, the analytical formulation used to predict leading edge noise from serrated airfoils is detailed and validated against experimental data. Then the formulation is extended to predict leading edge noise from rotating blades. The model is assessed by comparison to the LBM simulations results and the effect of the order approximation and the number of segments on the predicted spectra is studied. A parametric study is conducted with different serrations parameters to define the geometry which yields the maximum noise reduction. Furthermore, the effect of flow conditions on the predicted spectra is investigated along with the directivity patterns. A further objective of this chapter is to investigate the physical mechanisms responsible for the change in the leading edge noise radiation due to the introduction of sawtooth serrated leading edges are investigated.
The results presented in this chapter have been presented in AIAA aeroacoustics conference [120].

## 6.1 Analytical formulation

In this section, the detailed derivation of the turbulence interaction noise model for single airfoil with serrated leading edge developed by Lyu et al. [58] is presented.

### 6.1.1 The mathematical model

Consider an airfoil with leading edge serrations. The airfoil is considered as an infinitesimally thin plate with an averaged chord length $c$ and spanwise length $L$. $x^{'}$ and $y^{'}$ denote the streamwise and spanwise coordinates respectively and $z^{'}$ is the direction perpendicular to the airfoil as shown in figure 6.1. The observer is located at $(x_1, x_2, x_3)$. The sawtooth serrations are described by their root-to-tip length $2h$ and their wavelength $\lambda$. $\sigma = 4h/\lambda$ defines the sharpness of serrations.

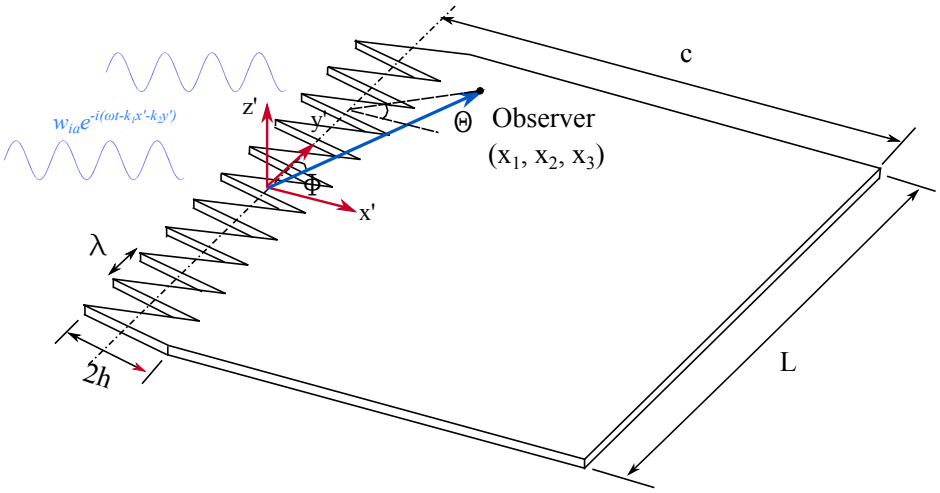


Figure 6.1: Sketch of a flat plate with serrated leading edge and related coordinate system.

The serrated edge is defined by a profile function $H(y^{'})$ for which the origin of the coordinates is chosen so that $H(y^{'})$ is an oscillatory function of zero mean and that $H(y^{'}) = 0$ in the absence of serrations.

The unsteady upwash disturbance that exists upstream the leading edge may be expressed as an integral of different gust components after applying a spatial and time Fourier transformation. The specific component of frequency $\omega$ takes the form

$$w = w_i e^{-i(\omega t - k_1 x^{'} - k_2 y^{'})} \tag{6.1}$$

where $w_i$ is the magnitude of the upwash velocity and $k_1$ and $k_2$ the wavenumbers in the chordwise and spanwise, respectively. According to Amiet [13], the induced potential field by an infinite flat plate due to the gust impingement at $z^{'} = 0$ can be found as

$$\phi_i = -\Phi_{ia} e^{-i(\omega t - k_1 x^{'} - k_2 y^{'})} \tag{6.2}$$

where $\Phi_{ia} \equiv -w_i / \sqrt{(k_1\beta + kM/\beta)^2 + k_2^2 - (k/\beta)^2}$. The minus sign in equation 6.2 is to cancel the positive gust. Schwartzchild technique is used to calculate the second part of the potential field $\phi$. Thus the boundary conditions for $\phi$ read

$$\begin{cases} \frac{\partial \phi}{\partial z^{'}} = 0 & x^{'} > H(y^{'}) \\ \phi = \Phi_{ia} e^{-i(\omega t - k_1 x^{'} - k_2 y^{'})} & x^{'} \leq H(y^{'}) \end{cases} \tag{6.3}$$

In the airfoil fixed frame, the equation governing the second part potential field $\phi$ remains the same as that of the induced total potential field, i.e.

$$\nabla^2\phi - \frac{1}{c^2}\left(\frac{\partial}{\partial t} + U\frac{\partial}{\partial x'}\right)^2 \phi = 0 \tag{6.4}$$

where $c_0$ is the speed of sound. With the assumption of harmonic perturbation $\phi = \Phi(x', y', z')e^{-i\omega t}$, equation 6.4 reduces to

$$\beta^2\frac{\partial^2\Phi}{\partial x'^2} + \frac{\partial^2\Phi}{\partial y'^2} + \frac{\partial^2\Phi}{\partial z'^2} + 2ikM\frac{\partial\Phi}{\partial x'} + k^2\Phi = 0 \tag{6.5}$$

where $k = \omega/c_0$, $\beta^2 = 1 - M^2$ and $M = U/c_0$

The coordinate transformation $x = x' - H(y')$, $y = y'$, $z = z'$ is then applied to make the boundary conditions independent of $y'$ and leads to the following differential equation

$$\left(\beta^2 + H'^2(y)\right)\frac{\partial^2\Phi}{\partial x^2} + \frac{\partial^2\Phi}{\partial y^2} + \frac{\partial^2\Phi}{\partial z^2} - 2H'(y)\frac{\partial^2\Phi}{\partial x\partial y} + \left(2iMk - H''(y)\right)\frac{\partial\Phi}{\partial x} + k^2\Phi = 0 \tag{6.6}$$

where $H'(y)$ and $H''(y)$ denote the first and second derivatives of $H(y)$ defined as the profile function of the serrated leading edge shown in figure 6.2.

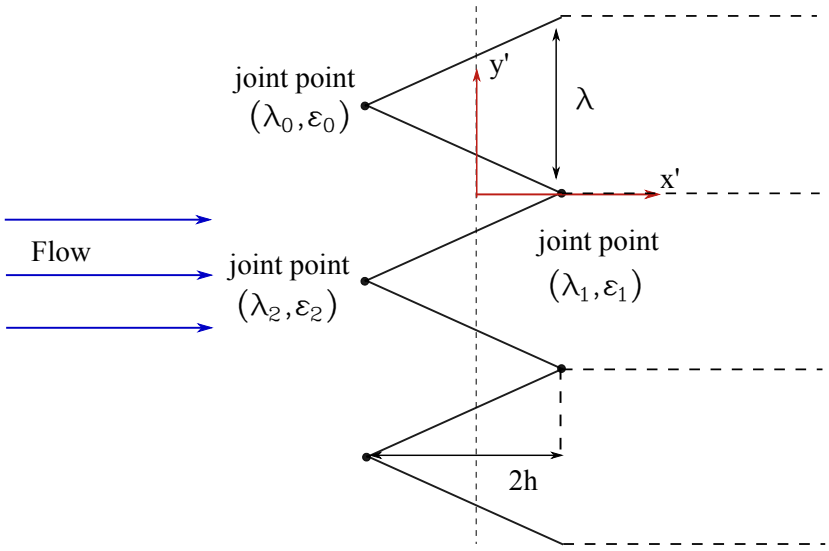


Figure 6.2: The schematic of leading edge serration profile.

The boundary conditions now read

$$\begin{cases} \Phi(x,y,0) = -\Phi_{ia} e^{i(k_1 x + k_2 y)} e^{ik_1 H(y)} & x \leq 0 \\ \partial\Phi(x,y,0)/\partial z = 0 & x > 0 \end{cases} \tag{6.7}$$

The Fourier expansion is used to solve equation (6.6) as it will be explained in the following section.

### 6.1.2 Fourier expansion

Considering the infinite span assumption and the serration periodicity, the induced potential due to gust impingement can be expanded using Fourier series in terms of the new coordinates $(x, y, z)$, as

$$\Phi(x,y,z) = \sum_{-\infty}^{\infty} \Phi_n(x,z)\, e^{ik_{2n}y} \tag{6.8}$$

where $k_{2n} = k_2 + 2n\pi/\lambda$

Substituting the above expression into equation (6.6) yields

$$\left(\beta^2 + H'^2(y)\right)\frac{\partial^2}{\partial x^2} + \frac{\partial^2}{\partial y^2} + \frac{\partial^2}{\partial z^2} - 2H'(y)\frac{\partial^2}{\partial x \partial y} + \left(2iMk - H''(y)\right)\frac{\partial}{\partial x} + k^2 \times \left\{\sum_{-\infty}^{\infty} \Phi_n(x,z)\, e^{ik_{2n}y}\right\} = 0 \tag{6.9}$$

Multiplying equation (6.9) by $e^{-ik_{2n'}y}$, then integrating it over $y$ from $-\lambda/2$ to $\lambda/2$ gives

$$\left\{\beta^2\frac{\partial^2}{\partial x^2} + \frac{\partial^2}{\partial z^2} + 2iMk\frac{\partial}{\partial x} + \left(k^2 - k_{2n'}^2\right)\right\}\Phi_{n'} + \frac{1}{\lambda}\int_{-\lambda/2}^{\lambda/2}\sum_{-\infty}^{\infty}\left\{H'^2\frac{\partial^2}{\partial x^2} - \left(H'' + 2ik_{2n}H'\right)\frac{\partial}{\partial x}\right\}\Phi_n e^{i2(n-n')\pi/\lambda y} dy = 0 \tag{6.10}$$

Following the same procedure used for the trailing edge serrations, a set of differential equations is obtained which can be written as

$$D\Phi = A\Phi + B\frac{\partial\Phi}{\partial x} \tag{6.11}$$

where $D = \left\{(\beta^2 + \sigma^2)\frac{\partial^2}{\partial x^2} + \frac{\partial^2}{\partial z^2} + 2iMk\frac{\partial}{\partial x}\right\}$ is a linear operator. $\Phi = \left(...\Phi_{-n'}(x,z), \Phi_{-n'+1}(x,z), ...\Phi_{n'-1}(x,z), \Phi_{n'}(x,z)\right)^T$ is a vector of functions where $T$

denotes the transpose of the matrix. Matrices $A$ and $B$ express the coefficient matrices of $\Phi$ and $\partial\Phi/\partial x$. $A_{ml}$ and $B_{ml}$ represent the entry corresponding to mode $m$ in row and $l$ in column of matrix $A$ and $B$ and are defined the same way as for the trailing edge serrations.

Substituting the profile geometry into the boundary conditions (equation 6.7) and performing the same Fourier expansions gives

$$\begin{cases} \Phi_n(x,0) = -\Phi_{ia} a_n e^{ik_1 x} & x \leq 0 \\ \partial\Phi_n(x,0)/\partial z = 0 & x > 0 \end{cases} \tag{6.12}$$

### 6.1.3 Acoustic formulation

Following the same procedure used by Amiet [13, 112], the induced potential field is solved then the far field sound is evaluated.

To obtain the induced potential field, equation 6.6 together with the boundary conditions in equation 6.12 are solved using an iteration process [58]. The exact solutions $\Phi_t$ can be expressed as

$$\Phi_t(x,0) = N(x) + C^{(1)}(x) + C^{(2)}(x) + C^{(3)}(x) + ... \tag{6.13}$$

where $N$ denotes the non-coupled part, while the the coupled parts are denoted by $C^{(i)}$ $(i = 1, 2, 3...)$. The entries of $N$ and $C^{(1)}$ of the first iteration corresponding to mode $n^{'}$ are expressed by

$$N_{n'}(x) = -\Phi_{ia} e^{ik_1 x} a_{n'} \left((1+i) E^*(\mu_{n'} x)\right) \tag{6.14}$$

$$\begin{aligned} C^1_{n'}(x) = &- \Phi_{ia} e^{ik_1 x}(1+i) \sum_{m=-\infty}^{\infty} \alpha_{n'm} a_m \Bigg( ik_1 \left(E^*(\mu_{n'} x) - E^*(\mu_n x)\right) \\ &+ \sqrt{\frac{\mu_m}{2\pi x}} \left(e^{-i\mu_{n'} x} - e^{-i\mu_m x}\right) \Bigg) \end{aligned} \tag{6.15}$$

where

$$\begin{aligned} \mu_{n'} &= -K_{n'} + k_1 + \frac{kM}{\beta^2 + \sigma^2} \\ E^*(x) &= \int_0^x \frac{e^{-it}}{\sqrt{2\pi t}} dt \end{aligned} \tag{6.16}$$

The induced potential due to gust impingement is obtained by summing the modal solutions over all different modes and transforming back to the physical coordinate system.

$$\Phi_t(x^{'}, y^{'}, 0) = \sum_{n^{'}=-\infty}^{\infty} \left[ N_{n^{'}} + C_{n^{'}}^{(1)} + C_{n^{'}}^{(2)} + ... \right] \left( x^{'} - H(y^{'}), 0 \right) e^{ik_{2n^{'}} y^{'}} \tag{6.17}$$

where the functions $N_{n^{'}}$ and $C_{n^{'}}^{(1)}$ are defined in equations (6.14, 6.15), $C_{n^{'}}^{(2)}$ is the result of the second order iteration and the terms in the parenthesis are the arguments for the $N_{n^{'}}$ and $C_{n^{'}}^{(i)}$ functions.
The induced potential field in the time domain can be written as

$$\phi_t(x^{'}, y^{'}, 0, t) = \sum_{n^{'}=-\infty}^{\infty} \left[ N_{n^{'}} + C_{n^{'}}^{(1)} + C_{n^{'}}^{(2)} + ... \right] \left( x^{'} - H(y^{'}), 0 \right) e^{ik_{2n^{'}} y^{'}} e^{-i\omega t} \tag{6.18}$$

The pressure field can thus be found by the equation

$$p = -\rho U \left( \frac{\partial \phi_t}{\partial x^{'}} - ik_1 \phi_t \right) \tag{6.19}$$

Therefore the pressure jump $\Delta p$ across the flat plate is given by

$$\Delta p(x^{'}, y^{'}, 0, t) = 2 \sum_{n^{'}=-\infty}^{\infty} \left[ P_{n^{'}}^{(0)} + P_{n^{'}}^{(1)} + P_{n^{'}}^{(2)} + ... \right] \left( x^{'} - H(y^{'}), 0 \right) e^{ik_{2n^{'}} y^{'}} e^{-i\omega t} \tag{6.20}$$

where

$$P_{n^{'}}^{(0)}(x) = \rho U \Phi_{ia} \left(1 + i\right) e^{ik_1 x} a_{n^{'}} \sqrt{\mu_{n^{'}}} \frac{1}{\sqrt{2\pi x}} e^{-i\mu_{n^{'}} x} \tag{6.21}$$

and

$$\begin{aligned} P_{n^{'}}^{(1)}(x) = {} & \rho U \Phi_{ia} \left(1 + i\right) e^{ik_1 x} \\ & \sum_{m=-\infty}^{\infty} \alpha_{n^{'}m} a_m \left[ ik_1 \frac{1}{\sqrt{2\pi x}} \left( \sqrt{\mu_{n^{'}}} e^{-i\mu_{n^{'}} x} - \sqrt{\mu_m} e^{-i\mu_m x} \right) \right. \\ & \left. -i \sqrt{\frac{\mu_m}{2\pi x}} \left( \mu_{n^{'}} e^{-i\mu_{n^{'}} x} - \mu_m e^{-i\mu_m x} \right) - \frac{1}{2} \sqrt{\frac{\mu_m}{2\pi x}} \frac{1}{x} \left( e^{-i\mu_{n^{'}} x} - e^{-i\mu_m x} \right) \right] \end{aligned} \tag{6.22}$$

Having obtained the pressure jump, the far field sound induced by the scattered surface pressure is found using the surface pressure integral. It is expressed as

$$p_f\left(x,\omega,k_2\right)=2\rho U\Phi_{ia}\left(\frac{-i\omega x_3}{4\pi c_0 S_0^2}\right)\lambda\frac{sin\left(\left(N+1/2\right)\lambda\left(k_2-kx_2/S_0\right)\right)}{sin\left(\lambda/2\left(k_2-kx_2/S_0\right)\right)}LE(\omega,k_1,k_2) \tag{6.23}$$

$(2N+1)$ is the number of sawtooth on the lading edge. $LE$ is the far field sound gust response function defined as:

$$\begin{aligned}LE(\omega,k_1,k_2)=&(1+i)\frac{1}{\lambda}e^{-ik(M_0x_1-S_0)/\beta^2}e^{ik(M_0-x_1/S_0)h/\beta^2}\\&\sum_{n'=-\infty}^{+\infty}\left(\Theta_{n'}^{(0)}+\Theta_{n'}^{(1)}+\Theta_{n'}^{(2)}+...\right)\end{aligned} \tag{6.24}$$

The $0^{th}$ and $1^{st}$ order radiation functions are expressed as:

$$\Theta_{n'}^{(0)}=a_{n'}\sqrt{\mu_{n'}}S_{n'n'} \tag{6.25a}$$

$$\begin{aligned}\Theta_{n'}^{(1)}=&\sum_{m=-\infty}^{+\infty}\alpha_{n'm}a_m\left[ik_1\left(\sqrt{\mu_{n'}}S_{n'n'}-\sqrt{\mu_m}S_{n'm}\right)-i\sqrt{\mu_m}\left(\mu_{n'}S_{n'n'}-\mu_mS_{n'm}\right)\right.\\&\left.-\sqrt{\mu_m}\left(T_{n'n'}-T_{n'm}\right)\right]\end{aligned} \tag{6.25b}$$

The functions $S_{nm}$ and $T_{nm}$ in the above equations are given by

$$\begin{aligned}S_{nm}=&\sum_{j=0}^{1}\frac{1}{\kappa_{nj}}\left\{\frac{1}{\sqrt{\eta_{Am}}}\left(e^{i\kappa_{nj}\lambda_{j+1}}E^*(\eta_{Am}(c-\epsilon_{j+1)})-e^{i\kappa_{nj}\lambda_j}E^*(\eta_{Am}(c-\epsilon_j))\right)\right.\\&\left.-\frac{1}{\sqrt{\eta_{Bnmj}}}e^{i\kappa_{nj}(\lambda_j+(c-\epsilon_j)/\sigma_j)}\left(E^*(\eta_{Bnmj}(c-\epsilon_{j+1}))-E^*(\eta_{Bnmj}(c-\epsilon_j))\right)\right\}\end{aligned} \tag{6.26}$$

$$\begin{aligned}T_{nm}=&\sum_{j=0}^{1}\frac{1}{\kappa_{nj}}\left\{\frac{-i\eta_{Am}}{\sqrt{\eta_{Am}}}\left(e^{i\kappa_{nj}\lambda_{j+1}}E^*(\eta_{Am}(c-\epsilon_{j+1)})-e^{i\kappa_{nj}\lambda_j}E^*(\eta_{Am}(c-\epsilon_j))\right)\right.\\&\left.+\frac{i\eta_{Bnmj}}{\sqrt{\eta_{Bnmj}}}e^{i\kappa_{nj}(\lambda_j+(c-\epsilon_j)/\sigma_j)}\left(E^*(\eta_{Bnmj}(c-\epsilon_{j+1}))-E^*(\eta_{Bnmj}(c-\epsilon_j))\right)\right\}\end{aligned} \tag{6.27}$$

where

$$\begin{aligned}
\eta_{Am} &= -K_m + kM/(\beta^2+\sigma^2) - k(M - x_1/S_0)/\beta^2 \\
\eta_{Bnmj} &= -K_m + kM/(\beta^2+\sigma^2) + (k_{2n} - kx_2/S_0)/\sigma_j \\
\kappa_{nj} &= k_{2n} - kx_2/S_0 + k(M - x_1/S_0)\sigma_j/\beta^2
\end{aligned} \tag{6.28}$$

**Far field sound power spectrum**

The far field sound power spectral density (PSD) $S_{pp}$ can be written as

$$\begin{aligned}
S_{pp}(x,\omega) &= \lim_{T\to\infty}\left(\frac{\pi}{T}\left\langle p_f(x,\omega)p_f^*(x,\omega)\right\rangle\right) \\
&= (2\pi LU)\left(\frac{\omega x_3\rho_0}{\pi c_0 S_0^2}\right)^2 \sum_{m=-\infty}^{+\infty} \frac{\Phi_{ww}\left(\omega/U, kx_2/S_0 + 2m\pi/\lambda\right)}{|\gamma_d\left(\omega/U, kx_2/S_0 + 2m\pi/\lambda\right)|^2} \\
&\times |LE\left(\omega/U, kx_2/S_0 + 2m\pi/\lambda\right)|^2
\end{aligned} \tag{6.29}$$

When the observer is in the mid-span plane, i.e. $x_2 = 0$, the sound pressure PSD reduces to

$$S_{pp}(x,\omega) = (2\pi LU)\left(\frac{\omega x_3\rho_0}{\pi c_0 S_0^2}\right)^2 \sum_{m=-\infty}^{+\infty} \frac{\Phi_{ww}\left(\omega/U, 2m\pi/\lambda\right)}{|\gamma_d\left(\omega/U, 2m\pi/\lambda\right)|^2} |LE\left(\omega, \omega/U, 2m\pi/\lambda\right|^2 \tag{6.30}$$

where $\gamma_d(k_1,k_2) = \sqrt{(k_1\beta + kM/\beta)^2 + k_2^2 - (k/\beta)^2}$

The Von Karman model for the isotropic turbulence $\Phi_{ww}$ is adopted as detailed in section (2.6).

**Model's validation**

The serrated leading edge model is assessed by comparison with experiments [54]. The experiments were conducted for a flat plate of mean chord length $c = 0.175m$ and span length $d = 0.45m$, in a flow velocity of $U = 60m/s$. The Von Karman model for isotropic turbulence is used in the analytical model with an experimentally measured streamwise integral length scale of turbulence $L_t = 0.006m$ and turbulent intensity $T_u = 2.5\%$.

Since this model is computationally expensive, an investigation on the effect of the different modes on the solution is necessary. Figure 6.3 shows the convergence results for a serration with amplitude $h/c = 0.067$ and a spanwise wavelength $\lambda/c = 0.067$. It is clear that the $0^{th}$ order solution can provide a good approximation of the solution

with a truncated summation over $m$ and $n^{'}$, in equations 6.25a, 6.25b and 6.30, at $m$ =30. The $1^{st}$ order solution is in better agreement with experimental data at high frequencies, but with a considerable increase in the computational time.

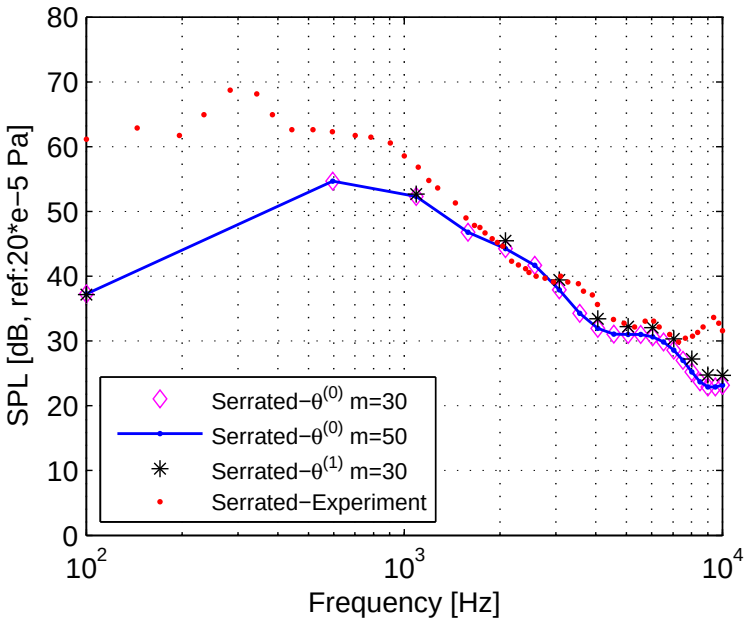


Figure 6.3: Effect of the $0^{th}$ and $1^{st}$ order solution on the result compared with experimental data [54].

For the identical serration, a comparison between the results obtained by the analytical model with experimental data is shown in figure 6.4. The numerical results agree very well with experiments in the middle to high frequency range. However, at low frequencies the experimental data exhibit higher levels of noise. This is due to the dominance of jet noise and to grid generated narrow band vortex shedding that interacts with the airfoil, as explained by Narayanan [54]. This suggests that the present model captures the essential physics and gives good prediction of the serrated leading edge noise. It is worth pointing that Amiet's model underestimates the noise levels at low to middle frequencies for the baseline configuration compared to the present model prediction, but the two models predicts well noise levels at high frequencies.

To evaluate the behaviour of the serrated leading edge model, a parametric study is conducted with different serration parameters. First, the wavelength is fixed to the value $\lambda = L_t$ and the amplitude varies. The results are shown in figure 6.5(a). The

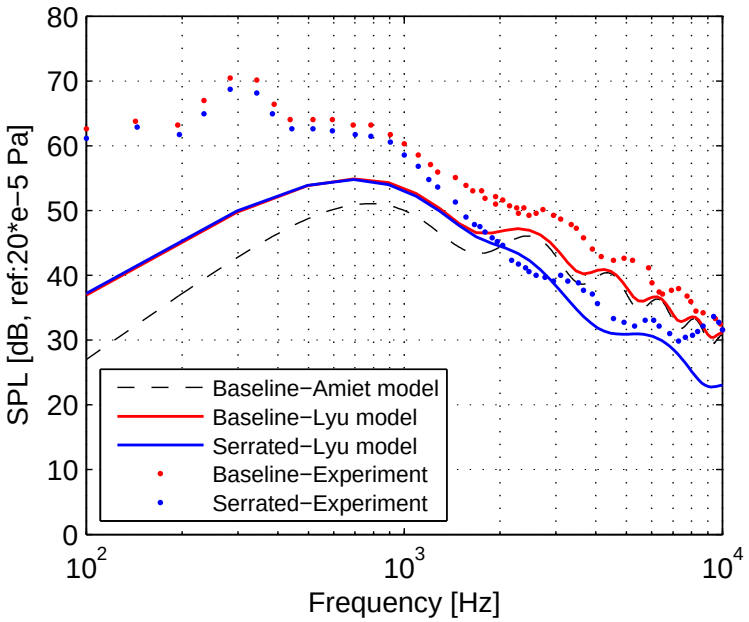


Figure 6.4: Comparison of the results obtained with the present model with experimental data [54] for baseline and serrated flat plates.

serration $h = (1/6)L_t$ have no effect on reducing noise. However, serrations with large amplitude prove to be more efficient. The serration $h = (3/2)L_t$ achieves the maximum noise reduction at high frequencies.

Similarly, to study the effect of the spanwise wavelength, the amplitude is fixed to the value $h = (3/2)L_t$ with varying $\lambda$. The results are shown in figure 6.5(b). It can be seen that decreasing $\lambda$ to $L_t$ affects the noise reduction at high frequencies. The maximum efficiency is achieved for narrow serrations ($\lambda = (1/3)L_t$). The same observations are reported in [59]. Another fact to point out from this study is that at low frequencies, noise increase is predicted compared to the baseline configuration, due to the constructive interference effect at these frequencies. In summary, the serration wavelength has to be sufficiently small and the amplitude has to be large to have appreciable reduction with serrated leading edges.

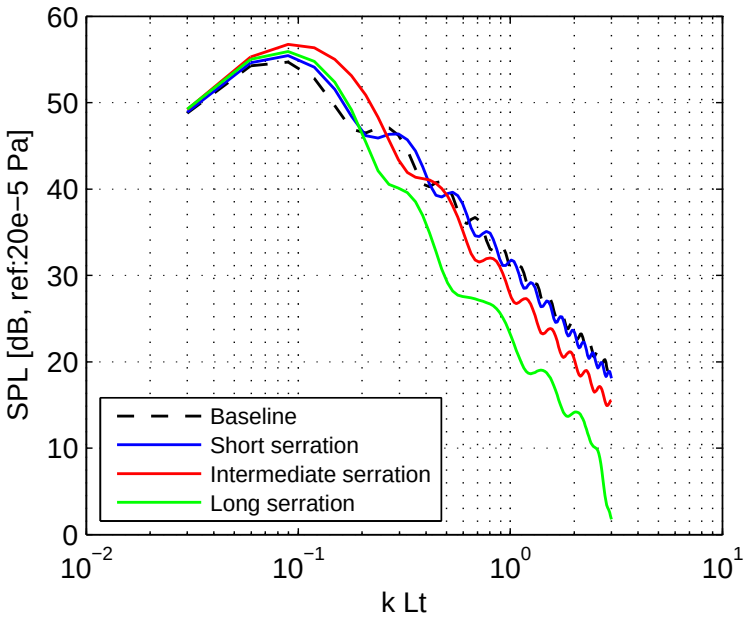


(a) Effect of varying h on sound spectrum while $\lambda = L_t$. Short serration: $h = (1/6)L_t$; Intermediate serration: $h = (1/2)L_t$; Long serration: $h = (3/2)L_t$.

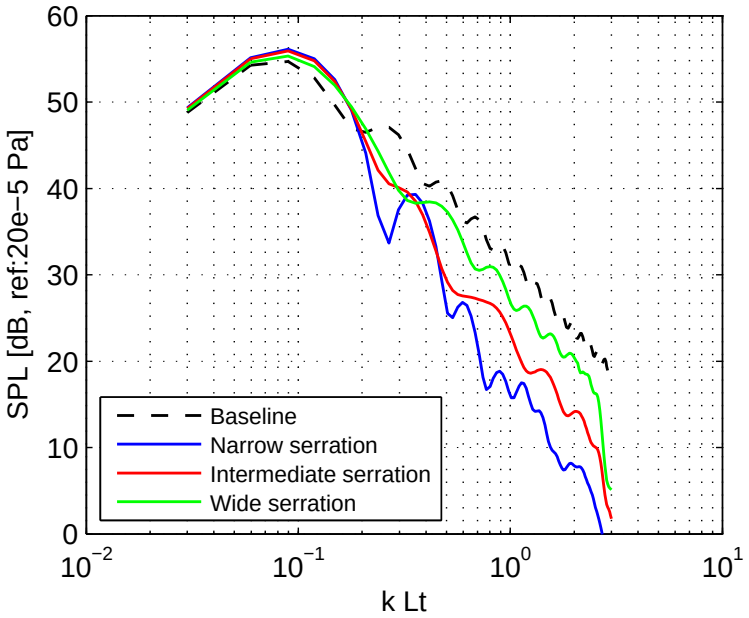


(b) Effect of varying $\lambda$ on sound spectrum while $h = (3/2)L_t$. Narrow serration: $\lambda = (1/3)L_t$; Intermediate serration: $\lambda = L_t$; Long serration: $h = 3L_t$.

Figure 6.5: Effects of varying h and $\lambda$ on far field spectrum using the serrated leading edge model

## 6.2 Extension of the single airfoil model to rotating blades

The same approach used to extend the analytical models for single airfoils to rotating blades, explained in section (2.7), is applied to predict the noise spectra emitted by the propellers with serrated leading edge presented in this section. The far field noise PSD for all propellers is calculated by averaging over all possible angular locations of the blade segments and by weighting with the Doppler factor (see section 2.7.1):

$$S_{pp}^{\Psi}(\vec{X},\omega) = \frac{B}{2\pi}\int_0^{2\pi}\left(\frac{\omega_e(\Psi)}{\omega}\right)^2 S_{pp}^{\Psi}(\vec{x},\omega_e)d\Psi \tag{6.31}$$

## 6.3 Model's assessment

The main results obtained from the use of the serrated leading edge model of Lyu et al. [58] on the propeller blades introduced in table 4.1 are presented in this section. First, the model is assessed by addressing the influence of the order approximation and the number of blade segments on the predicted solution. Next, the effect of the serration parameters on the leading edge noise and the leading edge component combined with the trailing edge component emitted by the propellers is discussed along with the effect of varying the flow conditions. The directivity patterns for different frequencies are also presented. All the spectra presented in this section are calculated for a receiver located at 1.5m from the propeller and placed at the angle $\theta = 90^o$. The Von Karman model for isotropic turbulence is used in the analytical model an integral length scale of turbulence $L_t = 0.001m$ and turbulent intensity $T_u = 0.1\%$.

Figure 6.6 compares the noise spectra emitted by the baseline blade predicted by the analytical models and the LBM simulations. The leading edge component using the analytical model of Lyu is predicted with the first order approximation, in the limit of no serrations (i.e. $\lim h/c \to 0$ and $\lim \lambda/h \to \infty$). When comparing the spectra combining the trailing edge and the leading edge noise, the results show that both Amiet's model, combined with the mean pressure gradient model for trailing edge noise, and Lyu's model predict the tendency and the SPL levels with a good precision at high

frequencies ($f > 1200Hz$) compared to the LBM spectrum. Although Amiet's model underestimates the leading edge noise spectrum compared to Lyu's model, the overall spectra predicted by the two models collapse at high frequencies when introducing the trailing edge noise component.

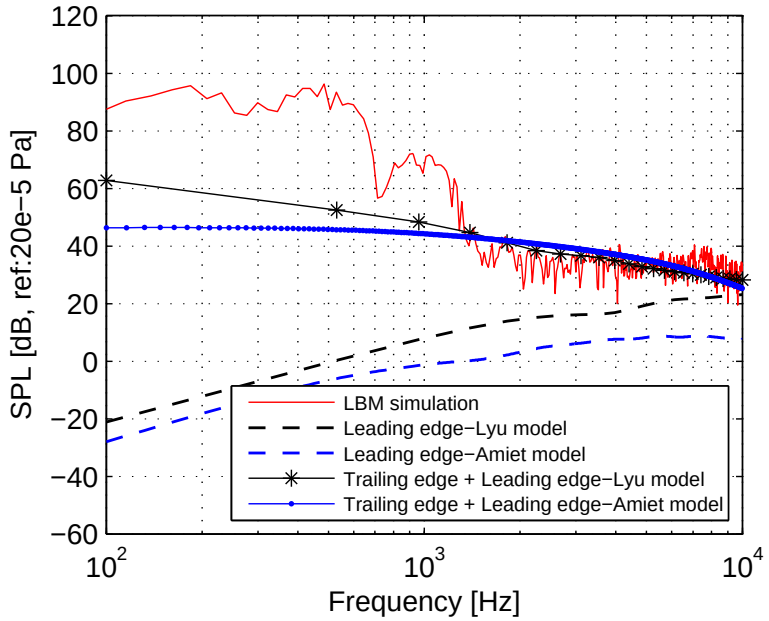


Figure 6.6: Noise spectra emitted by the baseline propeller.

Figure 6.7 presents the noise spectra emitted by the serrated leading edge blade $SLE7$. The analytical model for serrated leading edge proves to give a good approximation of the turbulence interaction noise spectrum which yields an overall spectrum that corresponds well with the LBM time-domain result at high frequencies, when introducing the trailing edge noise spectrum predicted by the same model.

### 6.3.1 Effect of the order approximation

The convergence rate of different order solutions is investigated by calculating the spectra using the zero and the $1^{st}$ order approximations for the straight blade (figure 6.8(a)) and the serrated leading edge blade $SLE5$ (figure 6.8(b)). The sum over $m$ and $n^{'}$ in equations (6.25a)-(6.25b), and (6.30) is truncated to m as indicated in the legends.

The results show that the predicted spectrum for the straight blade is not affected by

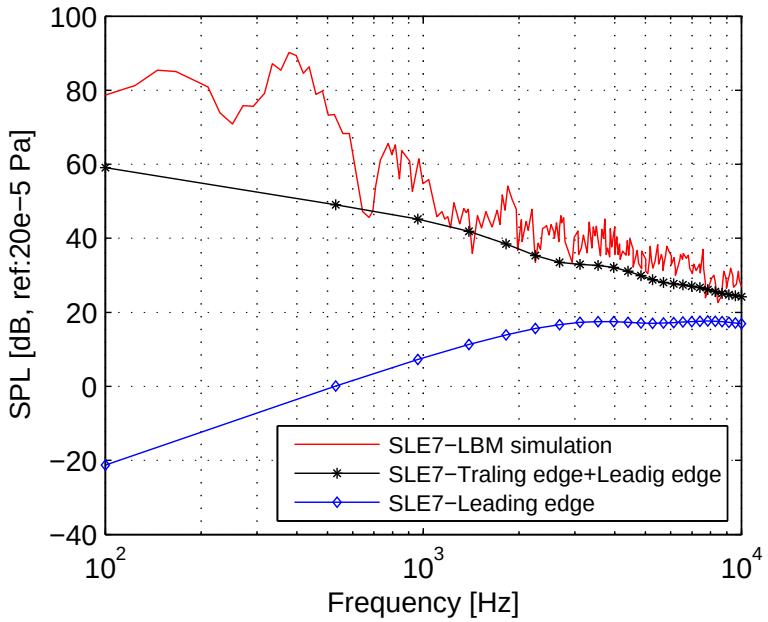


Figure 6.7: Noise spectra emitted by the $SLE7$ blade.

the approximation order. The same model applied to the serrated leading edge blade $SLE5$ show a difference between the $0^{th}$ and the $1^{st}$ order approximations of about $4dB$ at high frequencies. Furthermore, increasing the number of iterations when using the $1^{st}$ order approximation from $m = 30$ to $m = 70$ does not affect the accuracy of the solution but results in a considerable increase in computational time since it scales with $(2m + 1)^3$ as pointed by Fischer et al. [38].

### 6.3.2 Effect of the segments number

The influence of the segments number on the analytical solution is addressed in figure 6.9. Four tests are conducted with 3, 6, 9 and 12 segments on the SLE5 blade. The spectra are calculated using the $1^{st}$ order approximation with $m = 50$. It can be seen that the noise levels converge with the increasing number of segments in all frequency range. Furthermore, the difference between the SPL levels decreases from about $5dB$ between the spectra calculated with 3 and 6 strips to about $2dB$ between the spectra calculated with 9 and 12 strips at high frequencies. The overall difference between the spectra calculated with 3 and 12 strips reaches about $8dB$ at high frequencies. The predicted spectra show that the analytical model converge for a sufficiently large

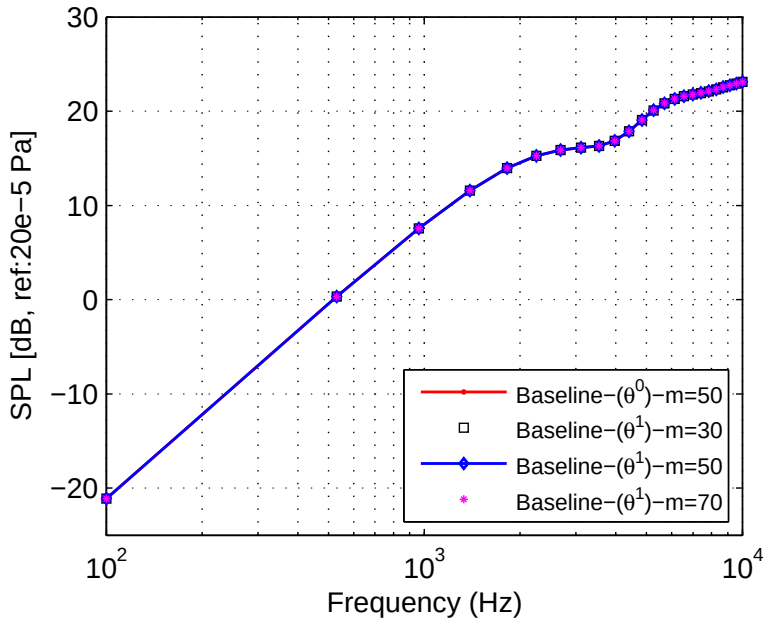


(a) Baseline propeller.

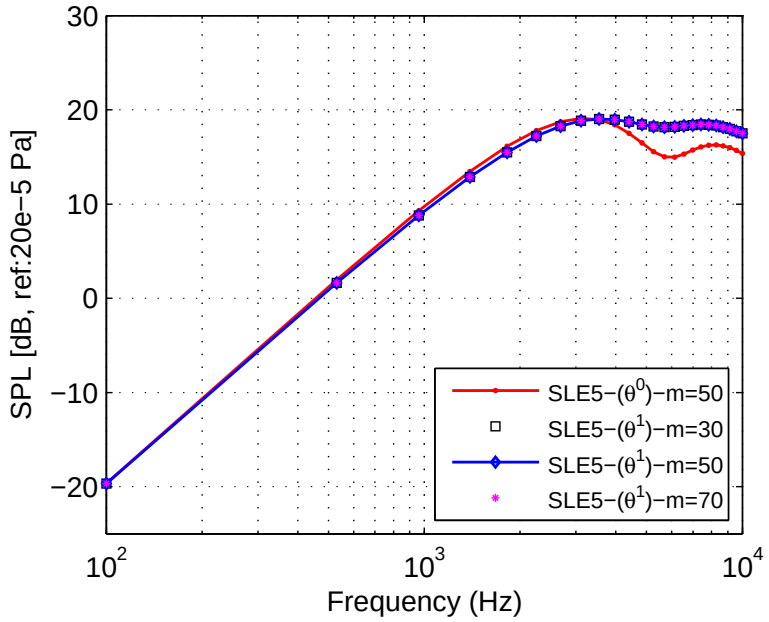


(b) $SLE5$ propeller.

Figure 6.8: Effect of the order approximation on the analytical results.

number of segments.

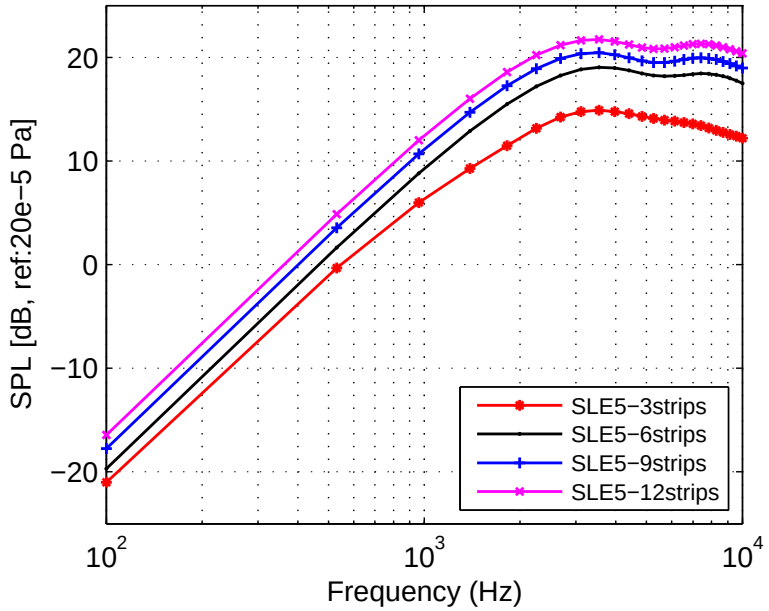


Figure 6.9: Effect of the segments number on the analytical results.

## 6.4 Effect of the serrations parameters

For the next analytical results, the $1^{st}$ order approximation is used to predict the SPL levels and the blade is divided into 6 segments to keep a balance between the precision of the solution and the computational cost.

The effect of varying the serration wavelength on the leading edge noise emitted by the serrated blades in comparison with the baseline propeller is shown in figure 6.10. All tested geometries increase noise in low to mid-frequency range, although turbulence interaction noise is weak in this range, and achieve a noise reduction above $5KHz$ where turbulence interaction noise is dominant. The serrated blades $SLE7$, $SLE5$ and $SLE12$ which have the same serration amplitude and decreasing serration wavelength present similar reduction magnitudes. The same trend is observed for the $SLE3$ and $SLE4$ serrated blades.

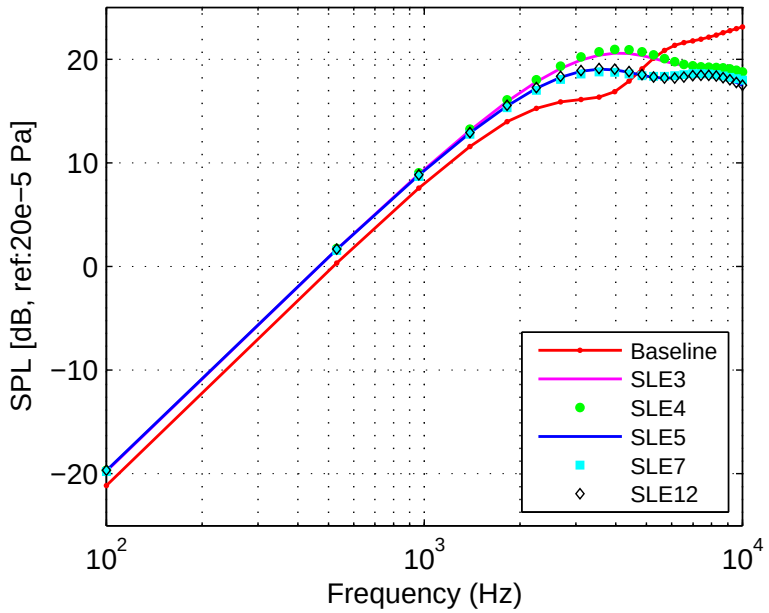


Figure 6.10: Effect of varying the serration wavelength.

To confirm this tendency, an investigation on the dependence of leading edge noise reduction as a function of the frequency is carried out. A representation of the noise reduction is $\Delta$SPL, which is the difference in SPL produced by the blades between the baseline and the serrated ones. Negative values of $\Delta$SPL denote noise reduction, while

positive values means that the serration produces higher noise level than the baseline case. Figure 6.11 presents the ΔSPL spectra with non dimensional frequency $f\lambda/U$ for the serrated blades of figure 6.10. It shows clearly that, although the sound reduction is of similar magnitude for a given serration amplitude, the curves fail to collapse, which translates the fact that the serration wavelength does not affect the magnitude of the noise reduction but it affects the frequency at which the reduction occurs.

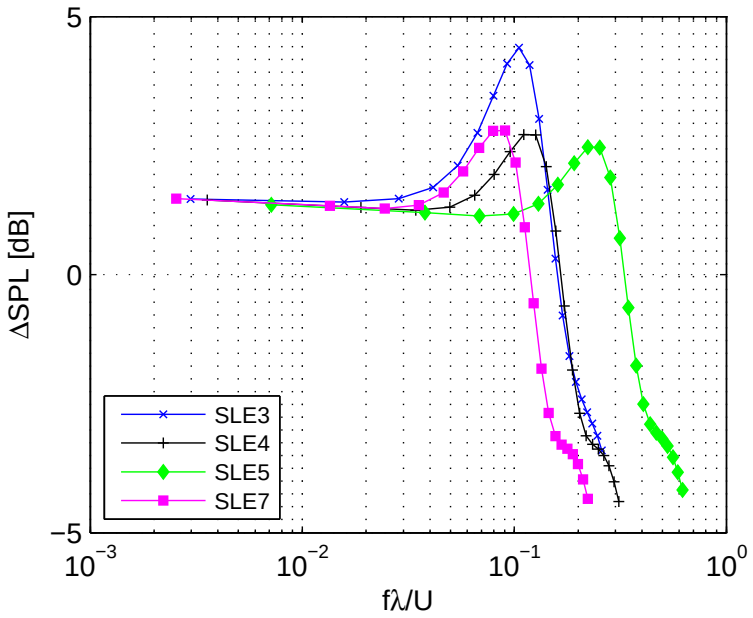


Figure 6.11: Variations in noise reduction.

Figure 6.12 depicts the influence of varying the serration amplitude on the leading edge noise emitted by the serrated propellers in comparison with the baseline blade. The results show that a noise reduction is achieved by increasing the serration amplitude. The predominent noise reduction is achieved by $SLE9$, which presents the highest serration amplitude, over a wider frequency range with a maximum reduction of about $10dB$ at high frequencies.

In summary, the spectra obtained for the serrated blades with different serration parameters show that the leading edge noise reduction is sensitive to the variation of the serration amplitude, while the serration wavelength does not seem to have a significant effect on it. High amplitudes come with noise reduction at high frequencies (above $1000Hz$). These observations agree well with the results presented by Narayanan et

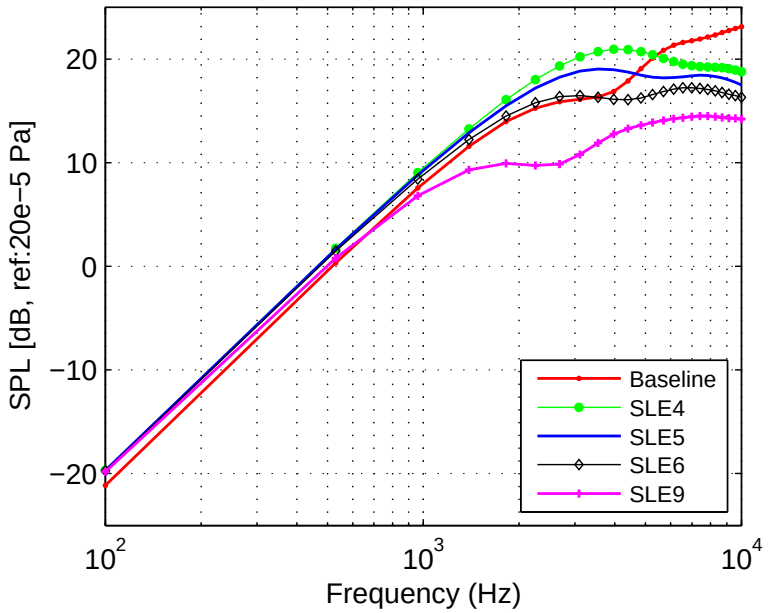


Figure 6.12: Effect of varying the serration amplitude.

al. [54, 121] and Chong et al. [122] for flat plates and airfoils in terms of variations with the serration amplitude and wavelength.

## 6.5 Effect of flow conditions

In order to assess the influence of the presence of leading edge serrations under varying advance ratios on the emitted noise levels, tests were conducted with the baseline and three serrated blades for different advance ratios. The serrated blades $SLE5$, $SLE7$ and $SLE9$ are selected to cover the effect of varying amplitudes and wavelengths with the variation of the advance ratio. From the results shown in figure 6.13 it can be seen that lower advance ratios, hence higher velocities on the blade, produce higher noise levels. For the advance ratio $J = 1.4$, for which the tip Mach number reaches 0.49, the spectra present the highest noise SPL levels for the baseline and the serrated blades. Moreover, no influence is observed on the trend of the spectra when varying the serrations parameters. These spectra show that the turbulence interaction noise is sensitive to the flow velocity as is found in Lyu et al. [58] and Narayanan et al. [54] for a flat plate and an isolated airfoil cases with different operating conditions.

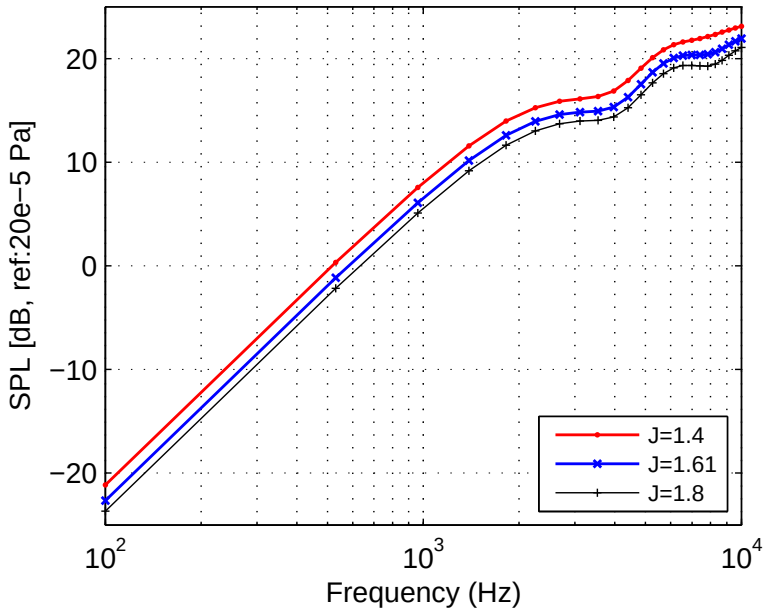


(a) Baseline propeller.

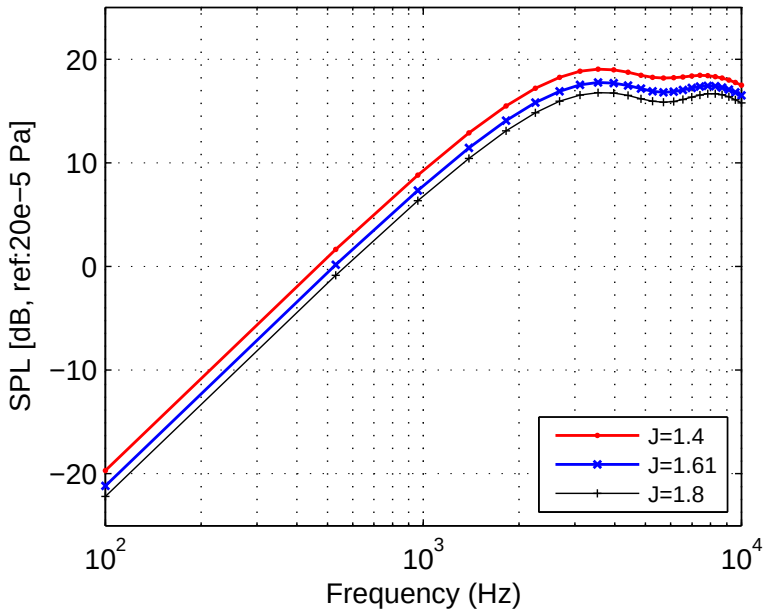


(b) $SLE5$ propeller.

Figure 6.13: Effect of varying the advance ratio on the turbulence interaction noise emitted by the baseline and $SLE5$ blades.

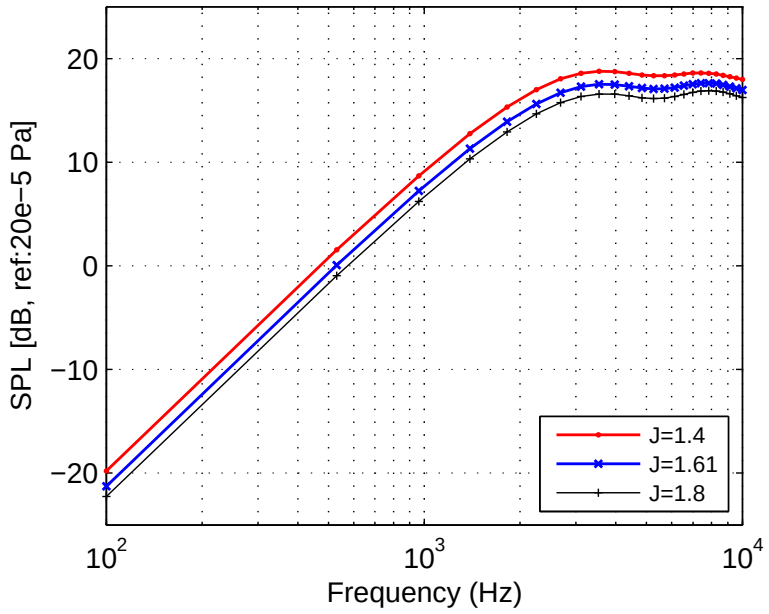


(a) $SLE7$ propeller.

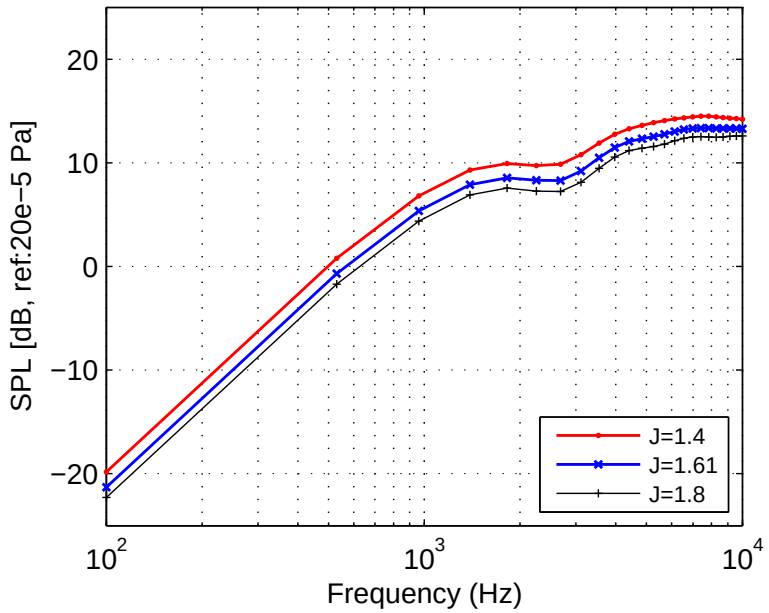


(b) $SLE9$ propeller.

Figure 6.14: Effect of varying the advance ratio on the turbulence interaction noise emitted by the $SLE7$ and $SLE9$ blades.

The same serrated blades were used to study the effect of turbulence intensity on the radiated turbulence interaction noise. Figure 6.15 presents the predicted SPL spectra for the serrated blades with varying turbulence intensity $Tu$. It is clear that the leading edge noise is highly sensitive to the turbulence intensity. An increase of about $20dB$ is observed when the turbulence intensity passes from 0.1% to 1%. Furthermore, the geometry of the serrated blades does not seem to affect the tendencies of the spectra.

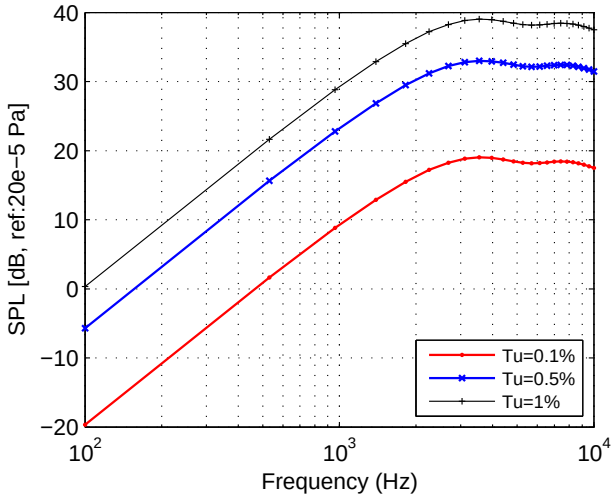


(a) $SLE5$ propeller.

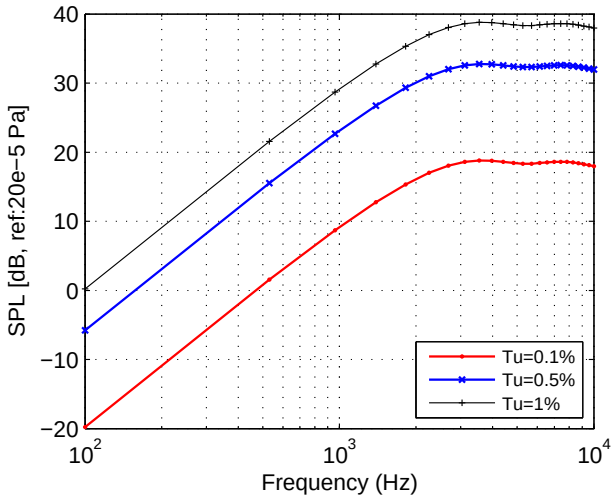


(b) $SLE7$ propeller.

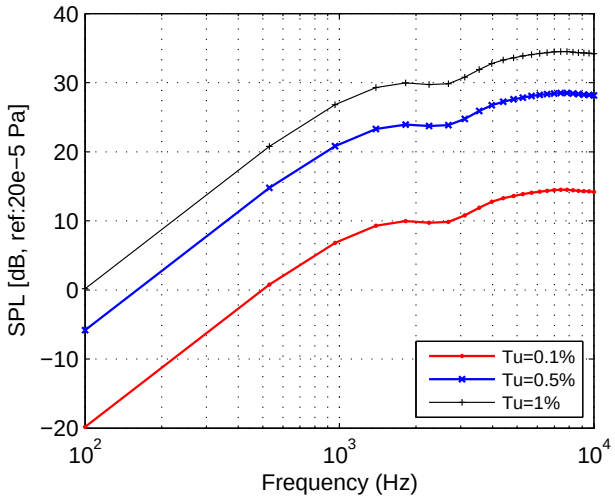


(c) $SLE9$ propeller.

Figure 6.15: Effect of varying the turbulence intensity on the turbulence interaction noise emitted by the blades.

## 6.6 Directivity patterns

Figures 6.16 and 6.17 show the sound pressure level directivity pattern, predicted by the analytical model, for the baseline and the serrated blades $SLE5$, $SLE6$ and $SLE9$ at different reduced frequencies $kc = 0.5, 2.8, 7.4, 12$ which correspond respectively to frequencies $f = 335Hz, 1.8kHz, 4.9kHz, 8kHz$.

At $kc = 0.5$, all the serrated geometries present a noise increase compared to the baseline blade at all angular positions. At mid range frequencies, $kc = 2.8$, $SLE9$ produces a noise reduction for all angular positions, while $SLE5$ and $SLE6$ present a different behaviour, noise reduction near the rotation axis and a noise increase elsewhere. At higher frequencies a noise reduction is observed with all serrated blades for all angular positions.

Overall, the results show that leading edge serrations reduce noise at high frequencies as discussed earlier, this can be explained by the destructive scattering interference effect [58]. Moreover, the leading edge serrations do not modify the directivity of the radiated trailing edge noise and their effect on the radiated noise is independent of the observer position. This was found to be the case at all studied frequencies whether a noise reduction occurs or not. The same result was pointed by Lyu et al. [58] for the sawtooth leading edge noise of a flat plate.

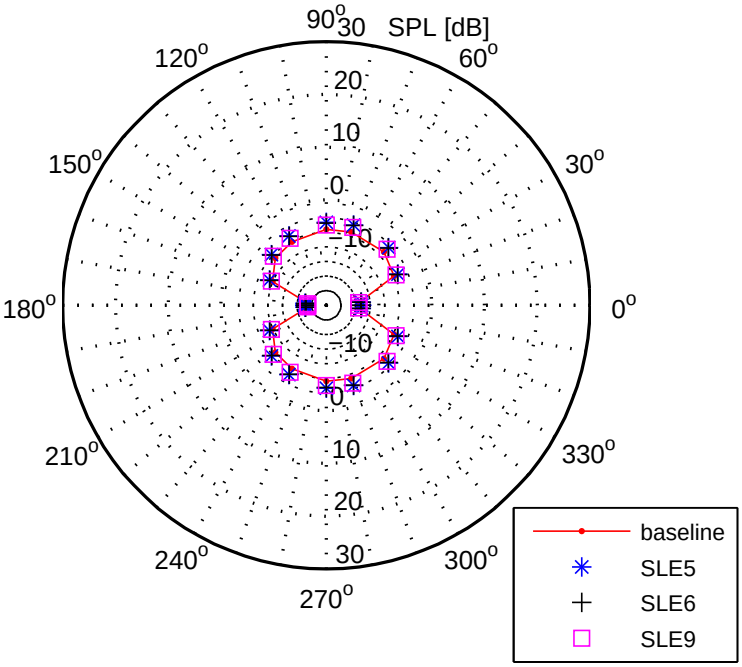


(a) $kc = 0.5$.

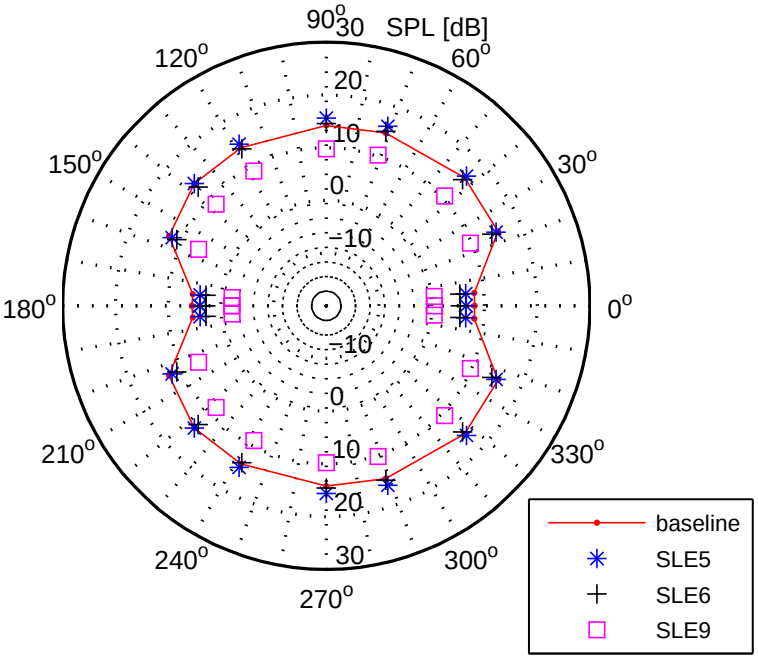


(b) $kc = 2.8$.

Figure 6.16: Leading edge noise directivity pattern for the baseline and leading edge serrated blades for $kc = 0.5$ and $kc = 2.8$.

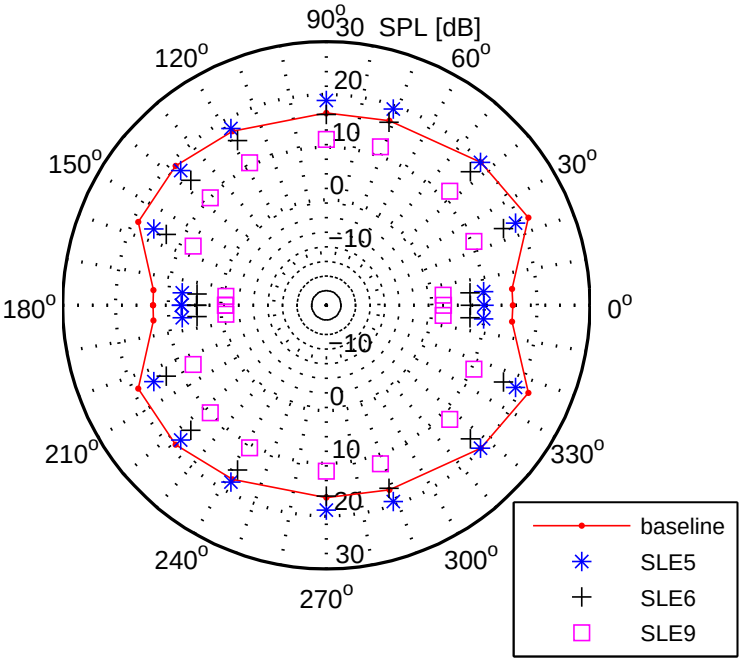


(a) $kc = 7.4$.

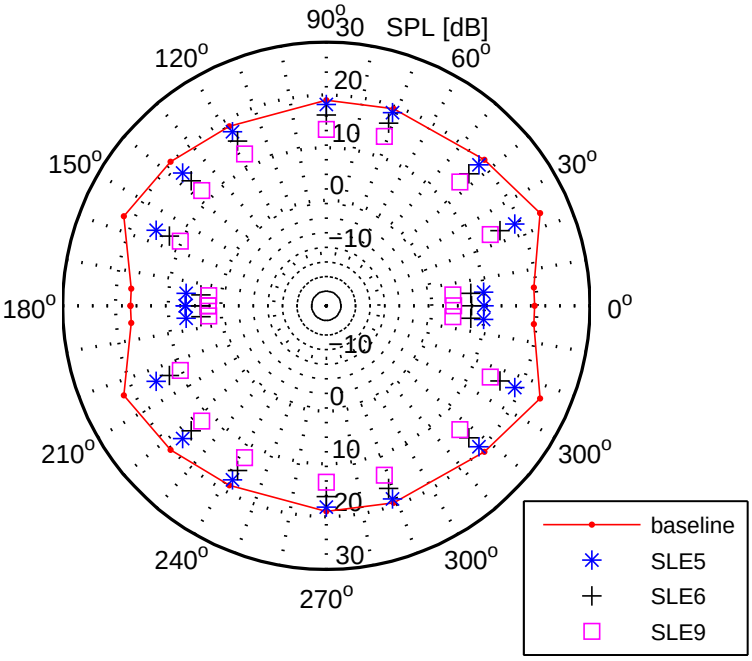


(b) $kc = 12$.

Figure 6.17: Leading edge noise directivity pattern for the baseline and leading edge serrated blades for $kc = 7.4$ and $kc = 12$.

## 6.7 Aerodynamic performance

In this section, the effect of the leading edge serrations on the flow around the baseline and $SLE4$, $SLE5$ and $SLE7$ blades is investigated. Results are extracted from the LBM simulations carried out for $J = 1.4$. The pressure and the skin friction coefficients distributions are evaluated along the blade chord at four spanwise locations: 25%, 50%, 75% and 95% for the nearest peak and valley as shown in figure 6.18.

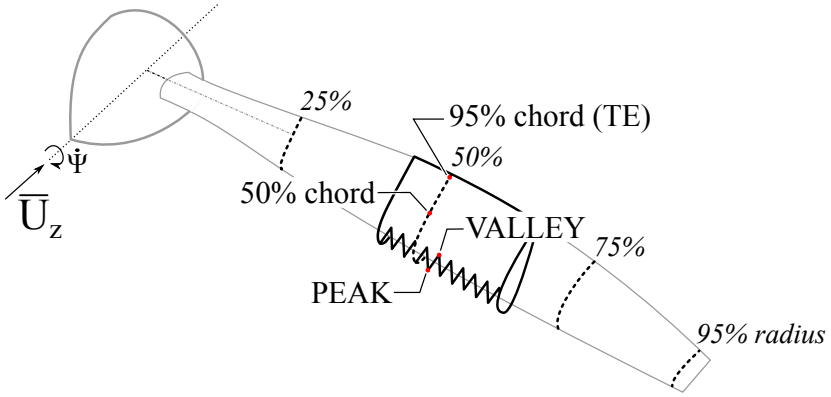


Figure 6.18: Chordwise and spanwise positions for the evaluation of the local flow features.

### 6.7.1 Pressure and skin friction coefficients

The static pressure coefficient $C_p$ and the skin friction coefficient $C_f$ are plotted in figures 6.19 and 6.20. For the baseline blade, at 25% span, the flow remains attached over the entire blade chord as can be seen in figures 6.19(a) and 6.20(a). At 50% span, the pressure distribution on the suction side (figure 6.19(b)) bears the trace of a separation bubble taking place at the leading edge, this is also confirmed by the sudden variation of the skin friction coefficient near the leading edge in figure 6.20(b). Starting from 75% span, a strong vortex attached to the leading edge appears, caused by the geometry of this latter (small radius) and the presence of a sweep [116], it becomes stronger in the spanwise direction and merges with the propeller tip vortex near the tip affecting strongly the pressure coefficient (figures 6.19(c), 6.19(d)) and skin friction coefficient (figures 6.21(d), 6.21(b)) distributions. On the pressure side, a plateau seen from 20% to 80% chord which is identified with a thin recirculation

bubble [123]. It extends all along the spanwise direction. These results are in good qualitative agreement with the experiments of Schulein et al. [124] in term of flow topology at the same advance ratio.

For the serrated blades, it can be seen that the pressure and the skin friction distributions are strongly affected near the peak of the serration on both the pressure and the suction sides. This can be explained by the fact that the peak is the first point of contact of the airfoil with a particular turbulence eddy [60]. At 50% span, a hump of pressure is observed at 0.2 chord on both the pressure and suction sides of the peak (figures 6.19(b)). This latter indicates the presence of a separation also evidenced by the skin friction coefficient at the same location as seen in figure 6.20(b). The separation zone extends in the spanwise direction until the tip. On the pressure side, the topology remains the same, however it changes appreciably on the suction side. The $SLE7$ blade exhibits a strong separation while the $SLE4$ and $SLE5$ blades, which have the same wavelength and different amplitudes, show a reattachment and another separation at approximately 0.7 chord (figure 6.19(c), 6.19(d), 6.21(d), 6.21(b)). These findings agree well with the dye injection visualisations performed by Chong et al. [122] who found that the dye remains attached to the serration peak but suddenly undergoes a splitting process at some points downstream. After the splitting, most of the dye converges to the adjacent serration valleys. Behind each valley, a large cigar-shaped turbulence structure was found to form which explains the high pressures observed near the valleys for the serrated blades. Near the tip, in the same location, the $SLE4$ and $SLE5$ blades show a reattachment on the suction side where the flow is also affected by the tip vortex.

### 6.7.2 Vorticity

For the serrated leading edge blades, peaks come comparatively with lower vorticity values than the baseline except for the region in the immediate vicinity of the trailing edge (figure 6.21). Valleys cause strong vorticity downstream of the leading edge along the suction side wall in the streak to about 50% chord which is a remain of the baseline leading edge vortex.

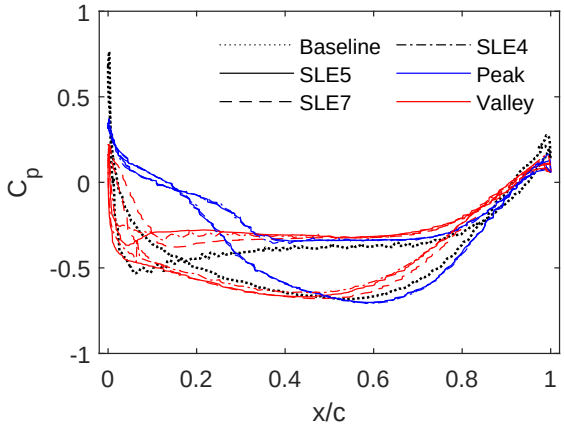


(a) $C_p$ – 25% radius.

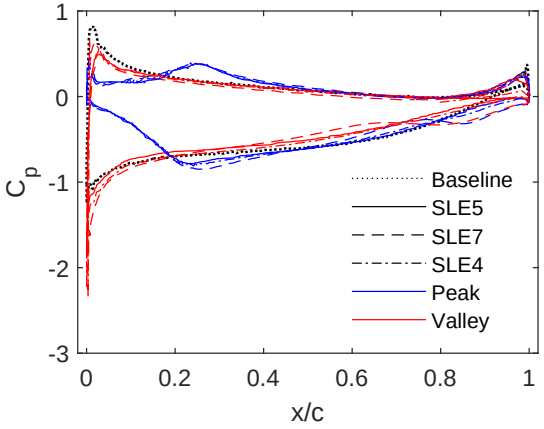


(b) $C_p$ – 50% radius.

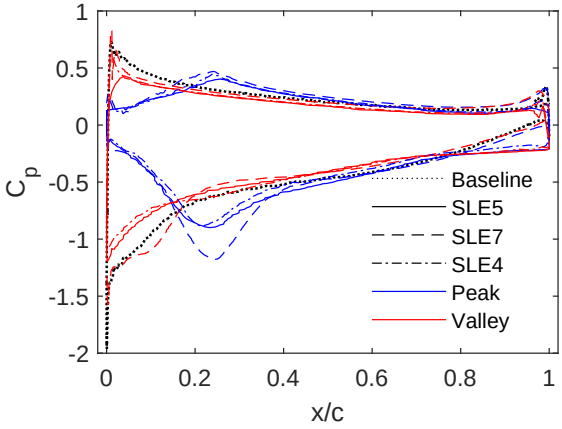


(c) $C_p$ – 75% radius.

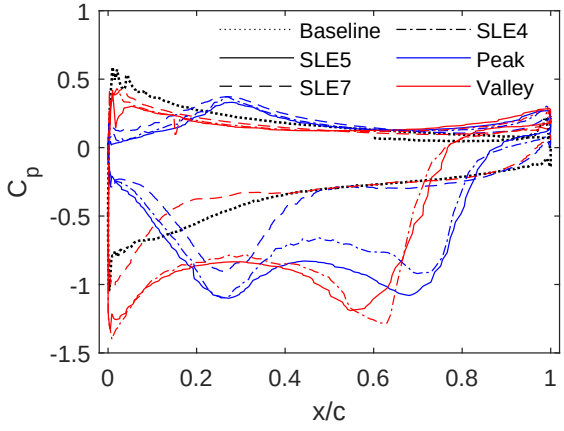


(d) $C_p$ – 95% radius.

Figure 6.19: Pressure coefficient distribution at different spanwise locations for the serrated leading edge blades.

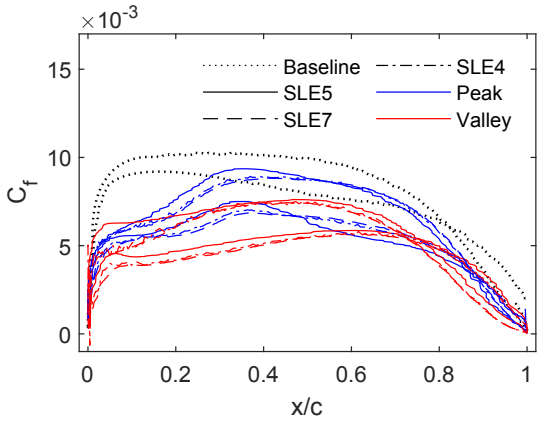


(a) $C_f$ – 25% radius.

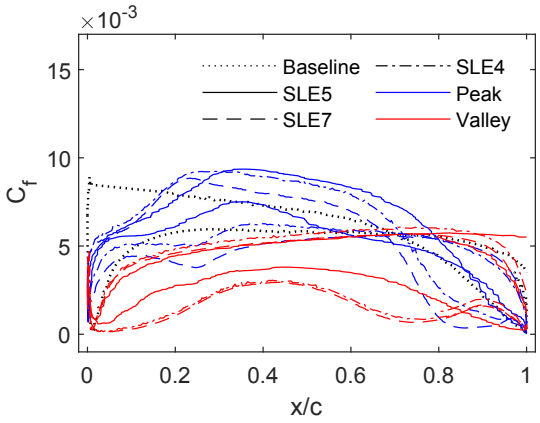


(b) $C_f$ – 50% radius.

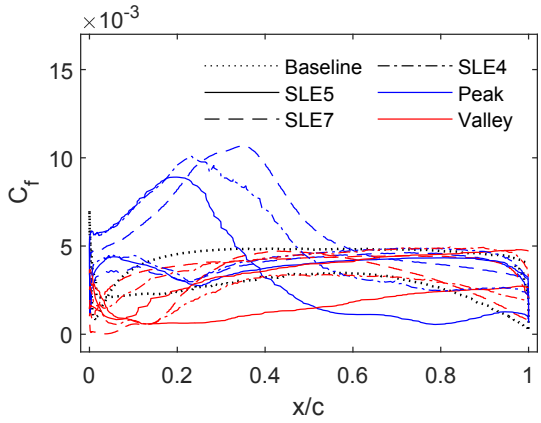


(c) $C_f$ – 75% radius.

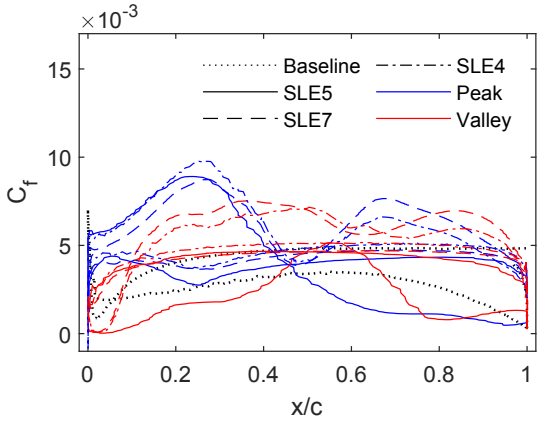


(d) $C_f$ – 95% radius.

Figure 6.20: Skin friction coefficient distribution at different spanwise locations for the serrated leading edge blades.

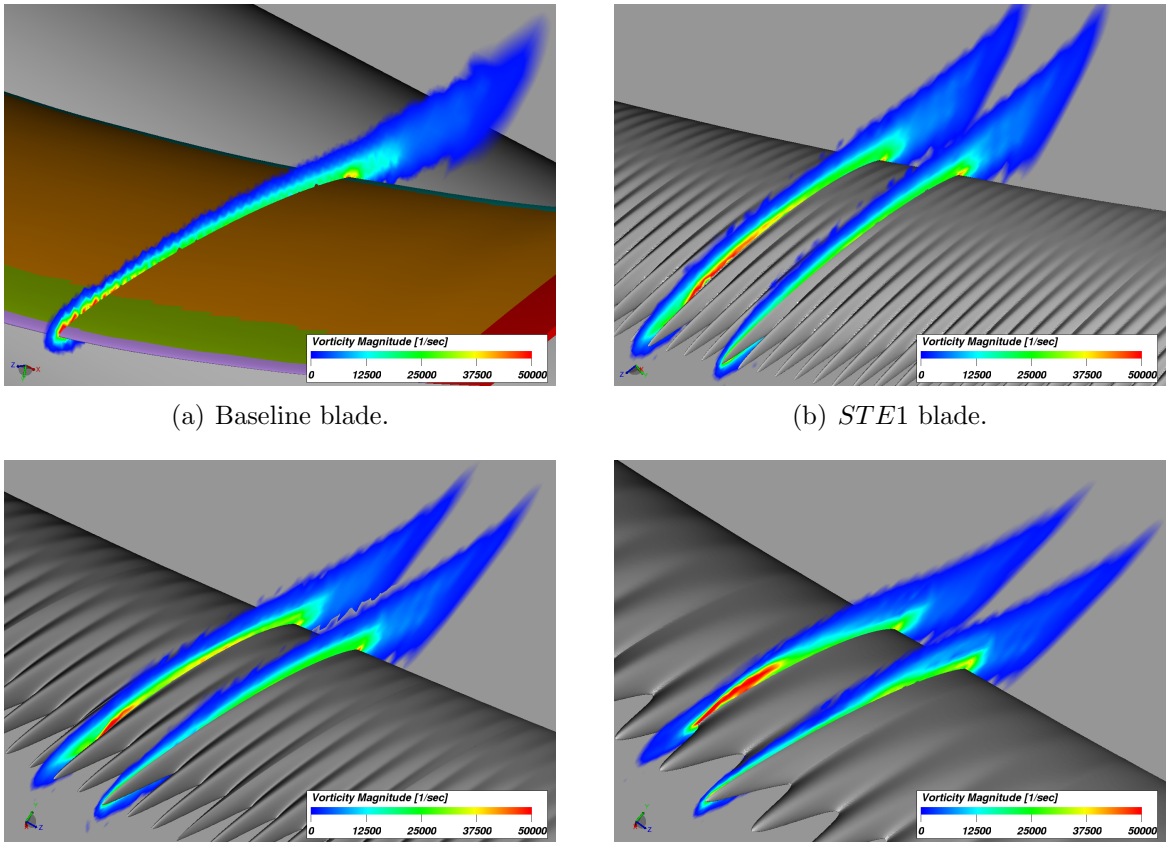


(a) Baseline blade.

(b) $STE1$ blade.

(c) $STE3$ blade.

(d) $STE4$ blade.

Figure 6.21: Vorticity contours around 75% radius for the baseline and the serrated leading edge blades.

Preliminary results from inspecting the local features of the flow around the baseline and the leading edge serrated blades show that the serrations affect greatly the flow structure around the blades as found by Wang et al. [62] and Chong et al. [122]. It is found that the most protrude part of the serration, which is the peak, interacts with the incoming flow which undergoes a splitting process. The remaining part of the flow merges at the valleys forming strong turbulent structures. This flow dynamics may be responsible for the noise reduction. Further investigations are needed to describe properly the mechanisms behind the turbulence interaction noise reduction and to analyse the effect of serration parameters on this latter.

### 6.7.3 Overall performance

Differences in aerodynamic performance for serrated leading edge blades are more pronounced than when comparing serrated trailing edge geometries. The $SLE5$ and $SLE7$ geometries outperform the baseline blade in terms of thrust, unfortunately also in terms of power so that efficiency is similar to that of the baseline. These blades do not perform as well as the baseline at lower rpm although the $SLE5$ offers interesting characteristics when looked at in the constant thrust perspective since it has a higher efficiency than the baseline as shown in figure 6.22.

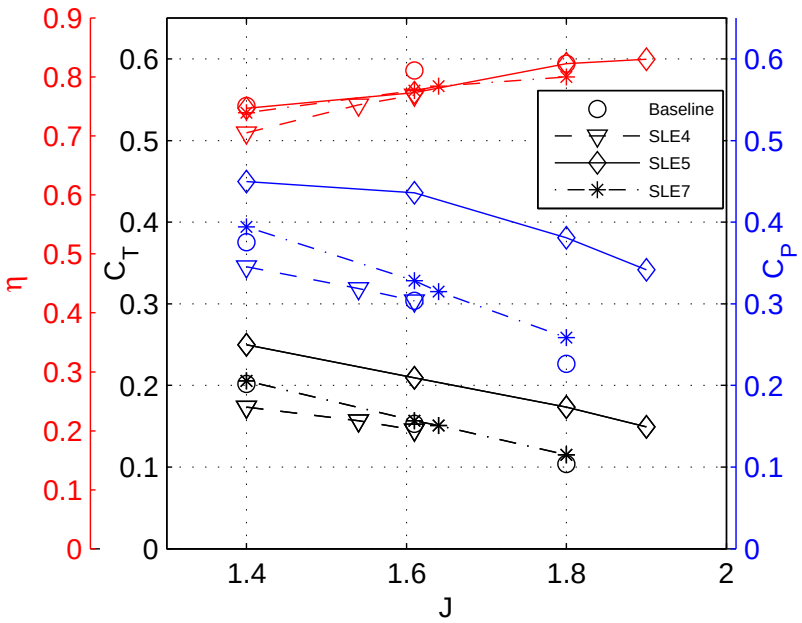


Figure 6.22: Aerodynamic performance for the leading edge serrated blades.

## 6.8 Conclusion

This chapter assesses the potential of leading edge noise reduction by applying sawtooth leading edge serrations on a propeller. Different serrations parameters are tested using Lyu's analytical frequency-domain model and compared to LBM time-domain simulations performed for the same serrated geometries.

The comparison of the spectra combining the trailing edge and the leading edge noise shows that both Amiet's model, combined with the mean pressure gradient model for trailing edge noise, and Lyu's model predict the tendency and the SPL levels with a good precision at high frequencies compared to the LBM spectrum.

A study was conducted to assess Lyu's model, it was found that the zero-order approximation is computationally relatively cheap and is able to capture relative variations but comes with a loss of accuracy, while the first-order approximation is more expensive in computational time but gives more accurate results. The number of segments affects the analytical solution which seems to converge for a large number of segments. Further investigations are needed to determine the limit of convergence with increasing the segments number since the computational cost scales directly with the number of

segments.

The results of the parametric study conducted with sawtooth leading edge serrated blades show that the use of serrations reduces the noise emitted by the propellers at high frequencies. The noise reduction increases with the increased serration amplitude, while the variation of serration wavelength show no significant effect on the noise reduction. Moreover, the leading edge noise reduction is sensitive to flow conditions, it was found to be an increasing function of both increasing advance ratio and turbulence intensity. The turbulence length scale is found to be an important factor which determines the noise reduction from serrated leading edges.

The inspection of the skin and pressure coefficients around the serrated blades shows that the flow is highly affected by the introduction of the serrations. The serrated blades come with increased thrust and power at constant advance ratio, but not with better efficiency.

# *Conclusions*

# Conclusions

This thesis presents, for the first time, an analytical and numerical study aimed at computing the broadband noise spectrum of a mini-RPA propeller in order to assess the potential of noise reduction when applying sawtooth serrations on its edges. The serration are obtained by modifying the spanwise distribution of chord and thickness which results in the existence of streamwise streaks into both sides of the blade. Recent frequency-domain analytical models for predicting noise from airfoils with serrated edges were implemented and applied to the propellers using a strip approach. The blade is divided into a number of spanwise segments for which the corresponding mean flow and boundary layer quantities are computed from a CFD solution. The models were assessed by comparison with time-domain LBM simulations.

The obtained results show that the analytical models are able to predict the noise from propellers with either straight or serrated trailing edge/leading edge. Moreover, the investigation of the convergence rate of the zero and first order solutions shows that the zero order approximation is computationally relatively cheap and is able to capture relative variations. The first order approximation is more expensive in computational time but gives more accurate results. The number of segments affects the analytical solution which seems to converge for a large number of segments. Further investigations are needed to determine the limit of convergence with increasing the segments number since the computational cost scales directly with the number of segments.

A parametric analytical study was conducted to investigate the effects of serrations on propellers featuring sawtooth serrations of varying amplitude and wavelength either at the leading edge or at the trailing edge. In parallel, the results of the Lattice Boltzmann unsteady simulations were used to investigate the pressure and skin friction distribution around the propeller blades and evaluate their performance.

For the the serrated trailing edge geometries:

– The use of serrations reduces the noise emitted by the propellers at low to mid frequencies but induces a noise increase at high frequencies. The sharpest serrations were found to achieve the better performance in terms of reducing noise. This result is identical to what was found for non-rotating airfoils by several authors [38, 43],

though it is here extended to the case of rotating airfoils hence with the occurrence of cross-flow and spanwise varying flow conditions as pointed by Oerlemans et al. [40];

– The serrations have an in influence upstream of their location due to the presence of the streamwise streaks stemming from the local variations in chord and thickness. Doing so, the area enclosed by the pressure distribution near a peak is decreased when compared to the baseline (less loading) whereas it is increased near valleys (more loading). Nevertheless, the leading edge vortex present along the span of the baseline and $STE$ blades is not impacted by the presence of downstream serrations;
– Large serrations of small wavelength are favourable in terms of $C_f$ which is lower thanks to the streamwise streaks; The thrust and power performance are highly influenced by the serration geometry even though the efficiency is not impacted.

For the serrated leading edge geometries:

– The serrations are effective in reducing the noise emitted by the propellers at high frequencies. The noise reduction increases with the increased serration amplitude, while the variation of serration wavelength show no significant effect on the noise reduction;
– The turbulence interaction noise is sensitive to flow conditions, it was found to be an increasing function of both increasing advance ratio (decreasing rotational speed) and turbulence intensity;
– The flow over the baseline blade is highly affected by the introduction of serrations. It is found that the incoming flow interacts with the peak and undergoes a splitting process with which the remaining part of the flow merges behind the valleys forming strong turbulent structures. This flow dynamics is believed to be responsible for the turbulence interaction noise reduction;
– The serrated blades come with increased thrust and power at constant advance ratio, but not with better efficiency.

An important result comes out from this study which outcomes show that the analytical models (Amiet's model for the baseline blade and Lyu's model for the serrated blades) combined with appropriate CFD-RANS results are capable of predicting emitted broadband noise from propellers with a good precision despite the assumptions used

to develop them. This is promising, since these models are particularly useful in the design stages of propellers or complete aircraft because they are relatively computationally cheap. An other point is that when comparing the results, it is clear that trailing edge serrations are more effective in reducing the overall broadband noise emitted by the blades over a larger frequency band compared to the leading edge serrations.
A question arises about what is the best solution to adopt to reduce noise from propellers: decreasing the rotational speed or using serrations? The answer is: it is a question of making compromises. Decreasing velocity comes with a noise reduction but a loss in aerodynamic performance. While serrations keep a good aerodynamic balance with reduction of noise at higher velocities.

## Recommendations for future work

Recommendations and suggestions for future work are listed below:

- Implementation of the second order approximation of the analytical model to assess its influence on the predicted spectra;
- Detailed investigation of quantitative parameters of the flow field around the blades such as the lift and drag coefficients, the rms of surface pressure fluctuations, the development of boundary layer... and the exploration of the propellers near wake are necessary to clarify the mechanisms by which noise is reduced;
- Development of prediction methods for other sources of broadband noise in propellers, such as the turbulent tip-vortex interaction noise and the pylon-wake/rotor interaction noise. The relative importance of these additional sources of broadband noise in propellers compared to the self noise and the turbulence interaction noise sources could then be studied;
- Design and test novel serrations geometries such as slitted or combed serrations on propellers blades.

# *Bibliography*

# Bibliography

[1] B. Magliozzi, D. Hanson, and R. Amiet, "Propeller and propfan noise," *NASA, Langley Research Center, Aeroacoustics of Flight Vehicles: Theory and Practice*, vol. 1, pp. 1–64, 1991.

[2] "Introduction of a regulatory framework for the operation of unmanned aircraft systems in the open and specific categories," Tech. Rep. Opinion No 01/2018, European Aviation Safety Agency, 2018.

[3] C. J. Doolan, D. J. Moreau, and L. A. Brooks, "Wind turbine noise mechanisms and some concepts for its control.," *Acoustics Australia*, vol. 40, no. 1, 2012.

[4] Y. Wang, K. Zhao, X.-Y. Lu, Y.-B. Song, and G. J. Bennett, "Bio-inspired aerodynamic noise control: a bibliographic review," *Applied Sciences*, vol. 9, no. 11, p. 2224, 2019.

[5] C. N. Adkins and R. H. Liebeck, "Design of optimum propellers," *Journal of Propulsion and Power*, vol. 10, no. 5, pp. 676–682, 1994.

[6] A. Leslie, K. C. Wong, and D. Auld, "Broadband noise reduction on a mini-uav propeller," in *14th AIAA/CEAS Aeroacoustics Conference (29th AIAA Aeroacoustics Conference)*, p. 3069, 2008.

[7] M. Roger, C. Schram, and L. D. Santana, "Reduction of airfoil turbulence-impingement noise by means of leading-edge serrations and/or porous material," in *19th AIAA/CEAS aeroacoustics conference*, p. 2108, 2013.

[8] T. Bachmann, S. Klän, W. Baumgarner, M. Klaas, w. Schröder, and H. Wagner, "Morphometric characterisation of wing feathers of the barn owl tyto alba pratincola and the pigeon columba livia," *Frontiers in zoology*, vol. 4:23, 2007.

[9] R. A. Kroeger, "Low speed aerodynamics for ultra-quiet flight," tech. rep., DTIC document, 1972.

[10] G. M. Lilley, "A study of the silent flight of the owl," in *4th AIAA/CEAS Aeroacoustics conference*, no. AIAA 1998-2340, 1998.

[11] H. Johari, C. Henoch, D. Custodio, and A. Levshin, "Effect of leading edge protuberances on airfoil performance," *AIAA Journal*, vol. 45, no. 11, pp. 2634–2642, 2007.

[12] M. S. Howe, "A review of the theory of trailing edge noise," Contractor Report 3021, NASA, June 1978.

[13] R. K. Amiet, "Noise due to turbulent flow past a trailing edge," *Journal of sound and vibration*, vol. 47, no. 3, pp. 387–393, 1976.

[14] M. S. Howe, "Trailing edge noise at low mach numbers," *Journal of Sound and Vibration*, vol. 225, pp. 211–238, September 1999.

[15] M. S. Howe, "Trailing edge noise at low mach numbers, part 2: attached and separated edge flows," *Journal of Sound and Vibration*, vol. 234, no. 5, pp. 761–775, 2000.

[16] R. K. Amiet, "Noise produced by turbulent flow into a propeller or helicopter rotor," *AIAA journal*, vol. 15, pp. 307–308, March 1977.

[17] R. W. Paterson and R. K. Amiet, "Noise of a model helicopter rotor due to ingestion of turbulence," Contractor Report 3213, NASA, November 1979.

[18] R. H. Schlinker and R. K. Amiet, "Helicopter rotor trailing edge noise," Contractor Report 3470, NASA, 1981.

[19] S. A. L. Glegg, S. M. Baxter, and A. G. Glendinning, "The prediction of broadband noise from wind turbines," *Journal of sound and vibration*, vol. 118, no. 2, pp. 217–239, 1987.

[20] V. P. Blandeau and Phill, "Validity of amiet's model for propeller trailing edge noise," *AIAA Journal*, vol. 49, no. 5, pp. 1057–1065, 2011.

[21] S. Sinayoko, M. Kingan, and A. Agarwal, "Trailing edge noise theory for rotating blades in uniform flow," *Proceeding of Royal Society*, pp. 1–28, June, 11 2013.

[22] M. Roger and S. Moreau, "Back-scattering correction and further extensions of amiet's trailing-edge noise model. part i: theory," *Journal of Sound and Vibration*, vol. 286, pp. 477–506, 2005.

[23] M. Roger and S. Moreau, "Back-scattering correction and further extensions of amiet's trailing-edge noise model. part ii: Application," *Journal of Sound and Vibration*, vol. 323, pp. 397–425, 2009.

[24] Y. Rozenberg, M. Moreau, A. Gu'edel, and S. Moreau, "Rotating blade self noise: experimental validation of analytical models," in *13th AIAA/CEAS Aeroacoustics conference (28th AIAA aeroacoustics conference)*, no. AIAA 2007-3709, (Rome, Italy), May 21-23 2007.

[25] Y. Rozenberg, M. Roger, and S. Moreau, "Rotating blade trailing edge noise: Experimental validation of analytical model," *AIAA journal*, vol. 48, pp. 951–962, May 2010.

[26] A. Pagano, M. Barbarino, D. Casalino, and Luigi, "Tonal and broadband noise calculations for aaeroacoustic optimization of propeller blades in a pusher configuration," in *15th AIAA/CEAS aeroacoustics conference (30th AIAA Aeroacoustics conference)*, no. AIAA 2009-3138, (Miami, Florida), May 11-13 2009.

[27] T. F. Brooks and T. H. Hudgson, "Trailing edge noise prediction from measured surface pressures," *Journal of Sound and Vibration*, vol. 78, no. 1, pp. 69–117, 1981.

[28] M. Wang and P. Moin, "Computation of trailing-edge flow and noise using large-eddy simulation," *AIAA journal*, vol. 38, no. 12, pp. 2201–2209, 2000.

[29] M. Goody, "Empirical spectral model of surface pressure fluctuations," *AIAA journal*, vol. 42, no. 9, pp. 1788–1794, 2004.

[30] Y. Rozenberg, G. Robert, and S. Moreau, "Wall pressure sspectra model including the adverse pressure gradient effects," *AIAA journal*, vol. 50, pp. 2168–2179, October 2012.

[31] M. S. Howe, "Noise produced by a sawtooth trailing edge," *Journal of the Acoustical Society of America*, vol. 90, pp. 482–487, july 1991.

[32] M. S. Howe, "Aerodynamic noise of a serrated trailing edge," *Journal of Fluids and Structures*, no. 5, pp. 33–45, 1991.

[33] M. Azarpeyvand, M. Gruber, and P. F. Joseph, "An analytical investigation of trailing edge noise reduction using novel serrations," in *19th AIAA/CEAS Aeroacoustics Conference*, no. AIAA 2013-2009, (Berlin, Germany), May, 27-29 2013.

[34] L. E. Jones and R. D. Sandberg, "Numerical investigation of airfoil self-noise reduction by addition of trailing-edge serrations," in *16th AIAA/CEAS aeroacoustics conference*, no. 2010-3703, 2010.

[35] M. Gruber, *Airfoil noise reduction by edge treatments*. PhD thesis, University of Southampton, February 2012.

[36] D. J. Moreau and C. J. Doolan, "Noise reduction mechanism of a flat plate serrated trailing edge," *AIAA journal*, vol. 51, pp. 2513–2522, October 2013.

[37] B. Lyu, M. Azarpeyvand, and S. Sinayoko, "Prediction of noise from serrated trailing edges," *Journal of Fluid Mechanics*, vol. 793, pp. 556–588, 2016.

[38] A. Fischer, F. Bertagnolio, W. Z. Chen, and J. Madsen, "Noise model for serrated trailing edges compared to wind tunnel measurements," *Journal of Physics*, vol. Conference Series 753 (2016), no. 022053, pp. 1–9, 2016.

[39] T. Dassen, R. Parchen, J. Bruggeman, and F. Hagg, "Results of a wind tunnel study on the reduction of airfoil self-noise by the application of serrated blade trailing edges," Tech. Rep. NLR TP 96350 U, National Aerospace Laboratory NLR, 1996.

[40] S. Oerlemans, M. Fisher, T. Maeder, and K. Kögler, "Reduction of wind turbine noise using optimized aairfoil and trailing edge serrations.," *AIAA Journal*, vol. 47, pp. 1470–1481, June 2009.

[41] S. Sinayoko, M. Azarpeyvand, and B. Lyu, "Trailing edge noise prediction for rotating serrated blades," in *20th AIAA/CEAS Aeroacoustics Conference*, no. AIAA 2014-3296, (Atlanta, GA), June, 16-20 2014.

[42] M. Gruber, P. F. Joseph, and T. P. Chong, "On the mechanisms of serrated airfoil trailing edge noise reduction," in *17th AIAA/CEAS Aeroacoustics conference*, no. AIAA 2011-2781, (Portland, Oregon), June, 5-8 2011.

[43] M. Gruber, P. F. Joseph, and T. P. Chong, "Experimental investigation of airfoil self noise and turbulent wake reduction by the use of trailing edge serrations," in *16th AIAA/CEAS Aeroacoustics conference*, no. AIAA 2010-3803, (Stockholm, Sweden), June 8-10 2010.

[44] A. Vathylakis and T. P. Chong, "On the turbulent boundary layers developed on flat plate with a serrated trailing edge," in *19th AIAA/CEAS Aeroacoustics Conference*, p. 2107, 2013.

[45] T. P. Chong and A. Vathylakis, "On the aeroacoustic and flow structures developed on a flat plate with a serrated sawtooth trailing edge," *Journal of Sound and Vibration*, vol. 354, pp. 65–90, 2015.

[46] R. Y. Myose and J. Iwata, "Flow visualization of an oscillating airfoil with sawtooth trailing edge," *AIAA journal*, vol. 34, no. 8, pp. 1748–1750, 1996.

[47] W. R. Sears, "Some aspects of non-stationary airfoil theory and its practical application," *Journal of the Aeronautical Sciences*, vol. 8, no. 3, pp. 104–108, 1941.

[48] J. Graham, "Similarity rules for thin aerofoils in non-stationary subsonic flows," *Journal of Fluid Mechanics*, vol. 43, no. 4, pp. 753–766, 1970.

[49] R. K. Amiet, "Acoustic radiation from an airfoil in a turbulent stream," *Journal of Sound and Vibration*, vol. 41, no. 4, pp. 407–420, 1975.

[50] S. Moreau, M. Roger, and V. Jurdic, "Effect of angle of attack and airfoil shape on turbulence interaction noise," in *11th AIAA/CEAS Aeroacoustics Conference*, no. AIAA 2005-2973, (Monterey, California), MAy 23-25 2005.

[51] R. E. A. Arndt and R. T. Nagel, "Effect of leading edge serrations on noise radiation from a model rotor," in *5th Fluid and Plasma Dynamics Conference*, no. AIAA 72-655, (Boston, Massachusetts), June, 26-28 1972.

[52] P. T. Soderman, "Leading edge serrations which reduce the noise of low speed rotors," Technical note NASA TN D-7371, NASA, 1973.

[53] A. S. Hersh, P. T. Soderman, and R. E. Hayden, "Investigation of acoustic effects of leading edge serrations on airfoils," *Journal of Aircraft*, vol. 11, pp. 197–202, April 1974.

[54] S. Narayanan, P. Chaitanya, S. Haeri, P. Joseph, J. W. Kim, and C. Polacsek, "Airfoil noise reduction through leading edge serrations," *Physics of Fluids*, vol. 27, no. 2, p. 025109, 2015.

[55] P. Chaitanya, S. Narayanan, P. Joseph, and J. W. Kim, "Leading edge serration geometries for significantly enhanced leading edge noise reductions," in *22nd AIAA/CEAS Aeroacoustics Conference*, no. AIAA 2016-2736, (Lyon, France), 30 May - 01 June 2016.

[56] A. S. Lau, S. Haeri, and J. W. Kim, "The effect of wavy leading edges on aerofoil-gust interaction noise," *Journal of Sound and Vibration*, vol. 332, pp. 6234–6253, 2013.

[57] J. Turner, J. W. Kim, P. Chaitanya, and P. Joseph, "Towards understanding aerofoils with dual-frequency wavy leading edges interacting with vortical disturbances," in *22th AIAA/CEAS Aeroacoustics Conference*, no. 2016-2951, (Lyon, France), May, 30- June, 1 2016.

[58] B. Lyu and M. Azarpeyvand, "On the noise prediction for serrated leading edges," *Journal of Fluid Mechanics*, vol. 826, pp. 205–234, 2017.

[59] B. Lyu, M. Azarpeyvand, and S. Sinayoko, "Noise prediction for serrated leading edges," in *22th AIAA/CEAS Aeroacoustics Conference*, no. AIAA 2016-2740, (Lyon, France), May, 30- June, 1 2016.

[60] J. W. Kim, S. Haeri, and P. F. Joseph, "On the reduction of aerofoil-turbulence interaction noise associated with wavy leading edges.," *Journal of Fluid Mechanics*, no. 792, pp. 526–552, 2016.

[61] L. J. Ayton and J. W. Kim, "An analytic solution for the noise generated by gust-aerofoil interaction for plates with serrated leading edges," *Journal of Fluid Mechanics*, vol. 853, pp. 515–536, 2018.

[62] M. Wang and X. Liu, "Numerical investigation of aerodynamic and acoustic characteristics of bionic airfoils inspired by bird wing," *Proc IMechE, Part G: Journal of Aerospace Engineering*, 2018.

[63] R. Camussi, *Noise sources in turbulent shear flows: fundamentals and applications*, vol. 545. Springer Science & Business Media, 2013.

[64] M. Moreau, "Computational aeroacoustics." April 2006.

[65] T. F. Brooks, D. S. Pope, and M. A. Marcolini, "Airfoil self-noise and prediction," Reference Publication 1218, NASA, July 1989.

[66] P. T. Soderman and W. C. Horne, "Acoustic and aerodynamic study of a pusher-propeller aircraft model," 1990.

[67] M. Roger and S. Moreau, "Broadband self noise from loaded fan blades," *AIAA journal*, vol. 42, no. 3, pp. 536–544, 2004.

[68] R. Paterson and R. Amiet, "Acoustic radiation and surface pressure characteristics of an airfoil due to incident turbulence," in *3rd Aeroacoustics Conference*, p. 571, 1976.

[69] S. Moreau and M. Roger, "Competing broadband noise mechanisms in low speed axial fans," *AIAA journal*, vol. 45, pp. 49–57, January 2007.

[70] A. Pagano, M. Barbarino, D. Casalino, and L. Federico, "Tonal and broadband noise calculations for aeroacoustic optimization of a pusher propeller," *journal of aircraft*, vol. 47, pp. 835–848, May-June 2010.

[71] M. Landahl, "Unsteady transonic flow. international series of monographs in aeronautics and astronautics. division ii: Aerodynamics. vol. 2 pergamon press," 1961.

[72] I. S. Gradshteyn and I. M. Ryzhik, *Table of integrals, series, and products*. Academic press, 2014.

[73] M. Abramowitz and I. A. Stegun, *Handbook of mathematical functions with formulas, graphs and mathematical tables*. 1972.

[74] M. Roger and S. Moreau, "Extensions and limitations of analytical airfoil broadband noise models," *International Journal of Aeroacoustics*, vol. 9, no. 3, pp. 273–305, 2010.

[75] G. M. Corcos, "The structure of the turbulent pressure field in boundary-layer flows," *Journal of Fluid Mechanics*, vol. 18, pp. 353–378, March 1964.

[76] W. L. Keith, D. A. Hurdis, and B. M. Abraham, "A comparison of turbulent boundary layer wall pressure spectra," *Journal of Fluid Engineering*, vol. 114, pp. 338–347, September 1992.

[77] M. Bull and A. Thomas, "High frequency wall-pressure fluctuations in turbulent boundary layers," *The Physics of Fluids*, vol. 19, no. 4, pp. 597–599, 1976.

[78] G. F. Carey, J. E. Chlupsa, and H. H. Schloemer, "Acoustic turbulent water-flow tunnel," *The Journal of the Acoustical Society of America*, vol. 41, no. 2, pp. 373–379, 1967.

[79] T. M. Farabee, "An experimental investigation of wall pressure fluctuations beneath nonequilibrium turbulent flows," *The Journal of the Acoustical Society of America*, vol. 80, no. 4, pp. 1263–1263, 1986.

[80] G. Schewe, "On the structure and resolution of wall-pressure fluctuations associated with turbulent boundary-layer flow," *Journal of Fluid Mechanics*, vol. 134, pp. 311–328, 1983.

[81] H. Choi and P. Moin, "On the space-time characteristics of wall-pressure fluctuations," *Physics of Fluids A: Fluid Dynamics*, vol. 2, no. 8, pp. 1450–1460, 1990.

[82] W. W. Willmarth and C. E. Wooldridge, "Measurements of the fluctuating pressure at the wall beneath a thick turbulent boundary layer," *Journal of Fluid Mechanics*, vol. 14, no. 2, pp. 187–210, 1962.

[83] F. H. Clauser, "Turbulent boundary layer in adverse pressure gradients," *Journal of the Aeronautical Sciences*, vol. 21, pp. 91–108, February 1954.

[84] D. Coles, "The law of the wake in the turbulent boundary layer," vol. 1, no. 2, pp. 191–226, 1956.

[85] Y. Rozenberg, M. Roger, and S. Moreau, "Fan blade trailing edge noise prediction using rans simulations," in *Acoustics 08 Paris*, 2008.

[86] M. Barbarino and D. Casalino, "Hybrid analytical/numerical prediction of propeller broadband noise in the time domain," *International Journal of Aeroacoustics*, vol. 11, no. 2, pp. 157–176, 2012.

[87] S. Succi, R. Benzi, and F. Higuera, "The lattice boltzmann equation: a new tool for computatioanl fluid-dynamics," *Physica D*, vol. 47, pp. 219–230, 1991.

[88] H. Chen, S. Chen, and W. H. Matthaeus, "Recovery of navier-stokes eequations using a lattice-gas boltzmann method," *Physical Review*, vol. 45, pp. 5339–5342, April 1992.

[89] H. Chen, "Volumetric formulation of the lattice boltzmann method for fluid dynamics: basic concept," *Physical review E*, vol. 58, no. 3, p. 3955, 1998.

[90] S. Chen and G. D. Doolen, "Lattice boltzmann method for fluid flows," *Annuel review in fluid mechanics*, vol. 30, no. 1, pp. 329–364, 1998.

[91] Y.-H. Qian, S. Succi, and S. Orszag, "Recent advances in lattice boltzmann computing," in *Annual reviews of computational physics III*, pp. 195–242, World Scientific, 1995.

[92] D. P. Lockard, L.-S. Luo, and B. A. Singer, "Evaluation of the lattice-boltzmann equation solver powerflow for aerodynamic applications," Contractor Report 2000-210550, NASA, October 2000.

[93] E. Fares and S. Nöelting, "Unsteady flow simulation of a high-lift configuration using a lattice boltzmann approach," in *49th AIAA Aerospace Science Meeting including the New Horizons Forum and Aerospace Exposition*, no. AIAA 2011-869, (Orlando, Florida), January, 4-7 2011.

[94] D. Casalino, A. Hazir, and A. Mann, "Turbofan broadband noise prediction using the lattice boltzmann method," in *22nd AIAA/CEAS Aeroacoustics conference*, no. AIAA 2016-2945, (Lyon, France), May, 30 - June, 1 2016.

[95] D. Casalino, S. Nölting, E. Fares, T. V. de Ven, F. Perot, and G. Bres, "Towards numerical aircraft noise certification: Analysis of a full-scale landing gear in flyover configuration," in *18th AIAA/CEAS Aeroacoustics conference*, no. AIAA 2012-2235, (Colorado Springs, CO), June, 4-6 2012.

[96] M. R. Khorrami, E. Fares, and Da, "Towards full aircraft airframe noise prediction: detached eddy simulations," in *20th AIAA/CEAS aeroacoustics conference*, no. 2014-2481, (Atlanta, GA), June 16-20 2014.

[97] S. Nöelting and E. Fares, "The lattice-boltzmann method: an alternative to les for complex aerodynamic and aeroacoustic simulations in the aerospace industry," tech. rep., 2015.

[98] U. Frisch, B. Hasslacher, and Y. Pomeau, "Lattice-gas automata for the navier-stokes equation," *Physical review letters*, vol. 56, no. 14, pp. 1505–1508, 1986.

[99] D. Raabe, "Overview of the lattice boltzmann method for nano-and microscale fluid dynamics in materials science and engineering," *Modelling and Simulation in Materials Science and Engineering*, vol. 12, no. 6, p. R13, 2004.

[100] Exa Corporation, *PowerFLOW User's Guide*, 2016.

[101] P. L. Bhatnagar, E. P. Gross, and M. Krook, "A model for collision processes in gases. i. small amplitude processes in charged and neutral one-component systems," *Physical review*, vol. 94, pp. 511–525, May 1954.

[102] H. Chen, C. Teixeira, and K. Molvig, "Realization of fluid boundary conditions via discrete boltzmann dynamics," *International Journal of Modern Physics*, vol. 9, pp. 1281–1292, September 1998.

[103] D. A. Wolf-Gladrow, *Lattice-gas cellular automata and lattice Boltzmann models: an introduction*. Springer, 2004.

[104] V. Yakhot and S. A. Orszag, "Renormalization group analysis of turbulence. i. basic theory," *Journal of scientific computing*, vol. 1, no. 1, pp. 3–51, 1986.

[105] B. G. Marinus, V. Personnettaz, and V. Hoarau, "Steady flow around a serrated propeller for mini-remotely piloted aircraft," *International Review of Aerospace Engineering (I.RE.AS.E)*, vol. 8, pp. 131–140, August 2015.

[106] M. Terrance, "A-weighting: Is it the metric you think it is?," *Acoustics 2013*, pp. 1–4, 2013.

[107] I. B. Celik, U. Ghia, P. J. Roache, C. J. Freitas, H. Coleman, and P. E. Raad, "Procedure for estimation and reporting of uncertainty due to discretization in cfd applications," *Journal of Fluid Engineering*, vol. 130, pp. 1–4, July 2008.

[108] Exa Corporation, *PowerACOUSTICS User's Guide*, 2016.

[109] A. Halimi, B. G. Marinus, and S. Larbi, "Analytical prediction of broadband noise from mini-rpa propellers with serrated edges," *International Journal of Aeroacoustics*, vol. 18, no. 4-5, pp. 517–535, 2019.

[110] A. Halimi, B. G. Marinus, and S. Larbi, "Characterization of the broadband noise of mini-rpa propeller blades," in *23rd AIAA/CEAS Aeroacoustics Conference*, no. 2017-4053, (Denver (USA)), June, 5-9 2017.

[111] A. Halimi, B. Marinus, and S. Larbi, "Trailing edge noise of innovative mini-rpa propeller blades geometry," in *24th AIAA/CEAS Aeroacoustics Conference*, no. 2018-3451, (Atlanta, Georgia), June, 25-29 2018.

[112] R. Amiet, "Effect of the incident surface pressure field on noise due to turbulent flow past a trailing edge," *Journal of Sound Vibration*, vol. 57, p. 305, 1978.

[113] C. A. Leon, R. M. Martinez, D. Ragni, F. Avallone, and M. Snellen, "Boundary layer characterization and acoustic measurements of flow-aligned trailing edge serrations," *Experiments in Fluids*, vol. 57, no. 182, pp. 1–22, 2016.

[114] B. Marinus, A. Halimi, L. Constantin, and S. Cracana, "Effect of rotation on the 3d boundary layer around a propeller blade," in *23rd AIAA/CEAS Aeroacoustics Conference*, no. AIAA 2017-3866, (Denver (USA)), June, 5-9 2017.

[115] Y. Rozenberg, S. Moreau, M. Henner, and S. C. Morris, "Fan trailing edge noise prediction unsing rans simulations," in *16th AIAA/CEAS Aeroacoustics Conference*, no. AIAA 2010-3720, (Stockholm, Sweden), June 8-10 2010.

[116] C. Vaczy and D. McCormick, "A study of the leading edge vortex and tip vortex on prop fan blade," *Journal of Turbomachinery*, vol. 109, no. 3, pp. 325–331, 1987.

[117] F. Avallone, W. Van der Velden, D. Ragni, and D. Casalino, "Noise reduction mechanisms of sawtooth and combed-sawtooth trailing-edge serrations," *Journal of Fluid Mechanics*, vol. 848, pp. 560–591, 2018.

[118] F. Avallone, S. Pröbsting, and D. Ragni, "Three-dimensional flow field over a trailing-edge serration and implications on broadband noise," *Physics of Fluids*, vol. 28, no. 11, p. 117101, 2016.

[119] X. Liu, H. Kamliya Jawahar, M. Azarpeyvand, and R. Theunissen, "Wake development of airfoils with serrated trailing edges," in *22nd AIAA/CEAS Aeroacoustics Conference*, p. 2817, 2016.

[120] A. Halimi, B. G. Marinus, and S. Larbi, "Analytical investigation of turbulence interaction noise of mini-rpa serrated blades," in *25th AIAA/CEAS Aeroacoustics Conference*, p. 2524, 2019.

[121] S. Narayanan, P. Joseph, S. Haeri, J. Kim, P. Chaitanya, and C. Po, "Noise reduction studies from the leading edge of serrated flat plates," in *20th AIAA/CEAS Aeroacoustics Conference*, no. AIAA 2014-2320, (Atlanta, GA), June, 16-20 2014.

[122] T. P. Chong, T. Biedermann, O. Koster, and S. M. Hasheminejad, "On the effect of leading edge serrations on aerofoil noise production," in *24th AIAA/CEAS Aeroacoustics Conference*, no. 2018-3289, (Atlanta, Georgia), June, 25-29 2018.

[123] S. Moreau, J. Foss, and S. Morris, "A numerical and experimental test-bed for low speed fans," *Proc IMechE, Part A: Journal of Power and Energy*, vol. 230, no. 5, pp. 456–466, 2019.

[124] E. Schulein, H. Rosermann, and S. Schaber, "Transition detection and skin friction measurements on rotating propeller blades," in *28th Aerodynamic measurement technology, ground testing and flight testing conference*, no. 2012-3202, (New orleans, Louisiana), June, 25-28 2012.